2021

Linear and Nonlinear Optical Effects in High Carrier Concentration Oxides and Nitrides at Epsilon-Near-Zero

Ray Secondo
Virginia Commonwealth University

Linear and Nonlinear Optical Effects in High Carrier Concentration Oxides and Nitrides at Epsilon-Near-Zero

A Dissertation submitted in partial fulfillment of the requirements for the degree of Doctor of Philosophy at Virginia Commonwealth University

By

Ray Secondo

Trine University, B.S. 2016

Virginia Commonwealth University, 2016-2021

Director: Nathaniel Kinsey, Associate Professor, Electrical and Computer Engineering

Richmond, Virginia

September 2021

I’d like to thank my family, friends, mentors and cohorts. Individually, my parents for their support and guidance. Dr. Sis for guidance through the doctoral process. Alicia for support and love through this time. Kyle for his nonsense and endless optimism. TJ Squad for a constant stream of bad movies and good jokes. Dr. Kinsey for his support and positive influence. Dhruv for his willingness to discuss everything work related. Adam for his long hours running experiments. The rest of the team for their input and positivity.

ACKNOWLEDGMENTS

Air Force Office of Scientific Research (FA9550-1-18-0151); Defense Advanced Research Projects Agency (HR00111820063).

Virginia Microelectronics Consortium

TABLE OF CONTENTS

TABLE OF FIGURES

TABLE OF VARIABLES AND CONSTANTS

Variable	Variable Name
n	Refractive Index
n_2	Nonlinear Refractive Index
I	Intensity
x	Electron Displacement
γ	Lorentz Oscillator Damping
Γ	Electron Scattering Rate
ω	Frequency
ω_0	Electron Resonant Frequency
E	Electric Field
D	Electric Displacement Field
P	Polarization
N	Carrier Concentration
ε_r	Relative Permittivity
$\chi^{(n)}$	nth order Susceptibility
m^*	Effective Mass
a_e	Electron Acceleration
F	Force
k	Crystal Momentum/ Crystal Vector
t	Time
v	Electron Velocity
ρ	Electron Momentum
E_g	Band Gap
E	Energy
v_ϕ	phase velocity
v_g	group velocity
f	Fermi-Dirac Distribution
ρ	Density of States
μ	Chemical Potential
μ_e	Electron Mobility
A	Absorptivity
τ	Electron Relaxation Rate
d	Film Thickness
R	Reflection
T	Transmission
T_e	Electron Temperature

U	Energy Density	Ψ	Ellipsometric Amplitude
λ	Wavelength	Δ	Ellipsometric Phase
ϕ	Phase	$\tilde{r}_{s,p}$	Complex Reflection Coefficients of r, p Polarizations
α	Absorption Coefficient		

Constant	Constant Value	Constant
q	$1.6 \times 10^{-19}\ J$ $1\ eV$	Charge of an Electron
m_0	$9.1 \times 10^{-31} kg$	Mass of an Electron
ε_0	$8.85 \times 10^{-12}\ F/m$	Permittivity of Free Space
c	$3 \times 10^{8}\ m/s$	Speed of Light
$\hbar$	$1.05 \times 10^{-34}\ J$ $6.58 \times 10^{-16}\ eV$	Planks Constant
k_B	$1.38 \times 10^{-23}\ J \cdot K^{-1}$	Boltzmann Constant

ABSTRACT

The study of optics is entirely a study of how light and materials interact. On the nano-scale, quantum optics allows for the study of a few photons and small materials. As the number of photons increases, the standard operating regime of “linear” optics applies to describe the interaction of light waves and materials. This range describes much of photonics knowledge such as metals and dielectrics, lenses, waveguides, and other light-matter interactions. As the number of photons increases to high fluences, a range of “nonlinear” optics is achieved. Here, the material polarization induced is no longer linearly related to the driving field as higher order effects come into play. Nonlinear optics has been an important method for achieving ultrafast light manipulation, while linear optics has been critical for general control.

In all realms of optics, the quest for new physics and improved efficiency of effects have required materials research that guides a loop of improvement. CMOS compatible optics for on-chip light control has been a driving force pushing the discovery of materials that can replace noble metals. This has led to the optimization of semi-metals, such as titanium nitride, and transparent conducting oxides such as indium tin oxide and aluminum-doped zinc oxide. In a similar vein, gallium nitride has been a recent avenue of research to enable high power devices where silicon-based devices begin to break down. While these materials began for other reasons, they have also influenced other research avenues such as nonlinear optics.

In particular, these materials have gained interest in nonlinear optics due to their ability to exhibit epsilon-near-zero (condition when $-1 < Re\{\varepsilon\} < 1$) and near-zero-index (condition when $-1 < Re\{n\} < 1$) optical parameters. Due to inherent advantages such as slow light, improved

confinement, and ideal relaxation times, the nonlinear response of these materials, such as the intensity-dependent-refractive-index, are ultra-large ($\Delta n \approx n_0$) yet remain ultra-fast (100s of fs rise and fall). This experimental discovery of epsilon-near-zero enhancement has thus opened new avenues in nonlinear optics research in recent years, and while experiments have continued to progress a theoretical understanding of the processes and origins of nonlinear optical enhancement at epsilon-near-zero has lagged.

To fill this gap, the work herein focuses on uncovering the mechanisms that drive the nonlinear interactions of Drude-based epsilon-near-zero materials. This framework utilizes knowledge of a given material's electronic band structure in energy-momentum space to understand the kinetic motion of free electrons under intense optical irradiation, realizing a fully feed-predictive simulator without fitting parameters. From this, two types of nonlinearities are elucidated, intra- and inter-band, whose overall effect on the optical properties are rooted in the non-parabolic dispersion of energy bands. Intraband nonlinearities are shown to originate from an increase in the overall effective mass of the electron sea while interband nonlinearities were shown to be dominated by generation of excess free electrons. Moreover, these effects are shown to induce opposing changes on the optical permittivity leading to distinctively different outcomes that can be used individually or together to sculpt the material's optical properties in time and space.

Paired with in-house growth, experimental data collected from literature, collaborators, and in-house experiments have been used to rigorously validate the theory across different materials, growth processes, and experimental conditions. Experimental methods of beam deflection and reflection-transmission modulation were used to study Al:ZnO and Ga:ZnO. Results include the first studies of Ga:ZnO as a nonlinear material in the near-infrared as well as some of the first

works utilizing beam deflection as a characterization method. Both intraband and interband nonlinearities are interrogated through these methods with the first known multi-pump (combined inter- and intraband nonlinearities) beam deflection studies in epsilon-near-zero materials.

Building from these demonstrations, the theoretical framework is used to guide exploration into the roles of optical loss, plasma frequency, and thickness of epsilon-near-zero materials with the intent to improve the efficiency of the nonlinearity for future applications. Moreover, the theoretical framework enables the exploration of new materials yet to be experimentally studied. Figures of merit were developed to enable quick intuition into the relative efficiency of either nonlinearity for new materials. This enables us to predict materials, such as highly doped gallium nitride which are likely to perform as well as, if not better than the current materials used.

Through this holistic study, improved prediction power is available for finding the ideal nonlinear films, and effects can be explored to optimize them. Full modeling of the nonlinear responses of materials allows for further advancement, not only from thin films as studied here, but in fabricated structures where field confinement and enhancement can be designed around to induce even more efficient nonlinear responses.

1. BACKGROUND: OPTICAL PROPERTIES OF OXIDES AND NITRIDES

Often, advancements in optics come from a combination of new physics and new materials. A recent example of this advancement is ultrafast, large nonlinear effects in epsilon-near-zero (ENZ) [1–6] materials. Nonlinear effects occur at high electric fields, causing materials to behave differently than the low field material [7]. For example, the intensity-dependent refractive index (IDRI) is an effect where the refractive index changes proportionally to the incident optical intensity ($n = n_0 + n_2 I$). ENZ materials are not brand new; instead, they have been developed for many explorations such as transparent conductors like indium doped tin oxide (ITO) [8–14], aluminum or gallium doped zinc oxide (AZO or GZO) [15–19], and cadmium oxide (CdO) [8,20–23], transparent conducting oxides (TCOs). Exploration into exploiting the effective Kerr index ($n_2 \propto 1/n$) with a near-zero-index (NZI) material lead to revelations into near unity refractive index modulation and opening new avenues in all-optical switching and frequency conversion [24,25].

To understand the mechanisms driving these nonlinear processes, a review of modeling the linear and nonlinear optical properties of materials is provided in Chapter 1. This lays the foundation of the mathematical descriptions and physics used to describe the ENZ materials and nonlinear interactions that have attracted significant interest in recent years, including our new efforts discussed in Chapters 2-6.

1.1. Electronic Band Structures

Fundamentally the linear and nonlinear optical properties of materials are dictated by the way electrons interact with an incoming electromagnetic light wave. When inside a material, this also includes the local forces and interactions on electrons due to the nuclei, other nearby electrons, material bonds, material structure, etc. Collectively these effects modify the electron's dispersion relation, which relates its energy and momentum. In vacuum, an electron has a parabolic dispersion relation, $E = \frac{\hbar^2}{2m_0}k^2$, where m_o is the mass of an electron. However, inside a material, the local forces perturb this relationship which is described through the introduction of the 'effective mass' term m^* (see a more in depth discussion of effective mass in Section 1.2):

$$E = \frac{\hbar^2}{2m_0 m^*}k^2. \qquad 12$$

As a result, the relation illustrates a set of energies, or a band of energies, that an electron can take as a function of its momentum within the crystal structure. As the electron moves further from the Γ point of a crystal structure (the zero momentum point), the atomic cell pushes and pulls the electron, requiring additional energy to gain the momentum required to traverse toward symmetry points. A similar statement can be written for electrons that reside in different bonds within the material (e.g. p bonding, s anti-bonding, etc.) each with their own unique energy and momentum. The combination of these various energy bands, each describing the dispersion of an individual bonding state, forms the band structure of a material (see Figure 1a). A key consequence of this interaction is the formation of a set of energies where no electron states exist in the band structure, a region called the bandgap. The band structure and its inherent features, is extremely useful for understanding electrical, optical, and thermal effects that occur within crystalline materials.

The states of the band structure that are occupied with electrons is quantified by the Fermi Energy or chemical potential, defined as the energy where there is a 50% probability of finding an occupied state at room temperature. For this work, discussion focused on electrons that near the Γ point of the material. In this region a conduction band and valence band are defined for free and bound electrons respectively. For films that are intrinsic (i.e. containing only the primary atoms, Si, Ga-As, etc.) the Fermi level exists within the bandgap of the valence and conduction bands. However, this can be modified through a process called doping where intentional atomic defects are introduced into the material to either donate an extra electron, n-type, or remove an electron, p-type, when they replace the host material atom (e.g. B or P in Si). At high doping levels, such as those for the ENZ materials considered here, the Fermi level can be degenerate, residing as much as 1 eV into the conduction band. As a result, the material is doped sufficiently to provide ensure many states within the conduction band are occupied, therefore providing a large density of free electrons and an electrically conductive nature to the material. Here, the reference energy is given as the conduction band minimum (CBM) rather than the valence band maximum (VBM) where the bandgap, E_g, would be added.

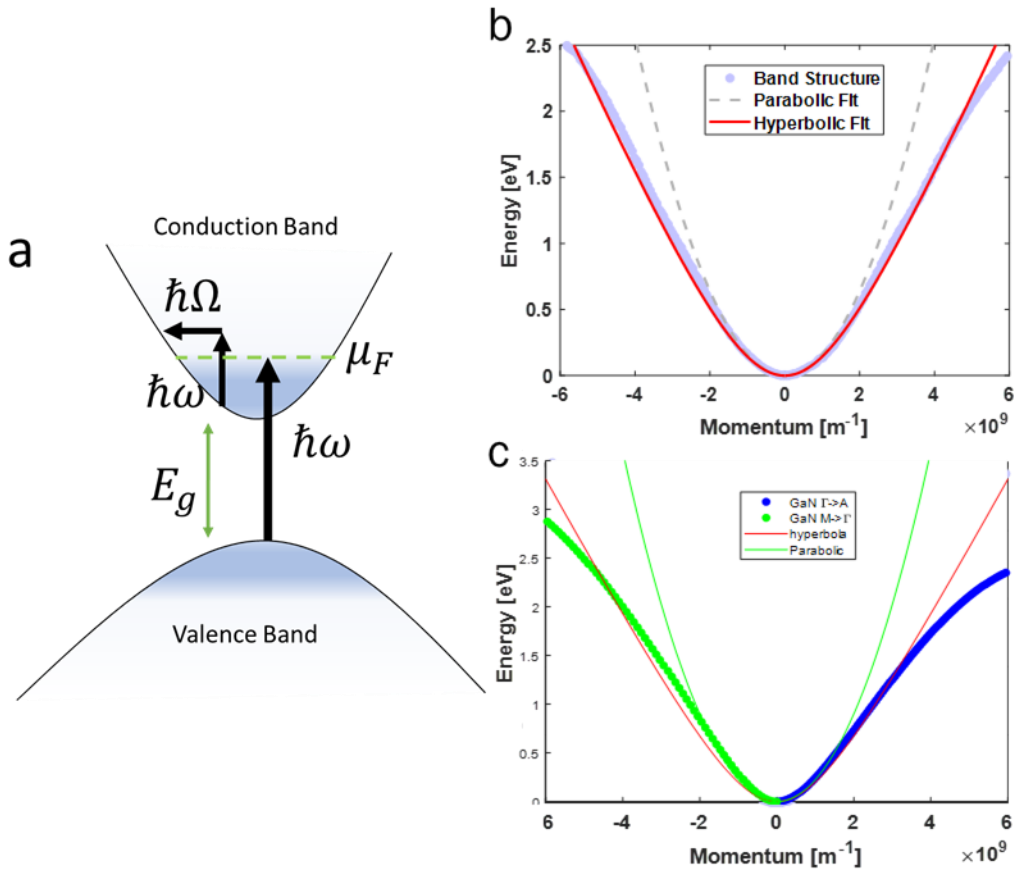

Figure 1: a) Generic direct band gap band structure showing a direct transition ($\hbar\omega = E_g + \mu_F$) between valence band the conduction band and an intraband transition from the conduction band to an elevated conduction band energy. b) Conduction band near the Γ point for doped zinc oxides compared between literature [30] (lilac dots), parabolic fit (grey dashed line), and a hyperbolic fit (red line) showing a good overlap of the hyperbolic fit and a poor fit for parabolic away from the CBM. c) Conduction band near the Γ point for doped gallium nitride compared between density-functional-theory calculated in-house (green and blue dots), parabolic fit (green line)) and a hyperbolic fit (red line) showing a reasonable overlap of the hyperbolic fit in positive k, and a poor fit for parabolic away from the CBM.

In real materials, the conduction band is not a perfect parabola beyond a certain range of energy, as seen in Figure 1, although the parabolic approximation is an accurate approximation near the CBM. In highly doped semiconductors such as ITO and aluminum/gallium doped zinc oxide (AZO, GZO), and doped gallium nitride (GaN) the Fermi level can be >1eV into the conduction band, far

from the range where the parabolic approximation is valid [20,31,32]. We have amended this distinction through various methods described later in Section 2.

1.2. Effective Mass

As discussed in Section 1.1, the forces of the material lattice lead to an electron which appears to have a different mass m^*m_0, quantified by the effective mass, m^*. From a Newtonian derivation, the effective mass is a result of the acceleration of the electrons:

$$F = ma_e = F_{ext} + F_{latt} = m^*m_0a_e \tag{13}$$

From this definition, the acceleration of the electron in a material can be lower or higher than the acceleration which would be found for an electron in a vacuum from the external force. A full derivation given in [33] is summarized here, finding that:

$$\hbar\frac{dk}{dt} = F_{ext} \tag{14}$$

where k is the crystal momentum. The work done on an electron by this force is calculated:

$$\delta E = F_{ext}v\delta t \tag{15}$$

and from this, we find the rate of acceleration as:

$$\frac{dv}{dt} = \frac{1}{\hbar}\frac{d^2E}{dkdt} = \frac{1}{\hbar}\frac{d^2E}{dk^2}\frac{dk}{dt} \tag{16}$$

and thus, we find the effective mass:

$$\frac{\hbar^2}{\left(\frac{d^2E}{dk^2}\right)}\frac{dv}{dt} = m^*m_0\frac{dv}{dt} = F \tag{17}$$

$$m^*m_0 = \hbar^2\left(\frac{d^2E}{dk^2}\right)^{-1}. \tag{18}$$

This definition of effective mass will be referred to in this work as the "band curvature effective mass".

The second definition of effective mass, [16,31] referred to here as the "transport effective mass" can be derived if the focus is on momentum, rather than acceleration. Here, the beginning equation is $\rho = mv$ rather than $F = ma$. Considering the relationship between momentum and crystal vector, $\rho = \hbar k$, we find:

$$m^* m_0 = \frac{\rho}{v} = \frac{\hbar k}{v}. \tag{19}$$

Using the findings of velocity from above, this definition finds:

$$m^* m_0 = \hbar^2 k \left(\frac{dE}{dk}\right)^{-1}. \tag{20}$$

These two definitions will be revisited in Section 3 for how they compare for our model derivation.

1.3. Optical Absorption in Intrinsically Doped Materials

With an understanding of the electronic band structure of a material, we can use this description to quantify the absorption of light by a material. Linear optical absorption can generally occur due to two processes, interband and intraband, shown in Figure 1a. For interband absorption, electrons are promoted from the valence band to the conduction band through the absorption of the photon. Near the band edge, the absorption coefficient in direct gap semiconductors, where the maximum/minimum of the valence/conduction bands are located at the same momentum such as indium oxide and zinc oxide, can be calculated as $\alpha = B\frac{\left(E-E_g\right)^2}{E}$ where B is a constant used to match measurements and is related to the strength of the dipole matrix element

that describes wavefunction overlap of the initial and final states [11,107]. Thus, strong absorption is expected for photon energies above the bandgap. However, if a material is degenerately doped to where the Fermi level lies above the CBM, Pauli blocking shifts this absorption edge to higher energies such that $E_g \approx E_{g,o} + E_F$.

Intraband absorption describes the transition of a below-Fermi level electron to above the Fermi level in the same conduction band. This transition has a lower energy than interband absorptions and contributes to free-carrier absorption in conductive samples. Since this transition is not purely vertical (i.e. only requiring energy), momentum must also be provided. This occurs through the simultaneous absorption of a photon and a scattering, which provides momentum, enabling the diagonal transition. The scattering event can occur due to processes such as impurity or phonon scattering. Due to this interaction, the absorptivity of our film is dependent on the number of free carriers and the scattering rate of the electrons. Experimental measurements of absorption as a function of frequency shows a proportionality, $\alpha_{fc} \propto \omega^{-\beta}$, where β is in the range from 2 to 3.

1.4. Nonlinear Lorentz Oscillator Model and Nonlinear Polarization

Form a microscopic perspective, electronic band structures and absorption events dictate how electrons are modified by optical energy. However, it is in many cases necessary to deal with bulk materials that have many electrons, occupied states, etc. In this case, utilizing the microscopic picture can be cumbersome, and another approach is desired. When the material is sufficiently large to invoke a bulk approximation, the interaction of bound electrons residing within the

valence and light can be described with a classical mass-spring model called the Lorentz Model [28]:

$$\ddot{x} + \gamma\dot{x} + \omega_0^2 x = -\frac{q}{m_0} E_x(t). \quad (1)$$

where x is the electron displacement, ω_0 is the resonant frequency of the system, γ is the electron damping rate, q is the electron charge, m_0 is the electron mass, and $E_x(t)$ is the electric field in the direction of displacement. Here, the resonant frequency models the transition of an electron between two states, such as through interband absorption. Taking the electric field as a single frequency sinusoid, the solution is found as:

$$x = \frac{q}{m_0} \frac{1}{\omega_0^2 - \omega^2 - i\gamma\omega} E_x(t). \quad (2)$$

This displacement can be linked to the polarization of the atom, measuring the amount an electron is displaced from its atom by the electric field, through the relation $P_x = Nqx$ where N is the number of bound electrons. In turn, this leads to a displacement field of:

$$D = \varepsilon_0 E + P = \varepsilon_0 E + \frac{Nq^2}{m_0} \frac{1}{\omega_0^2 - \omega^2 + i\gamma\omega} E \quad (3)$$

$$D = E\varepsilon_0 \left(1 + \frac{Nq^2}{\varepsilon_0 m_0} \frac{1}{\omega_0^2 - \omega^2 - i\gamma\omega}\right). \quad (4)$$

The permittivity and susceptibility, defined as $\frac{D}{E\varepsilon_0} = \varepsilon_r = 1 + \chi E$, can then be utilized as simple expressions for the overall interaction of light with a material that has an absorption resonance at some frequency ω_0. If a material has multiple resonant frequencies, ω_{0j}, the contribution from each can simply be summed taking into account various oscillator strengths f_j dictated by each absorption process, leading to a total Lorentz permittivity of:

$$\varepsilon_r = 1 + \frac{Nq^2}{\varepsilon_0 m_0} \sum_j \frac{f_j}{\omega_{0j}^2 - \omega^2 - i\gamma\omega}. \quad 5$$

Away from absorption the permittivity is generally non-dispersive and can be lumped as the sum of all oscillators of higher frequencies into a term ε_∞ which denotes the background permittivity. This same model can be extended to describe nonlinear optical phenomena as well by relaxing the restriction of Equation 1 that the model must be linearly dependent upon the applied field. If we allow higher order terms, we can introduce nonlinear displacement and susceptibility terms which all contribute to the total polarization experienced by the material [7],

$$P = \varepsilon_0(\chi^{(1)}E + \chi^{(2)}E^2 + \chi^{(3)}E^3 + \cdots) \quad 6$$

where superscript (n) denotes the order of susceptibility, where $\chi^{(1)}$ represents the linear susceptibility. The strength of the nonlinear susceptibilities is generally many orders of magnitude smaller than $\chi^{(1)}$ ($\chi^{(2)} \sim 10^{-12}\frac{m}{V}$; $\chi^{(3)} \sim 10^{-24} m^2/V^2$) [27], requiring extremely large fields to access any polarization beyond the linear case. The relation therefore states that under small driving fields, the polarization can be approximation as linearly dependent upon the electric field (as was done above for the Lorentz permittivity). However, under strong electric fields, typically on the order of the interatomic electric field, the polarization becomes nonlinear and its relation must therefore be modified to account for these higher-order deviations. Although weak, nonlinear optical effects can give rise to useful effects such as harmonic generation and two beam coupling. An important distinction should be made that $\chi^{(2)}$, while larger than $\chi^{(3)}$, only exists in non-centrosymmetric materials, leading to a strong emphasis on $\chi^{(3)}$ as a more general nonlinear process.

In the following research, the focus is on a $\chi^{(3)}$ effect which modifies the magnitude of the refractive index, called the intensity-dependent refractive index (IDRI). For bound electronic polarization nonlinearities, the material polarization follows both the electric field and the cube of the electric field, which becomes dominant at high fields. We can quantify the resulting effect on the refractive index of the material by relating the effect on the permittivity and the index of the material:

$$n^2 = (n_0 + n_2 I)^2 = 1 + \chi^{(1)} + \chi^{(3)}|E|^2 \quad 7$$

where $n = \sqrt{\varepsilon_r}$. Simplifying, we can define an IDRI coefficient:

$$n_0^2 + 2n_2 I + n_2^2 I^2 \approx n_0^2 + 2n_2 I = \left(1 + \chi^{(1)}\right) + \chi^{(3)}|E|^2 \quad 8$$

$$n_2 = \frac{3\chi^{(3)}}{4\varepsilon_0 n_0 c}. \quad 9$$

While the origins of the nonlinear process in ENZ materials is not due to nonlinear polarization, as described above, the result is also a modification to the refractive index. As a result, the same theoretical framework can be used to quantify the effects, which is useful for comparing to other materials in literature, so long as one understands that the origin of the nonlinearity is not solely nonlinear polarization. To indicate this when discussing or comparing $\chi^{(3)}$ or n_2, we utilize the term 'effective', denoted $\chi^{(3)}_{eff}$ or $n_{2,eff}$.

In the case of a lossy film, altering the index through a $\chi^{(3)}$ process also induces a change in loss. This effect is mandated through Kramer's Kronig [7] where a change in index causes a change in loss, and vice versa. The change in loss due to a $\chi^{(3)}$ change in index is often termed as α_2, as a parallel to n_2, giving the equation $\alpha = \alpha_0 + \alpha_2 I$. The nonlinear absorption term, α_2, can be either positive or negative. In the case where $\alpha_2 > 0$ (absorption is increased), this term typically

describes multi-photon absorption processes such as two-photon absorption where $\hbar\omega_3 = \hbar\omega_1 + \hbar\omega_2$. The rate of this two-photon interaction is proportional to intensity as sufficient photons are required to combine probabilistically. When $\alpha_2 < 0$ (absorption is decreased), this term describes saturable absorption processes such as state-filling in finite density of state systems, bandgap shifts, etc. This term is again proportional to intensity as it requires a large number of absorption processes to occur that subsequently affects the ability of additional photons to be absorbed. When small numbers of photons are absorbed, the change in the absorption is minimal. However, if a large number, comparable to the number of available states, are absorbed the loss within the material can be greatly modified.

1.5. Drude Model

While the Lorentz oscillator is used for bound electron's contribution to the polarization and permittivity, free electrons contribute to permittivity producing a metallic nature. This Drude oscillator term can be derived from the same spring model, Equation 1, without the restoring force (resonant frequency) resulting in a similar result of:

$$\ddot{x} + i\Gamma\dot{x} = \frac{q}{m}E_x(t) \tag{10}$$

$$\varepsilon_r = \varepsilon_\infty - \frac{\omega_p^2}{\omega^2 + i\Gamma\omega}, \omega_p^2 = \frac{Nq^2}{\varepsilon_0 m^* m_0} \tag{11}$$

where N is the free carrier concentration, and ω_p is the "unscreened" plasma frequency, Γ is the characteristic loss, and m^* is the effective mass; the permittivity would be zero if the background permittivity was unity, representing vacuum or free space.

1.6. Introduction to ENZ

ENZ materials are a set of materials with a permittivity that approaches zero, achieved in bulk materials through either an absorption resonance or the presence of free carriers, see Figure 2. This has an important distinction from NZI materials where the refractive index ($n = \sqrt{\varepsilon}$) approaches zero. This distinction can be made when the loss is high enough where the refractive index does not dip below unity, which leads to different enhancement interactions.

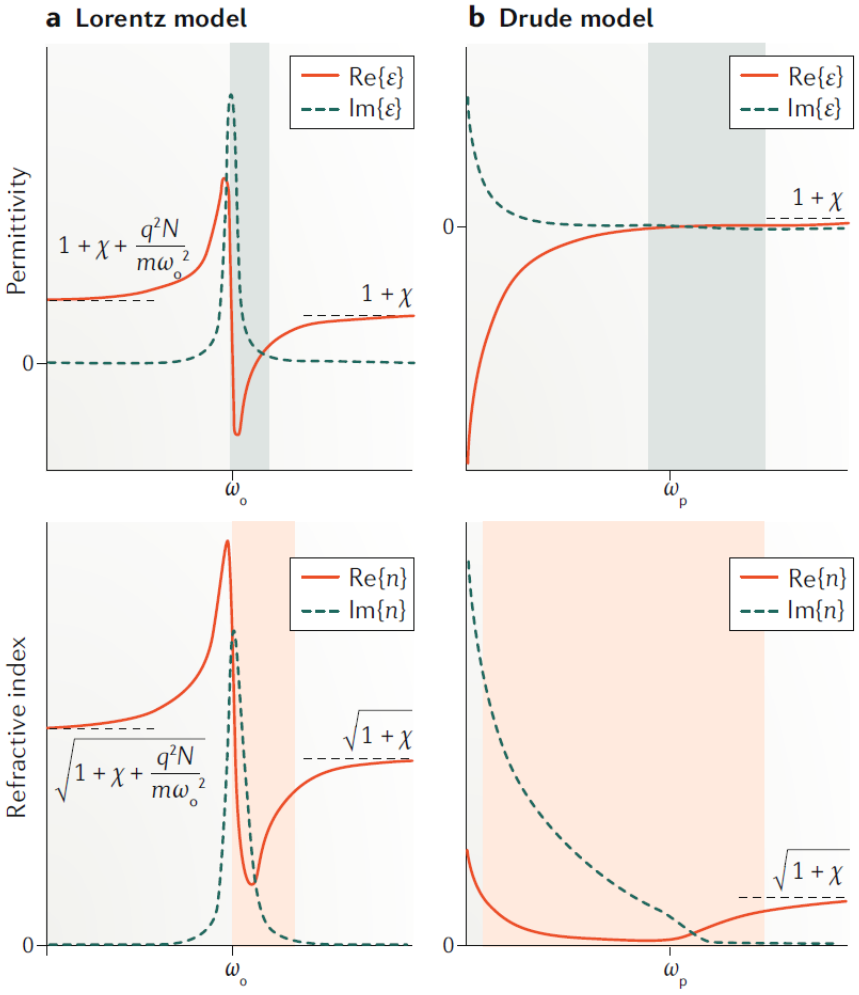

Figure 2: A near zero permittivity can be achieved through multiple means, such as a) a strong Lorentz oscillator and b) a Drude dispersion. This effect is shown in both permittivity (top) and refractive index (bottom) for both cases. Figure adapted from [5] under Creative Commons license.

When a film exhibits NZI properties, a handful of distinct effects are observed which enhance light matter interaction [2,3,34]. First, the phase velocity, v_ϕ, in NZI tends toward infinity while the group velocity,v_g, tends toward zero in an effect called "slow light" [35,36]:

$$v_\phi = \frac{c}{n} \tag{21}$$

$$\mathrm{v_g} = \frac{c\sqrt{\varepsilon(\omega)}}{\varepsilon(\omega) + \frac{\omega}{2}\frac{\partial\varepsilon(\omega)}{\partial\omega}}. \tag{22}$$

The phase velocity describes how the phase of light propagates through a material and is related to the effective wavelength of light in a material, $\lambda_{eff} = \lambda/n$. For an NZI film with a phase velocity near infinity, this results in a long effective wavelength or "DC light". In practice, this aids nonlinear interaction of frequency mixing as the strength of these effects is related to the phase overlap between beams that is designedly high due to this enhanced effective wavelength.

The group velocity describes the propagation of the photon in time. A low group velocity elongates the propagation of a photon through a material and compresses optical pulses in time. Slow light works to enhance light-matter interaction by allowing for extended interaction time that leads to more absorption and electric field interactions [37,38].

Another effect that enhances interactions is the D-field continuity:

$$\varepsilon_1 E_{\perp 1} = \varepsilon_2 E_{\perp 2}. \tag{23}$$

When the permittivity (and index) of the second material approaches zero, this leads to an exceedingly high electric field within the material. This high electric field enhances all types of optical interactions by increasing the electric field. While NZI materials exhibit all three enhancement mechanisms, ENZ materials only exhibit the final interaction which leads to a

reduction in the potential enhancement of light-matter interactions. One such film studied in our work is titanium nitride. While TiN is a fantastic material for its semi-metal tunability and large damage thresholds [39], preliminary studies from other groups show that the linear loss is too high for NZI effects, which limit its enhancement of light-matter-interaction [40].

2. ELLIPSOMETRY ON LOSSY THIN FILMS

While the majority of this work will be focused on the nonlinear properties of films, it is critical to understand the linear properties of the films under study. Ellipsometry is a prominent tool in linear characterization of materials; however, thin films with significant loss can lead to error in characterization if additional steps are not taken. Proper rigorous characterization of the linear material is important to minimize error in the understanding of nonlinear measurements.

To illustrate the importance careful extraction of linear optical properties, efforts to characterize high quality TiN thin films are discussed. Our team's TiN studies have produced the lowest loss of atomic layer deposition (ALD) films available for TiN. To verify the film quality, accurate characterization is important. Multiple techniques for measurement were utilized, including spectroscopic ellipsometry with reflection (SE+R), see Section 2 [41].

2.1. Ellipsometric Methods of Film Characterization

Plasmonics [42,43] is a wide-reaching field that has a variety of applications including near-field imaging [44,45], biological sensing [46], magnetic memory [47], data transfer [48–50], particle trapping [51], energy harvesting [52], metasurfaces [53–55] and more [56]. Traditional plasmonics often relies on noble metals for their low loss and large negative permittivity. These factors are necessary for enabling long propagation lengths and strongly confined modes. Yet, noble metals are limited by aspects such as a low melting temperature and difficulties in forming sub-nanometer smooth films that can be important in light confinement and high-power optics research.

These limitations of traditional plasmonic materials have spurred research into alternative plasmonic materials with optical properties that are similar to noble metals like silver and gold [57]. Titanium nitride (TiN) is one of the more promising alternatives due to its robustness [58], gold-like properties, and CMOS-compatibility [9,59–62]. Additionally, it is tunable with plasma frequency variations from less than 450 nm to over 600 nm with widely varying loss [10,63–66]. However, the material properties of such alternative plasmonic materials can vary widely based on the growth methods and the conditions employed. To understand the origins of such large variation and reliably tune the growth conditions to achieve the desired material characteristics, consistent and accurate measurement of optical properties is needed.

Many techniques exist to measure the optical properties of thin films, including spectroscopic ellipsometry (SE) and reflection-transmission (RT). Both measurements utilize known material properties and physically-based calculations to find unknown material properties from measured values. SE is a widely used method [67–70] due to its relative ease and self-referenced nature. It is often used for non-absorbing and semi-absorbing thin films that are easily determined from layers of unknown thickness. Absorbing films, such as metals, present a special difficulty to the measurement of either RT or SE.

In this section, I will show examples of characterizing titanium nitride ultrathin films using SE with and without supplemental transmission intensity (T) data. Without T data, the resulting permittivity, which provides a good match to the SE data through modeling, shows a significant variance, of up to 3× for a single film, characterized by the figure of merit (ε’/ε”). Combining SE and T data reduces the model ambiguity allowing the optical constants, film thickness, and growth rate of films to all be determined. Through a case study of three TiN films on sapphire

substrates using plasma-enhanced atomic layer deposition, we show that the addition of T is an important step in the characterization of such materials. This section is directly from Secondo et al. [41].

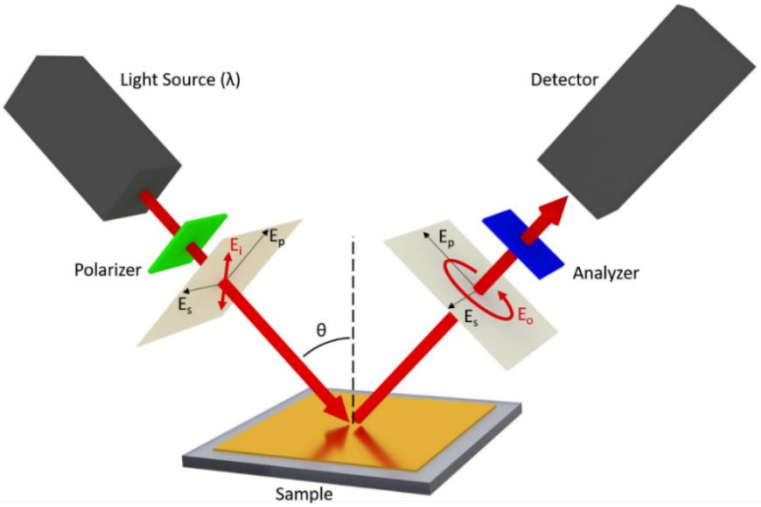

Figure 3 Schematic of spectroscopic ellipsometry. Here, a light source with wavelength λ is configured to produce an arbitrary polarization state (Ei) by a variable polarizer. The incident beam is then used to interrogate the sample at an angle θ. The polarization state of the reflected beam (Eo) is altered by the interaction with the sample. After passing through an analyzer, which allows the polarization state of the reflected beam to be measured at two perpendicular states, the complex s and p reflection coefficients of the sample can be determined.

Spectroscopic Ellipsometry is a powerful method for finding the refractive index and thickness of thin films. Spectroscopic Ellipsometry measures the reflected change of polarized light at oblique angles to characterize the material properties. Bulk materials can be characterized by the complex reflection coefficients for *s* and *p* polarized light, see Figure 3 [71]. For thin films, reflections from the second surface interfere with the top-reflections to produce interference patterns in the measured SE spectra that can be used to calculate both film thickness and refractive index. SE data is characterized using two values, Ψ and Δ, which are calculated using the formula:

$$\frac{\tilde{r}_p}{\tilde{r}_s} = \tan\Psi\, e^{i\Delta} \qquad 24$$

where $\tilde{r}_p$ and $\tilde{r}_s$ are the complex reflection coefficient for *p* and *s* polarized light, respectively. The data represented by Ψ and Δ do not directly translate to the thin-film thickness and refractive index; rather, the data must be matched to a model-calculation based on best-fit sample properties. To reduce unknown parameters that describe material optical constants, a variety of dispersion equations are often implemented such as Cauchy, Sellmeier, general oscillators (e.g. Drude, Lorentz), and B-Spline [72].

As plasmonic materials are inherently lossy, general oscillator and B-Spline dispersion are used in this work. B-Spline dispersion equations provide an efficient and easy way to extract optical parameters, but some limitations exist such as an inability to extract physical meaning from the results [73]. General oscillators are a broad category of dispersion equations that use physically-derived functions, such as Drude, Lorentz, Tauc-Lorentz, and others, to model the permittivity [72] (see Methods). As an example of parameter extraction, the Drude equation has the unscreened plasma frequency ω_p that can be calculated as $\omega_p = \sqrt{\frac{Nq^2}{\varepsilon_0 m^*}} = \sqrt{\frac{1}{\rho_0 \varepsilon_0 \tau}}$, and from these, possible extracted values include the free electron density *N*, effective mass m^*, mobility, relaxation time τ, and resistivity ρ_0 if the other parameters are known.

B-Spline dispersion, on the other hand, has no physically-retrievable values and is purely a fitting function to accurately match the ellipsometric data. B-Spline uses a set number of nodes for basis-functions to describe the optical functions and find the best match for Ψ and Δ. B-Spline can be implemented with Kramers-Kronig consistency to keep the optical functions physically

plausible, but it does not allow for the extraction of any physical parameters from the fit. This method is very easy to implement and can then be converted to general oscillators and *vice versa*. The optical model is used to generate Ψ and Δ for a given sample structure using parameters such as thickness and refractive index for each film, along with the substrate optical functions. The model-generated data are compared to the measured Ψ and Δ spectral data using a single output value to quantify the fit quality. Mean squared error (MSE) is a typical representation of how well the modeled data matches the SE data (see Methods). This formalization provides a single value for how well the model fits the data, but we note that there is no ideal universal MSE value, as the value depends upon the assumptions, known quantities about the material, and measurement noise. A major limitation of the MSE is a tendency to define a "correct fit" based solely upon its minimum value. If a correlation exists between multiple unknown fit-parameters, then many combinations of values can manifest in an acceptable MSE.

Dielectric films have negligible loss so the refractive index is purely real. For dielectric films of unknown thickness, the balance of variables is data-heavy to Ψ and Δ, see Figure 3(a), as the parameters fit are refractive index $n(\lambda)$ and thickness t while the measured values are $\Psi(\lambda)$ and $\Delta(\lambda)$. This data saturation allows for very nice data fits to determine both thickness and refractive index for many material systems.

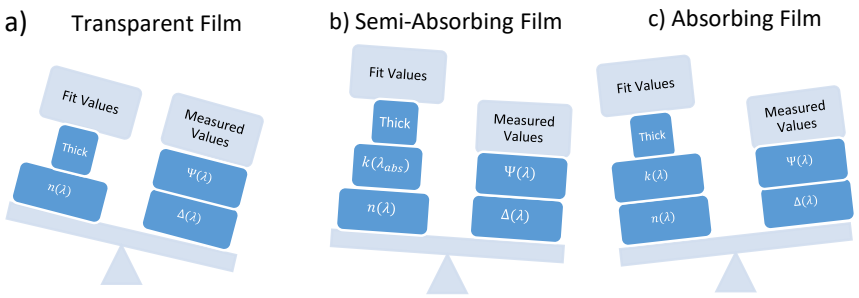

Figure 4 Comparison of data balance for a) transparent film, b) semi-absorbing film, and c) thin absorbing film. For transparent and semi-absorbing films, the ellipsometry measurements are sufficient to allow for the unique retrieval of the refractive index and thickness. However, for absorbing films, the ellipsometry measurements alone are insufficient to allow for a unique retrieval of the optical properties and thickness, and additional information should be added to improve the confidence of the result.

When loss is added to a system the refractive index becomes complex leading to two values, n and k where $\tilde{n} = n + ik$, at each wavelength. For some materials, such as doped-semiconductors, a region exists where k is negligible so the balance of variables continues to favor Ψ and Δ, see Figure 4c as the thickness can be uniquely fit within the transparency window and fixed. However, in very thin films with absorption across the spectrum, the balance of data no longer favors the measured values, Figure 4(c), which can lead to fit ambiguity. Multiple methods exist for overcoming the data discrepancy [74,75]: adding RT measurements, interference enhancement [71,74], multi-sample analysis, and *in situ* ellipsometry [69].

In this work, SE measurements are conducted on a single titanium nitride film of unknown thickness, using various metrics to analyze the results. Later, a case study comparison of three films, grown with the same conditions but of different unknown thickness, is presented. We demonstrate the combination of SE and T measurements to overcome the data content shortage. To facilitate T measurements, the absorbing thin film must be on a polished, transparent substrate. This can be counterproductive to the simplicity of ellipsometry, due to backside

reflections from the substrate, but can generally be managed [76]. Transmission must also exist at some point in the material which limits the thickness of the absorbing film and the substrate type.

2.2. Characterization of Titanium Nitride Films

Titanium nitride is metallic with a color similar to gold; therefore, when fitting with general oscillators, we use a Drude oscillator and two Lorentz oscillators to model the transitions [63]. The film absorbs across the spectrum and typically has a plasma frequency between 450 and 650 nm, which, along with quality, varies greatly by the method and parameters of growth. Due to this variation in materials, the data is presented with very few assumptions of the expected thickness or permittivity values.

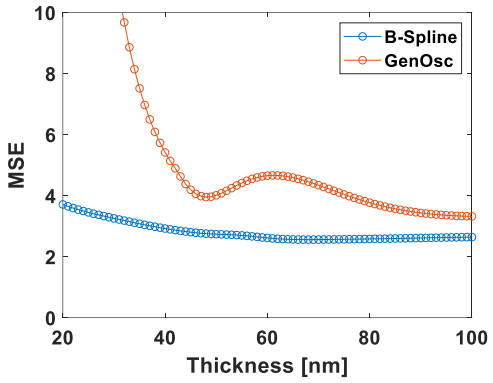

Figure 5 Mean Squared Error (MSE) vs Thickness for a thin TiN layer using a general oscillator and B-Spline dispersion equations to fit only SE data. The general oscillator shows a distinct minimum at 48 nm and the B-Spline has a flat, low MSE fit from 20 to 120 nm leading to a large ambiguity in fit quality.

When fitting materials for both refractive index and thickness, a popular tool for checking the certainty of value is to plot parameter uniqueness. Figure 5 is an example of thickness uniqueness plots for the analysis of SE data when describing the TiN layer using a general oscillator (GenOsc) (red) and B-Spline (blue) dispersion equation. A sharp 'v' shape in parameter uniqueness shows

a high certainty of the fit to a specific thickness. A sharp 'v' is seen in the modeling of GenOsc for a fit of 48 nm with a reasonable MSE value near 4, but the B-Spline has an MSE below 3 for a wide range of thicknesses (from about 40 nm to well beyond 100 nm). At thicknesses of 90 nm for this material, the thin film is considered optically opaque, so the thickness no longer has a role in the fit-quality as all secondary reflections are quenched. The GenOsc preferentially fits with 48 nm layer thickness but a less prominent fit also occurs when the layer is over 100 nm. To properly characterize this material using either method, more must be known about the material.

Table 1: Correlation matrix between thickness, resistivity, and scattering time using GenOsc models. The correlation between thickness and resistivity or thickness and scattering time being close to ±1 is non-ideal, meaning there is no uniqueness to the fit.

	Thickness (nm)	Resistivity (Ω·cm)	Scat. Time (fs)
Thickness (nm)	1	0.934	-0.931
Resistivity (Ω·cm)	0.934	1	-0.992
Scat. Time (fs)	-0.931	-0.992	1

Another way to check the uniqueness of fits is to calculate the correlation matrix, which shows the interdependence between fitting parameters. A value of ±1 corresponds to a perfect correlation where parameters A and B can be interchanged and still achieve the same result. Correlation near zero is ideal for fitting parameters as no variation in a variable can be countered by another parameter to achieve the same result. A measured correlation matrix is shown in Table 1 where the correlation between resistivity and scattering time is shown to be inversely correlated (e.g. approximately -1). By examining the Drude formula used to model the film, this

correlation is expected and does not affect the quality of fit; it simply means there is no information to separate these two values and only one is required to fit the data with the other fixed. To retrieve information about the film resistivity from SE measurements, we would need to separately know the accurate scattering time. A more troublesome correlation is between thickness and the dispersion model equations (here, both resistivity and scattering time). This correlation suggests that an arbitrary thickness increase can be compensated by a similar factor increase in resistivity. Figure 6 shows a two-dimensional uniqueness plot corresponding to thickness and resistivity. The trough representing the minimum MSE is elongated, demonstrating this correlation between thickness and resistivity.

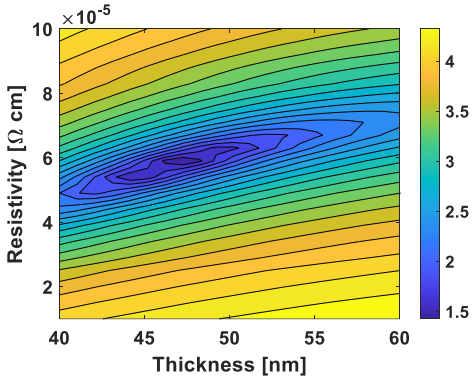

Figure 6 Logarithmic surface plot of Mean Squared Error for various resistivity and thickness combinations. The elongated trough shows a strong correlation between thickness and resistivity which induces a large variability in material properties.

B-Spline produces a similar issue as shown in the thickness uniqueness plot (Figure 6). The basic functionality also works to produce a high correlation between each node, which results in a flat, low MSE, curve without a sharp 'v'. To demonstrate the variety of material characteristics this can produce, the permittivities and figure of merit values are compared for TiN films fit from 30 nm to 70 nm in. We see a variation in the figure of merit of almost 3× from minimum to maximum and a similar spread is found when fitting with GenOsc (not shown).

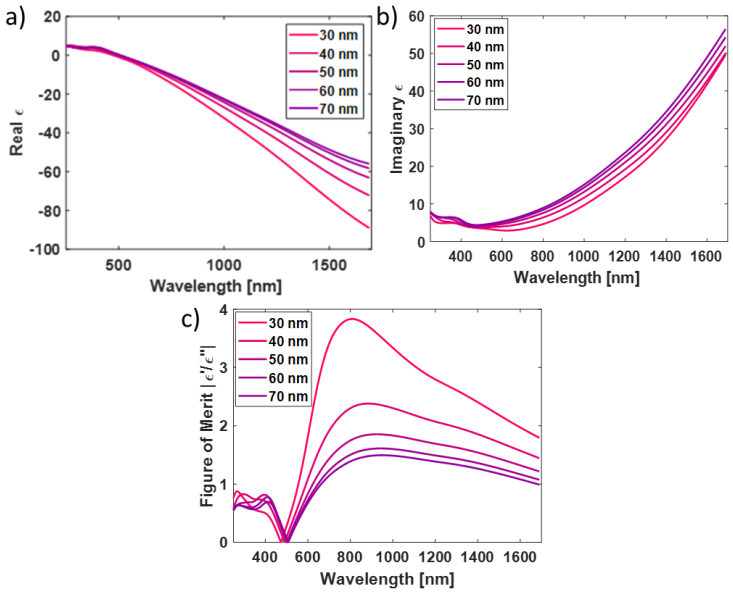

Figure 7 B-Spline fit for various thicknesses calculated real and imaginary permittivity a) and b) and figure of merit c). Despite each fit having a low Mean Squared Error fit, a large change in optical properties is seen between each fit with almost 3× variation.

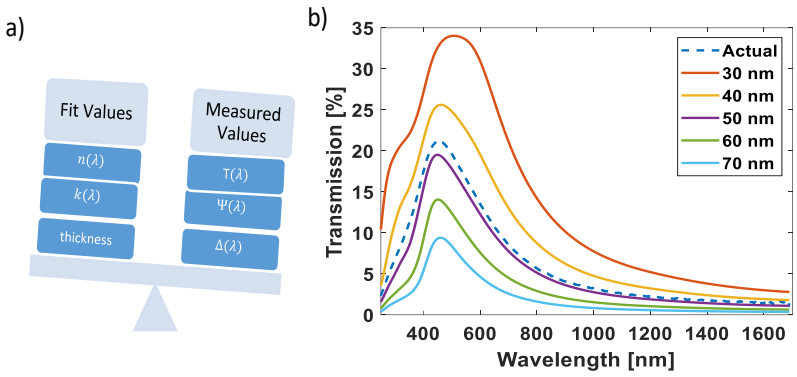

Figure 8. a) Balance of variables with transmission included. The balance favors measured values, which is ideal for fitting. b) Transmission measured and generated with B-Spline fits shown in Figure 5. The 50 nm fit is closest to the measured transmission of the film.

In this case, neither the GenOsc nor the B-Spline fit the SE data confidently and more data is necessary to accurately determine the material properties. Accurate thickness measurements could be taken via methods such as transmission electron microscopy or step etching, thereby reducing the unknown variables. When we add T data the balance of variables favors the measured values, see Figure 8(a), as we have both SE and T data for each wavelength. Even when

some spectral regions are completely opaque, only a few transmission data points are necessary to allow for film characterization.

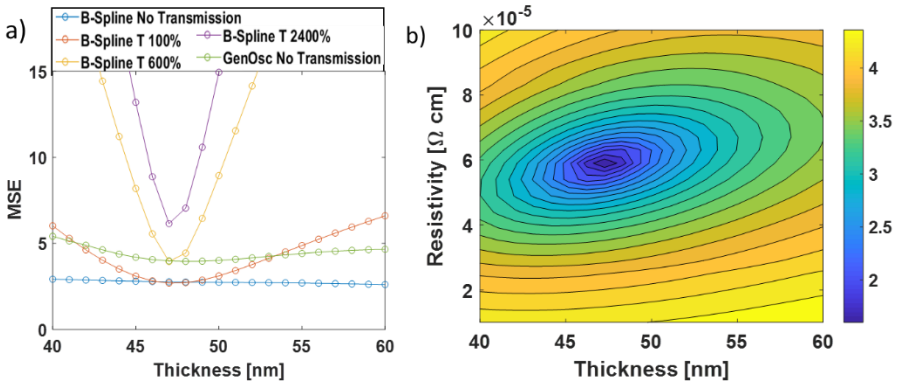

Figure 9 a) Mean Squared Error vs thickness for various weightings of transmission. Fits with transmission included having a sharp 'v' providing a unique fit for thickness at 47 nm. b) Two-dimensional parameter uniqueness comparing resistivity and thickness. The conical trough is ideal, showing a unique fit between the thickness and resistivity parameters.

Table 2: Correlation matrix with transmission included in the calculation. The correlation between thickness and resistivity or thickness and scattering time is no longer close to ±1 so the correlation is broken

	Thickness (nm)	Resistivity (Ω·cm)	Scattering Time (fs)
Thickness (nm)	1	0.324	-0.237
Resistivity (Ω·cm)	0.324	1	-0.949
Scattering Time (fs)	-0.237	-0.949	1

Adding T data, we can simply calculate the expected T from the previous B-Spline results at various thicknesses and compare to the measured T. Figure 8(b) shows that the results calculated from the 50 nm fit results produce the closest match to T. This visual check may be enough information to consider the film to be about 50 nm thick and use this to optimize our permittivity. However, it is best to consider the SE and T data simultaneously as the thickness and permittivity

are regressed to the best-fit. The standard approach considers the single T data to be "weighted" as a single measurement, compared to the multiple-angles from SE measurements. To increase the importance of the T, when three angles of $\Psi(\lambda)$ and $\Delta(\lambda)$ where measured, we increase the T weighting to 600% such that T and SE curves are more or less equivalent. As seen in Figure 9(a), when T is added, the uniqueness plot produces a sharp 'v'. This 'v' is sharper for higher T weighting, including tests with T, weighted at 2400%, but the MSE also increases. This gives a confident thickness of 47 nm for the film. T data also breaks correlation as can be seen in Table 2 and Figure 9(b). As a result, the previously elongated trough in the two-dimensional parameter uniqueness has been condensed such that a large change in thickness cannot be compensated by a change in resistivity.

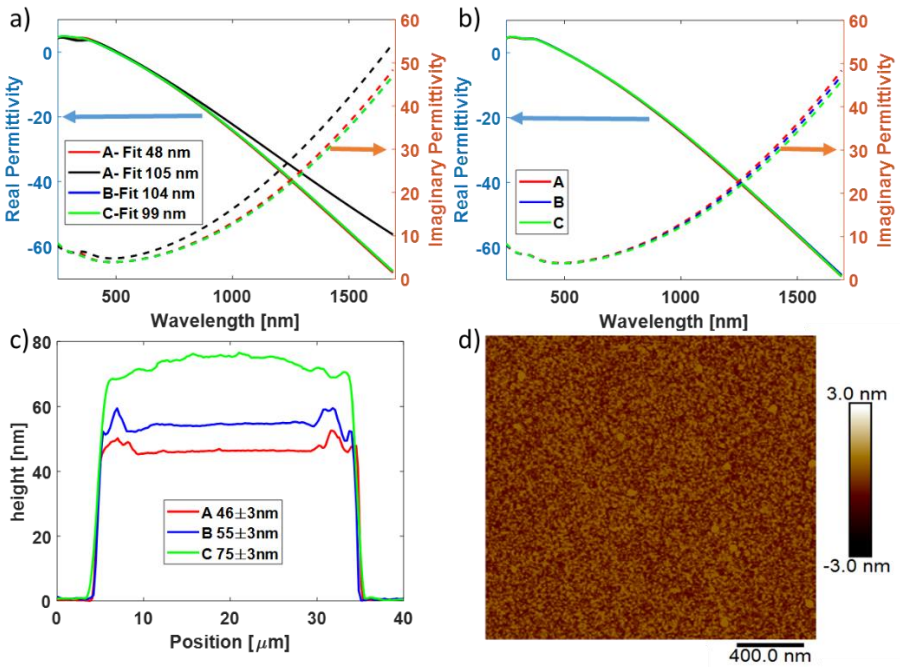

Figure 10 a) Real (left axis) and Imaginary (right axis) permittivities of samples A, B, and C when using SE data alone fit with a Drude and two Lorentz oscillators (GenOsc). The fit thicknesses have clear deviations from linear growth. b) Real (left axis) and Imaginary (right axis) permittivities of samples A, B, and C with transmission measurements fit with a Drude and two Lorentz oscillators(GenOsc). The trend is now seen that material quality does not strongly depend on the thickness of the film and a linear growth rate is found. c) AFM measurement of a step in the TiN films verifying the thicknesses obtained. The curvature seen in C is attributed to etching under the mask, more prevalent in C due to additional time of etching. d) AFM measurement of sample A showing <1 nm surface roughness. Other samples illustrate similar roughness.

Finally, we consider three films; film A, which has been the subject of the previous sections, along with films B and C. The growth method is plasma-enhanced atomic layer deposition, a technique with a consistent, but unknown, growth-rate when other deposition parameters are kept constant. The three films were grown to different unknown thicknesses to verify whether the thickness of ultrathin films impacts the optical properties. Film A should be the thinnest with film C being the thickest based on deposition cycle numbers. First, the films were characterized with SE only (without T) using a GenOsc with one Drude and two Lorentz oscillators. Film A produced best fits at 48 nm and 105 nm, film B at 105 nm, and film C at 99 nm). All three sample optical

properties are plotted in Figure 10(a); the optical properties of the three films are shown to vary only for the lowest thickness in film A but the assumed thicknesses are incorrect.

However, the large discrepancy between expected film thickness and fit thickness led to the addition of T spectra for the three samples. After fitting both SE and T, we find that the actual thicknesses are 47 nm, 58 nm, and 80 nm, which is a linear growth rate of 0.07Å/ cycle between samples. The results of this correct modeling are shown in Figure 10(b) and there is no significant change in optical properties between films. For parity, the thicknesses of the films were also measured using atomic force microscopy across a step profile of the film fabricated through photolithography and wet etching. The resulting thickness values are found to agree with the ellipsometry measurements, Figure 10(c), within the ±3 nm error of the measurement. Surface roughness was measured using AFM to find <1 nm RMS, shown in Figure 10(d).

3. LARGE INTRABAND INTENSITY DEPENDENT REFRACTIVE INDEX IN ENZ

The intensity dependent refractive of ENZ materials has been studied in literature through experimental means without significant theoretical direction. Our work aims to holistically investigate all nonlinearities that induce an intensity dependent refractive index in ENZ films. Initial investigation lead to an understanding that the nonlinear process is absorptive in nature.

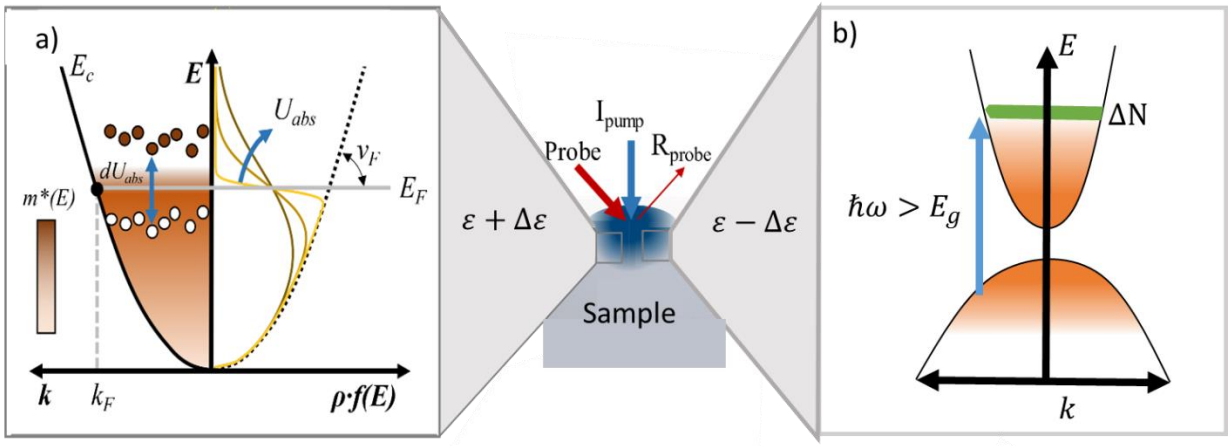

Figure 11 a) Schematic of the intraband nonlinearity in ENZ materials, where the reflectivity (permittivity) of the material is changed through the application of a pump beam. The change in permittivity occurs due to a modification of the effective mass of the electron sea as the absorbed pump energy elevates electrons to higher energy, higher mass states. b) Schematic of the interband nonlinearity where the permittivity is decreased through the absorption of photons with energies larger than the band gap, causing free carrier generation. Figure adapted from [4].

Two types of absorption can be investigated as the cause of this effect, depending on the spectral location of the pump. Excitation in the longer wavelengths of visible through near-infrared, intraband absorption is the dominant absorption mechanism. This form of absorption promotes electrons from lower in the conduction band to higher energies (Figure 11a) causing a redshift in plasma frequency as will be described in depth in Section 3.2. In the UV optical region, the main absorption effect is interband absorption; electrons are promoted from the valence band to the

conduction band (Figure 11b). This induces additional free carriers and blueshifts the plasma frequency as will be described in Section 4.2.

3.1. Background: Intraband Nonlinearity of Epsilon-Near-Zero Media in Literature

The search for an ideal nonlinear material has been a fruitful study [7,77–80] which continues to provide new opportunities for research from organic materials [79,80], to designer glasses [81], plasmonics [82–84], and metasurfaces [85–87]. One promising effect that has been shown to boost nonlinearities in metasurfaces [1,88–94], plasmonics [95–97], and thin films [1,6,24,26,35,40,98–100] is epsilon-near-zero (ENZ). A number of works have explored intraband nonlinearities in ENZ materials from various perspectives of experimental data [5,6,24,101,102]. Typical experiments have been conducted with Z-scan [24,89], R-T [5,6], and beam deflection [26,103] to measure n_2 of ITO and doped ZnO films. The results have consistently provided large nonlinear responses; however, modeling and exact values have varied work to work and are not perfectly corroborating.

An early, influential, work in the field was conducted via Z-scan and RTA measurements by Boyd et al [27]. Z-scan is a technique where a film is moved along the incident axis, near the focus of a beam which acts as pump and probe. The change of the refractive index in the film acts as a lens focusing or defocusing the beam. By comparing the total transmission and the alteration of transmission collected into a small slit, the change in the index can be modeled [104]. Changing the position to the focus (where the name Z-Scan originates) provides an intensity dependence and normalization.

Further exploration was given through transient RTA, where a pump induces a change in the film, which is probed by a weak pulse. These measurements allow for back-calculation of optical

parameters through the transfer matrix method (TMM). This allows for time dependent measurements by sampling the material's response a different points in time, achieved by varying the relative arrival time at the sample of the pump and probe pulses (see Section 6.1.2). Intensity dependent measurements of ITO are taken through both methods and large nonlinearities are found. Off normal angle enhancement is found to be quite large as is predicted through D-Field continuity. Furthermore, saturation effects are found near $150\ GW/cm^2$ [27]. Modeling of this effect is completed through Two Temperature Model [105].

Other materials and measurements have been taken to establish n_2 in nondegenerate cases. Spectral data has been taken by Boltasseva, Faccio, et al. [6] to explore nonlinearities beyond intensity dependence. These measurements were taken through RT measurements at multiple intensities in AZO, results provided in Figure 12(a-c). This work was modeled with a Kerr nonlinearity with a varying $\chi^{(3)}$, Figure 12b.

Time dependence measurements having a clear relaxation rate, and polarization insensitivity verifies that this effect is not a bound electron polarization effect as described by a Kerr effect, confirmed via the overlap of parallel and perpendicular responses in beam deflection results [24].

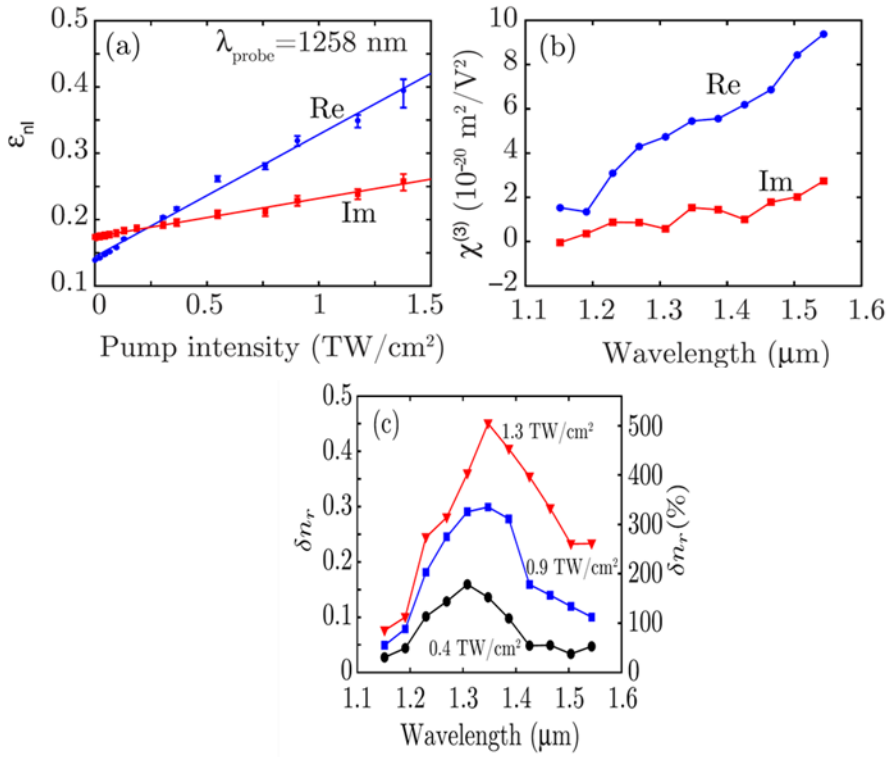

Figure 12 Nonlinear changes in permittivity as a function of intensity (a) and probe wavelength (c). The $\chi^{(3)}$ used to model this effect is given in (b). Figure taken with permission from Caspani et al [6] .

3.2. Kinetic Adaptation of Intraband Nonlinearities in Epsilon-Near-Zero Media

Here, the theory describing the nonlinear process of intraband intensity-dependent refractive index (IDRI) in telecom, Drude, ENZ materials such as ITO, AZO, and GZO, is outlined. For a full exploration of this phenomenon, see the publication, Secondo et al. [4], which will be summarized here. Literature has defined effective mass as the band curvature effective mass for most cases, however, some works have proposed the use of a transport effective mass. However, in the pursuit of holistic understanding, our research worked to derive effective mass for ourselves beginning with the change in the Fermi surface due to an applied field.

$$\delta k = -\frac{qE}{\hbar} \tag{25}$$

If the velocity of an electron is considered for a particular direction it is found as:

$$v_z = v\cos\theta = v_F \frac{k_z}{\sqrt{k_z^2 + k_\perp^2}}. \tag{26}$$

Taking the effective mass as the change in velocity compared to the rate of change in momentum, $\frac{dv}{dk}$. Taking this full derivative:

$$\frac{dv_z}{dk_z} = \frac{dv(k)}{dk_z}\cos\theta - v(k)\sin\theta\frac{d\theta}{dk_z} = \frac{dv(k)}{dk}\cos^2\theta + \frac{v(k)}{k}\sin^2\theta\,. \tag{27}$$

After taking the time average of the sinusoidal terms, the change in velocity is found as:

$$\delta v_z = -\frac{q}{i\omega\hbar}\left[\frac{2}{3}\frac{v(k)}{k} + \frac{1}{3}\frac{dv(k)}{dk}\right]E = -\frac{q}{i\omega m^*(k)}E. \tag{28}$$

The result is found that the effective mass is a combination of these two previously mentioned effective masses:

$$m^*(E)m_0 = \hbar\left(\frac{2}{3k}\frac{dE}{dk} + \frac{1}{3\hbar}\frac{d^2E}{dk^2}\right)^{-1}. \tag{29}$$

As shown in Figure 13, in the parabolic region, this is the same as either of the previous models. When the parabolic assumption is violated, this equation presents an effective mass that is a weighted average of the other two definitions.

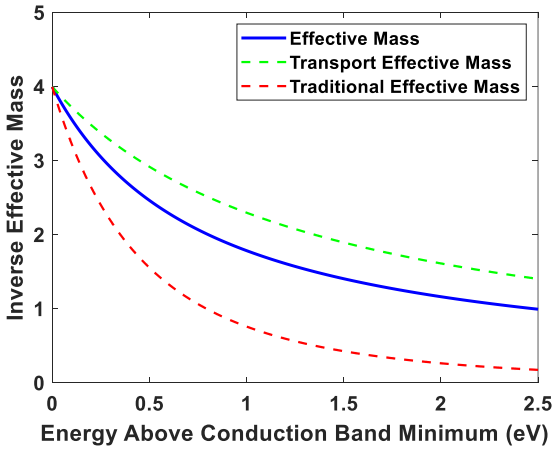

Figure 13: The traditional, transport, and our weighted average effective mass increase (shown above as inverse decreasing) as the energy above the conduction band minimum increases. The traditional effective mass begins to tend toward infinity at high energies.

If we begin to consider the implications to the Drude formula, we find that if carriers are away from the CBM, their effective mass will vary. This means we can no longer consider one effective mass, but rather, must average the effective mass amongst the carriers. This results in a revised Drude formula:

$$\varepsilon_r = \varepsilon_\infty - \frac{q^2}{\varepsilon_0 m_0} \frac{1}{\omega^2 + i\Gamma\omega} \int_0^\infty \frac{f(E,\mu,T_e)\rho(E)dE}{m^*(E)} \qquad 30$$

where $f(E,\mu,T_e)$ is the Fermi-Dirac distribution with respect to energy, chemical potential, μ, an electron temperature, T_e, $\left(f(E,\mu,T_e) = \frac{1}{e^{\frac{E-\mu}{k_B T}}+1}\right)$ and $\rho(E)$ is the electronic density of states (DOS). Since m^* tends to be higher at higher energies, an increase in carrier concentration causes a higher average effective mass. Furthermore, if the electron temperature rises, the average effective mass increases as well. The temperature rises due to absorbed energy density, dU_{abs},

from intraband excitation. This temperature rise can be found through two conservation equations, the first for carrier concentration and the second for energy:

$$\int_0^\infty f(E,\mu,T_e)\rho(E)dE = N \tag{31}$$

$$\int_0^\infty f(E,\mu,T_e)\rho(E)dE - \int_0^\infty f(E,\mu_0,T_{e0})\rho(E)EdE = dU_{abs} \tag{32}$$

where subscripts denote unexcited chemical potential and electron temperature. The energy density absorbed can be found through $\frac{A(\omega)I\tau}{d}$ where τ is the system relaxation rate, d is the material thickness, and $A(\omega)$ is the absorptivity of the film $(1-R-T)$. This absorptivity can be enhanced through pump wavelength choice, film loss, and slow light enhancement, finding a delicate balance between increasing traditional absorption by adding loss and enhancing absorption through slow-light by reducing loss.

From the calculations of μ and T_e, the excited material's effective mass can directly be calculated as in Equation 29. By calculating the linear permittivity and the excited permittivity (Figure 14), and taking the difference, the nonlinear susceptibility is found. Unlike traditional IDRI, the effective n_2 found through this process is not constant as the effect is not due to bound polarization effects given by $\chi^{(3)}$ (Equation 8). Instead, the shift in plasma frequency provides a change in the index.

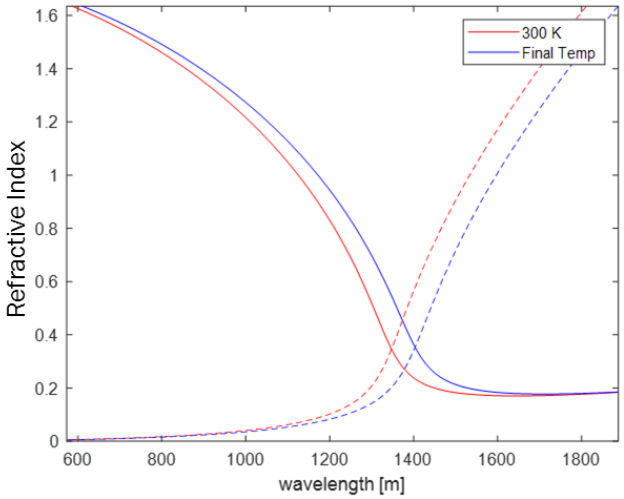

Figure 14: When the plasma frequency of a material shifts, the effects can be seen far away from ENZ, the effect is shown here for the $0.4\ \mathrm{TW/cm^2}$ intensity in Figure 15, the change is still visible at twice the energy of ENZ.

For an AZO film in literature, we were able to show that this model adequately describes the nonlinear effect through these linear material processes of absorption and relaxation (see Figure 15).

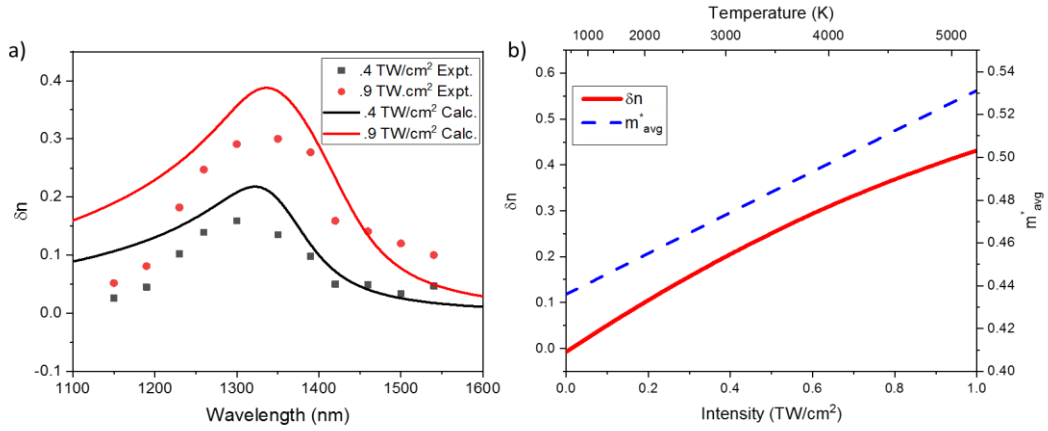

Figure 15 a) The change in refractive index due to a $0.4\ (TW/cm^2)$ (black) and $0.9\ (TW/cm^2)$ (red) pump at 780 nm. Using a relaxation rate of $\tau = 170\ (fs)$ [5] on a Gaussian pulse shape with maximum pump with 100 fs full-width half-maximum. A close fit between experimental [6] and theoretical responses is obtained through a deterministic model. b) The peak δn and average effective mass of carriers versus the applied pump intensity for the AZO sample. (Figure is taken with permission from Secondo et al [4] with experimental data from Caspani et al. [6]).

Furthermore, a figure of merit was proposed that allows the comparison of various materials and loss conditions to aid future research efforts and give insight into the important mechanisms involved. This figure of merit can be split into three sections of focus (shown through brackets).

$$FOM = A_{pump}\left[\frac{1}{m^*_{avg}}\frac{dm^*}{dE}\right]\left[\frac{1}{N}\frac{dn_{probe}}{dm^*_{avg}}\right] \quad 33$$

First, the energy must be absorbed to generate excess energy in a material, given by A_{pump}. This absorption can be enhanced and optimized through pump wavelength choice and material characteristics. Film absorption is highest in the range near ENZ due to a tradeoff between transmission and reflection being dominant (shown in Figure 16). At moderate positive permittivities, low reflection is observed, however, the film is not metallic enough to have considerable intraband absorption. On the long side of ENZ, negative permittivities are highly reflective, reducing the ability to absorb due to limited field entering the bulk of the material. For low loss films (n<<1), ENZ provides an enhancement due to slow light discussed in Section 1.5 allowing for an extended effective length of the material. In high loss films, this enhancement goes away as $n > 1$, however, these films benefit from a reduced impedance mismatch.

Next, for a significant change in effective mass to occur, the initial effective mass is ideally small and changes drastically as electrons are excited to higher energies. The initial effective mass works as a normalization factor for the dispersion of effective mass. This reduces the efficiency of high carrier concentration films due to their large effective mass from having more carriers initialized away from the CBM.

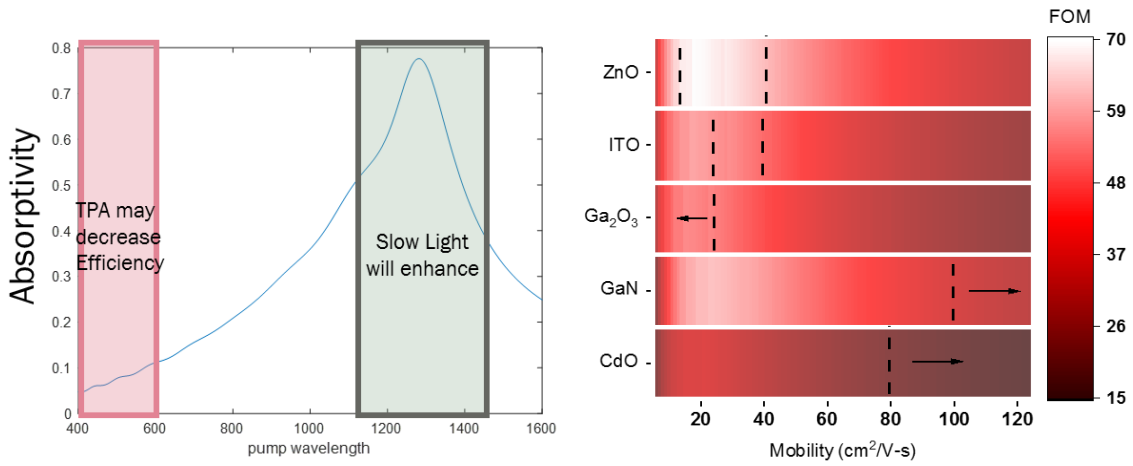

Figure 16: (left) dn generally follows the trend of absorptivity due to being caused by the absorption of the material, however, near NZI effects, slow light is expected to enhance absorption and enhance refractive index modulation. In the region $\mathrm{E_{pump}} > \mathrm{E_g}/2$ two-photon absorption may weakly decrease the efficiency of the process by generating free carriers. (right) The figure of Merit calculations for various materials as given in Secondo et al [4] based on hyperbolic band fits, reprinted with permission.

The final considerations are for how difficult a film is to modulate. The higher the carrier concentration is, the more energy is required to generate a shift in the average effective mass. Next, the refractive index dispersion with respect to a change in effective mass describes how much effective mass change is necessary to have the change be visible in the index. A high background permittivity causes this term to be high due to the extra curvature from being a steeper Drude dispersion; however, the high background permittivity also requires more carriers to generate a high plasma frequency providing an interesting trade-off. This term is also loss dependent as the curvature is sharpened at a low loss, and shallows at a high loss, balancing with the absorption from term 1.

Limited qualitative discussion of the specifics of comparison will be presented here with a more in depth, quantitative discussion following the multi-pump discussion in Section 5.2 to directly compare IR and UV results. The FoM calculations for the five films considered here are taken as

a function of loss through a change in mobility. The peak in absorption for the considered films occurs near a mobility of $20 - 30\ \left[\frac{cm^2}{V \cdot s}\right]$ where reflection is low due to a low impedance mismatch with air ($\tilde{n} \approx 0.7 + i0.7$, $|\tilde{n}| \approx 1$). For this calculation, AZO and ITO have very similar results due to a similar initial carrier concentration and effective mass, deviating mainly through the band curvature. The other three films suffer from large background permittivities, requiring larger initial carrier concentrations to achieve the considered ENZ. This also limits the effective mass by forcing the Fermi level higher in the band, leading to a high initial effective mass. However, the high background permittivity also causes a larger curvature in index at ENZ resulting in a larger dn/dm^*. Despite this, GaN shows itself to be a good nonlinear IR material due to its large nonparabolicity factor $\frac{dm^*}{dE}$. This results in CdO and Ga_2O_3 showing a poor nonlinearity compared to the other three films.

As the thickness directly affects absorption and changes the energy density of an absorbed pump, the thickness of the absorbing film must also be studied. From reflection and transmission measurements, it can be noted that a peak in absorption generally occurs at the crossover of reflection and transmission, due to energy conservation. For a thick film, the denotations of dielectric and metallic regions directly translate to high transmission and high reflection regions respectively. For a thick ENZ film, the transition between a strongly reflective and strongly transmissive conditions occurs fairly rapidly in wavelength (see in Figure 16b). This translates to the highest absorption region being close to ENZ as previously shown. However, for thinner films, the transition does not occur as rapidly. This redshifts the peak in absorption to well beyond the ENZ wavelengths. For a film with ENZ at 1.3 μm and a loss of 0.4 at ENZ, the trend of peak absorption is shown for film thicknesses 50 nm to 500 nm (Figure 17). For this theoretical film,

the transitional region of absorption occurs at thicknesses between 100 and 200 nm, with ENZ pinning occurring for thicknesses greater than 250 nm which continually become more narrow with increasing thickness. This transition is both dependent on the ENZ wavelength and the loss of the film. Low loss films will have a sharper transition between transmission and reflection in wavelength, resulting in a more direct pinning of the absorption to ENZ while lossy films have a slower transition, requiring a thicker film to pin to ENZ. For overall absorption efficiency, it must also be noted that absorption follows an exponential decay trend leading to additional thickness producing a diminishing effect on overall efficiency. Thus, depending upon the loss of the film there will be a maximum thickness after which the addition of more material will not strongly affect the ability of the film to absorb. This thickness is the skin depth ($d = 1/\alpha$), which is typically ~1 µm at ENZ.

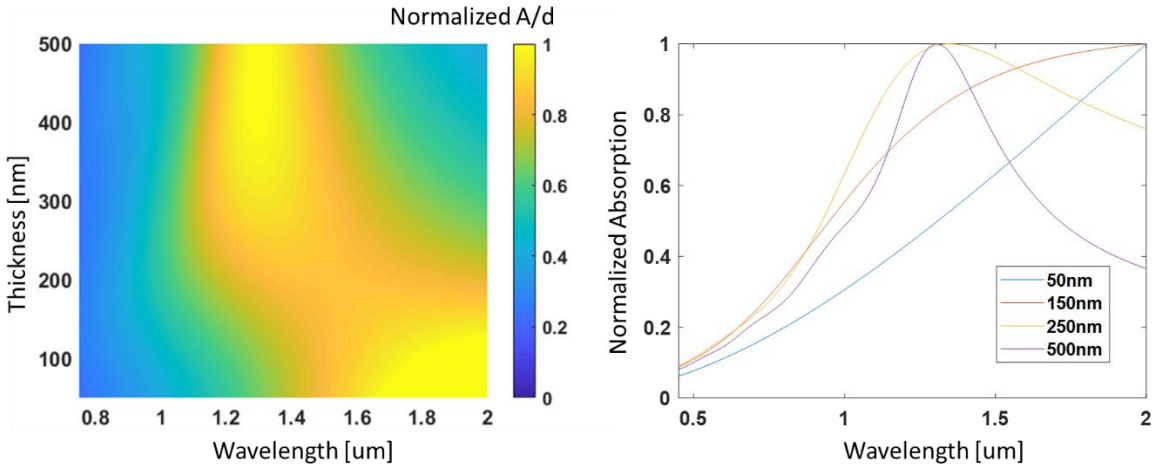

Figure 17 (left) The normalized absorption efficiency, absorption divided by thickness, for a film with ENZ at 1300 nm and low loss. This shows the ideal pumping wavelength to maximize nonlinear response of the material. Thick films pin the ideal pump wavelength to the ENZ region of the film, while thinner films have this region at longer wavelengths. (right) The normalized absorption as a function of film thickness clearly shows the pinning transition between 150 nm and 250 nm and the continued narrowing of the ideal wavelength to ENZ.

Having studied the material centric effects provided in the figure of merit and the experimental practical considerations such as pump wavelength, probe wavelength, and film thickness, theory enables us to look further into the ideal performance choices available. Certain experimental considerations can be found from investigation that allow us to take our film and find a preferred experimental set up; or on the other side, a film may be chose to operate well for a given experimental set up. For example, if a film is significantly thin, using a pump with a longer wavelength may enhance the experimental results. This result is contrary to the general viewpoint discussed in literature, which generally seek to explore degenerate use at ENZ [106]. If the pump and probe are required to be degenerate (or only one beam such as a Z-Scan experiment), utilizing a slightly thicker film to pin the ideal pump wavelength to the preferred probe wavelength of ENZ.

3.3. Gallium Nitride as an Intraband Nonlinear Medium

Among the materials explored through hyperbolic band modeling, gallium nitride stands as a film whose band structure deviates the greatest at energies of interest (as shown in Figure 18). As the effective mass is inversely proportional to both the first and second derivatives of the $E-k$ relationship, a band flattening at lower energies will have a more drastic effective mass dispersion, Figure 19a,b. In GaN this effect is evident and our exploration required direct calculation of band curvatures rather than model fits such as the hyperbola. For this, density functional theory (DFT) was applied to a gallium nitride film with doping $\approx 5 \times 10^{20}[cm^{-3}]$ allowing for direct calculations from numerically derived band structures.

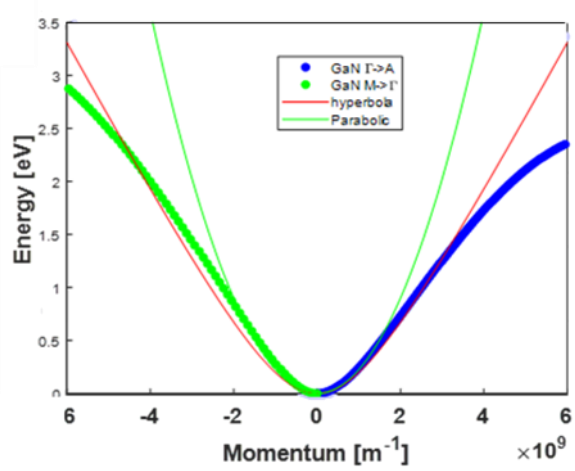

Figure 18: Gallium nitride band structure from DFT calculations compared to matched hyperbolic (red) and parabolic (green) approximations.

The result of the DFT calculations, conducted by Dr. Dennis Demchenko, shows a conduction band maximum under 2.5eV, shown in Figure 19c. At the top of the band, the density of states becomes very large; similarly, the effective mass becomes exceedingly large at moderate energy levels compared to the hyperbolic expectations, see Figure 19b. As our effective mass can be described as a combination of the curvature effective mass and the transport effective mass, it is worth discussing the interaction of each of these individually. The curvature effective mass diverges at the inflection point of a curve as $\frac{d^2E}{dk^2} = 0$ in a linear region (close to 1 eV above CBM in GaN, shown in Figure 19c). On the other hand, $\frac{dE}{dk} = 0$ at the band minimum/maximum so the transport effective mass stays finite throughout the majority of energies of interest, also keeping the overall effective mass finite. However, their interaction produces a region between the inflection point and maximum of the band (~1.6 eV, see Figure 19a) where the effective mass diverges, producing states with very heavy electrons due to the cancelation of the negative curvature effective mass and the positive transport effective mass. The excessively heavy electrons increase the average effective mass significantly, but as the bulk of the electron sea

stays at lower energies, the film remains conductive and has a finite effective mass. Yet, the ability to move carriers via optical excitation into this high effective mass region of the band manifests as an increase in nonlinear response as seen in Figure 19d.

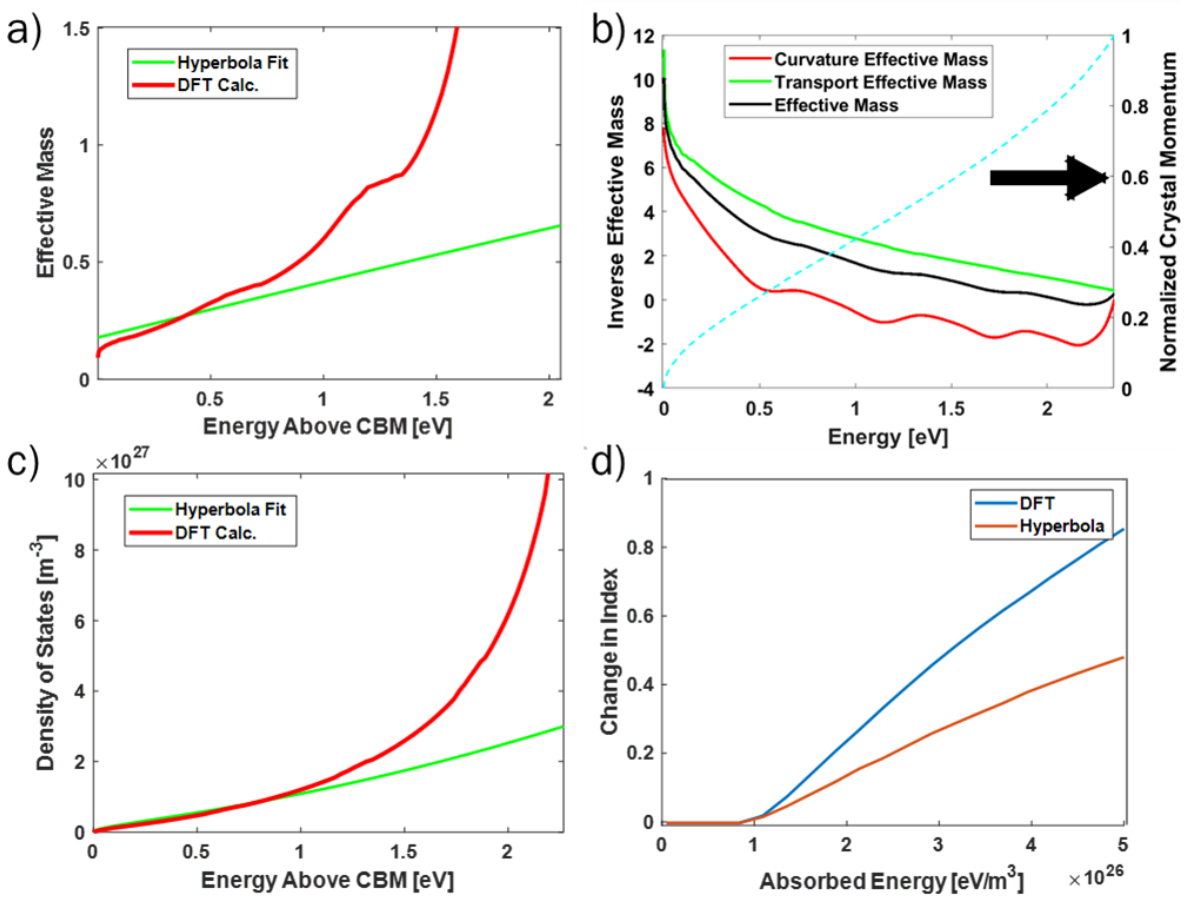

Figure 19 Gallium nitride's band structure strongly deviates from the hyperbolic fit utilized for materials such as zinc oxide. This is obvious when calculating the density of states (c) and effective mass (a) necessary for understanding the nonlinear response. The diverging density of states, paired with a strong dispersion of effective mass predicts an efficient nonlinear response of GaN. b) The inverse effective masses are shown with the band structure from Γ point to the A point (positive momentum Bouillon Zone). The inflection point and conduction band maximum are easily shown through the zero crossings of the curvature effective mass and transport effective mass. d) The nonlinear response calculated through the DFT band structure and the hyperbolic fit for a GaN film with ENZ wavelength of $1700\ \mathrm{nm}$ are compared through the absorbed energy density, $\mathrm{dU_{abs}}$. The large deviation of the actual band from the hyperbola presents a larger dn for a given absorption by the actual film. DFT calculations were conducted through collaboration with Dr. Dennis Demchenko of the Virginia Commonwealth University Physics Department.

Comparing four films, AZO, GaN, CdO, and ITO through DFT calculated band structures shows a good indication of why GaN is a promising film. While all concerned films have a similar curvature that leads to high effective mass changes at high photon energies, GaN approaches this curvature at a significantly lower energy than the other materials. While the background permittivity limits the efficiency of GaN to slightly lower values than AZO and ITO at low pump intensities, this trend changes at high pump intensities. As the electron sea becomes energetic, electrons approach this diverging effective mass faster in GaN than in the other films leading a different curvature than in the other films, see Figure 19d. This allows GaN to continue to outperform other materials at high fluences where this heavy region is accessed. This finding motivates the study of nonlinearities at the edges of the Brillouin Zone and illustrate that GaN is a highly promising material for further studies.

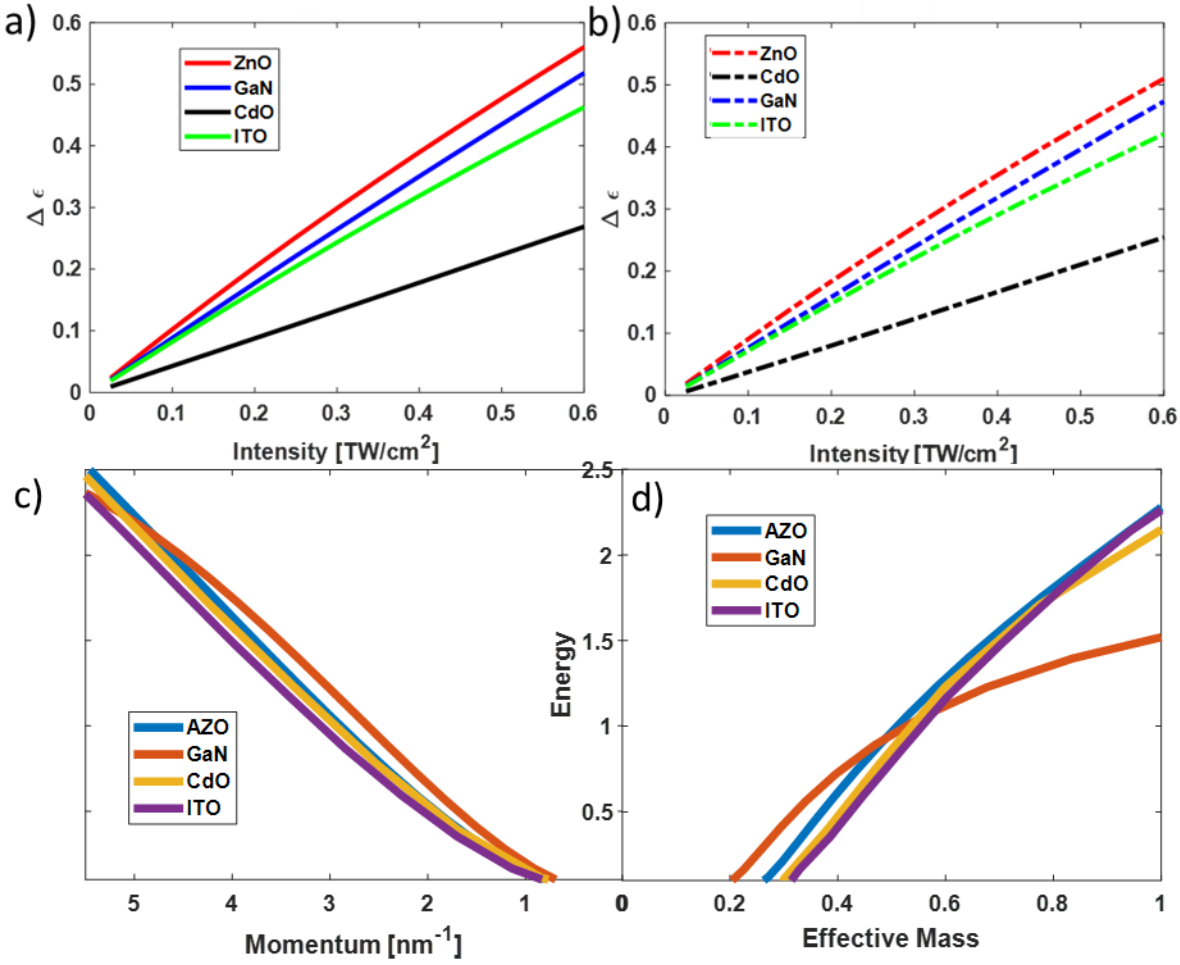

Figure 20 (a,b) The change in permittivity calculated from intraband absorption at 787 nm for AZO, GaN, CdO, and ITO with $\lambda(\varepsilon' = 0) = 1.8\mu m$ (solid, a) and $\lambda(\varepsilon' = 0) = 2.2\mu m$ (dashed, b). While ITO and AZO have nearly the same curvature, GaN shows more promise at high intensities where the highly non-parabolic behavior is seen. This nonparabolic behavior is shown in (c) with an energy turnover beginning near 2 eV while the other materials continue to be hyperbolic. The effective mass as a function of energy between the four films as shown (d); the effective mass of GaN is first to diverge to a large value, allowing for the high effective mass changes occurring at large pumping powers.

4. INTERBAND INTENSITY DEPENDENT REFRACTIVE INDEX OF EPSILON-NEAR-ZERO MEDIA

Revisiting our summary figure for the nonlinear processes in ENZ materials, here we will discuss interband processes shown in Figure 21b. Interband absorption itself is a well-known process where an e-h pair is generated by a photon with energy above the bandgap.

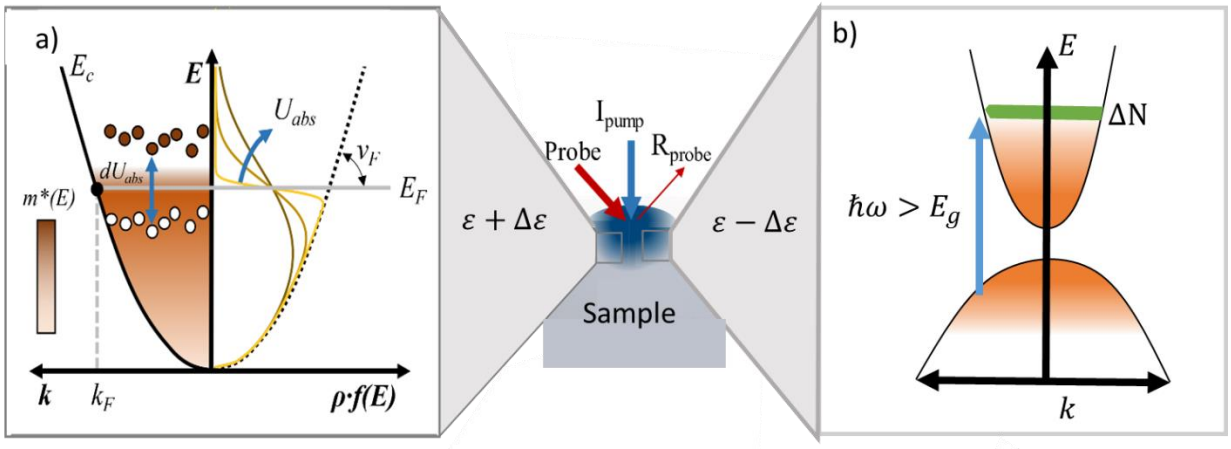

Figure 21 a) Schematic of the intraband nonlinearity in ENZ materials, where the reflectivity (permittivity) of the material is changed through the application of a pump beam. The change in permittivity occurs due to a modification of the effective mass of the electron sea as the absorbed pump energy elevates electrons to higher energy, higher mass states. b) Schematic of the interband nonlinearity where the permittivity is decreased through the absorption of photons with energies larger than the band gap, causing free carrier generation. Figure adapted with permission from [4].

The generation of e-h pairs in large quantities creates perturbations in permittivity outside of the ENZ conditions through the modification of the free-carrier density in the material, giving rise to an intensity dependent refractive index. Here we outline the prior work in interband nonlinearities in ENZ materials and expand our kinetic nonlinear model to encompass these excitations.

4.1. Background: Interband Nonlinear of Epsilon-Near-Zero Media in Literature

Interband nonlinearities have been explored in AZO as an ENZ material, focusing on applications in ultrafast switching for telecommunication wavelengths [109]. In this work, an AZO film with $\lambda_{ENZ} = 1300nm$ and assumed $m^*_{avg} = m^*_\Gamma = 0.25$, where m^*_Γ is the effective mass at the Γ point (a constant effective mass). The nonlinear response is calculated through R-T characterization and is modeled to find the number of carriers generated through absorption and the resultant change in the refractive index. The results provide that for $1, 2.4, \text{and } 3.6\ mJcm^{-2}$ an average change in free carriers of $0.2, 0.5, \text{and } 0.7 \times 10^{20} cm^{-3}$ are induced resulting in index changes of $-0.07 + i0.07, -0.14 + i0.16, \text{and} -0.17 + i0.25$, respectively.

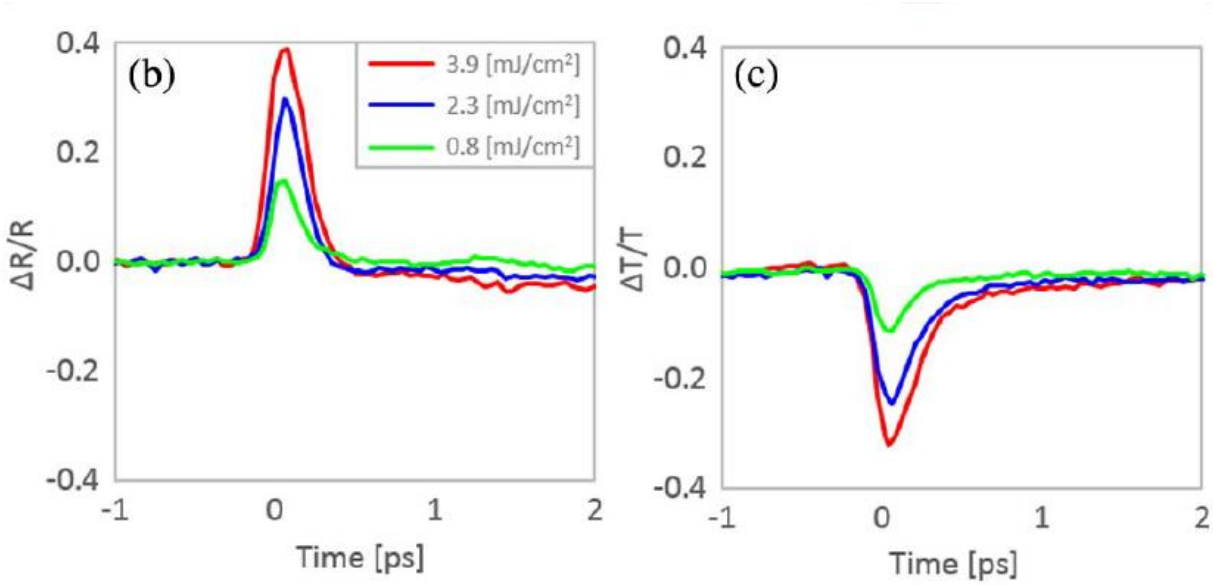

Figure 22 $\Delta R/R$ (b) and $\Delta T/T$ (c) responses for three fluences applied at 325 nm on an AZO film, probed at its epsilon-near-zero point of 1300 nm. The positive change in reflection and negative change in transmission denotes an increased metallicity of the film due to the increased carrier concentration. The figure is taken with permission from [109].

A key difference between the work presented here and our theory is the dedicated focus on effective mass. The prior work considers a constant effective mass for all electrons while our

modeling provides an understanding of the change in effective mass due to the additional electrons. Our model also considers the additional energy of above-band gap pumping and meshes into the theory presented in Section 3, to model more complex systems, shown in Section 5.

4.2. Kinetic Adaptation of Interband Nonlinearities in Epsilon-Near-Zero Media

Interband nonlinearities have been studied to a degree in literature with a physical understanding of exciting an electron-hole pair. Our model provides a small expansion to this effect worth noting. The effective mass of carriers in previous works was taken to be constant. When applied in our model, new carriers have higher effective masses than the average which lowers their efficiency in modifying the plasma frequency by a small factor. We also can introduce an effect, briefly studied in the literature, where pumping well above the bandgap energy provides excess photon energy and results in a similar increase in electron temperature as was found in the intraband case. For these effects, we can extend our governing conservation formulas, Equations 31 and 32, to include a change in carriers dN and excitation energy dU_{UV}:

$$\int f(E,\mu,T_e)\rho(E)dE = N_0 + dN = N_0 + \frac{A_{UV}(\omega)}{d}\frac{I_{UV}\tau_{UV}}{\hbar\omega} \tag{34}$$

$$\int f(E,\mu,T_e)\rho(E)EdE - \int f(E,\mu_0,T_{e0})\rho(E)EdE = dU_{UV} \tag{35}$$

$$dU_{UV} = A_{UV}(\omega)\frac{I_{UV}\tau_{UV}}{d}\left(\hbar\omega - E_g\right). \tag{36}$$

In the case where the pump energy is $\hbar\omega \approx E_g + \mu_{e0}$, T_e should stay constant at $\approx 300K$. When excitation happens significantly above this absorption edge, it will contribute to a temperature rise. This occurs because the electron is promoted to a state well above the Fermi level and must

relax to a state near the Fermi level through electron-electron scattering which increases the electron temperature. Consequently, the effective mass increases a small amount. However, this effect is generally very small when pumping near the bandgap energy. If we consider the change of effective mass as negligible, the permittivity change is easily calculated as:

$$\delta\varepsilon \approx \frac{-dN}{\varepsilon_0 m_0 m^*} \frac{1}{\omega^2 + i\Gamma\omega}. \tag{37}$$

The sign of this change is counter to that of intraband nonlinear responses by moving the plasma frequency toward the blue of the permittivity crossover.

Under extreme pumping scenarios, it is possible for a sufficient number of carriers to be generated such that the chemical potential will temporarily increase, blue-shifting the absorption edge as well, as seen in Figure 23(right). This effect would result in a saturation of the pump absorption for energies very near the bandgap, and would also induce an additional modulation upon the permittivity due to the shift in bandgap. Currently, this saturation effect is not included within the model, and constitutes a promising next step for expansion.

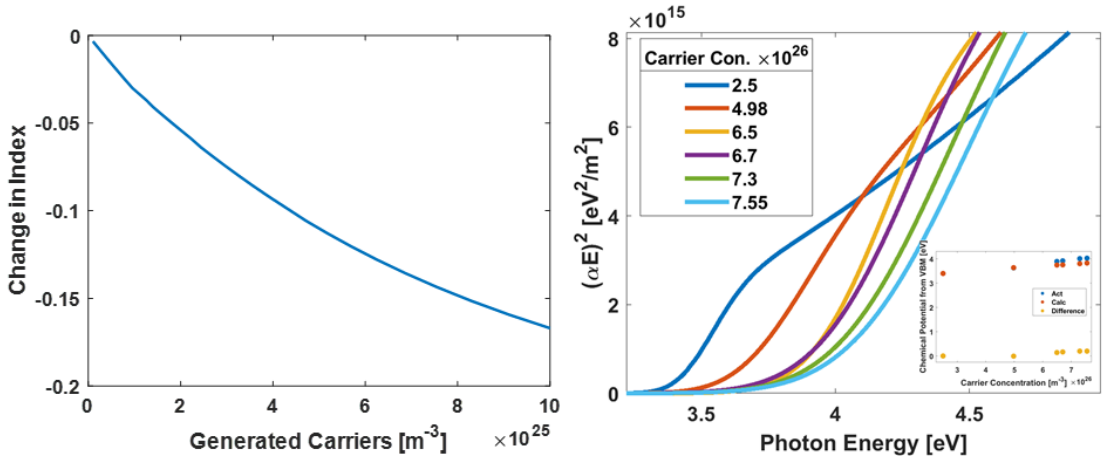

Figure 23 (left)As carriers are generated in the film, the refractive index is reduced due to the shift in plasma frequency. This effect is still limited by the linear index near ENZ. (right) As the number of carriers is increased, either through doping or e-h pair generation, the chemical potential increases, leading to a blue shift of the band edge. This edge is clearly seen through the linear extrapolation of $(\alpha E)^2$ to the x-axis. (inset)The chemical potential extrapolated from $(\alpha E)^2$ compared to the chemical potential calculated from the model. The small error could be due to growth conditions or Moss-Bernstein shift.

Through a similar method to Section 3.2, a figure of merit can be derived. This figure of merit for interband effects can be split into three sections of focus (shown through brackets).

$$FOM = -\left[\frac{A_{pump}}{E_g}\right]\left[\frac{1}{N}\frac{dn_{probe}}{dN}\right]\left[\frac{1}{\mathrm{m}^*}\frac{dN}{dE}\right] \qquad 38$$

First, the energy must be absorbed to generate excess carriers in a material, given by A_{pump}/E_g . This absorption is generally dictated by the energy of the transition, the matrix element, and the joint density of states with band filling. Since the number of carriers generated from absorption is calculated through $\Delta N \propto \frac{AI}{\hbar\omega}$, films with large band gaps are expected to have fewer carriers generated from the same intensity when pumped directly at the effective band edge. Film absorption strongly increases near the band edge and has only incremental increases with increased energy, leading to an A_{pump}/E_g that peaks near the band edge.

Second, to generate a large index change, the film should ideally have a low initial carrier concentration. This allows a modulation of carrier concentration to generate a larger plasma frequency shift. Similar to the intraband case, a sharp refractive index dispersion at the probe wavelength is also beneficial is it reduces the number of carriers required to achieve a given index modulation. From this dispersion term, an important qualitiy can be discerned – unlike intraband processes, a low loss ENZ film is always ideal for interband pumping. This is because the optical absorption of the probe in the ENZ region (due to free carriers) and interband absorption of the pump (due to band-to-band transitions) are due to two separate processes that are not inherently linked. This dissociation of pump and probe absorption leads to the ideal film being as low loss as possible at ENZ, thus facilitating increased index dispersion in the ENZ region (i.e. at the probe wavelength), while seeking maximized absorption for the pump to enable efficient use of the excitation energy.

Finally, the ideal film has a low effective mass enabling large plasma frequency modulation with a large density of states at the energy of excitation. The large density of states helps overcome the limitation of new carriers having a higher effective mass which would hurt efficiency; a low non-parabolicty also helps mitigate this effect by allowing the effective mass of new carriers to be exactly that of the old carriers, the highest efficiency expected. A direct comparison of materials through this FoM will be conducted in section 5.2.

Similar to the discussion in Section 3.2, a thickness dependence exists where the absorption of the pump is dispersed across a film's thickness. Unlike the case of intraband absorption, interband absorption is highly efficient and therefore has a skin depth as low as 100 nm leading

to the exponential decay of absorption. For this reason, a thickness dependent model was adapted for gradient absorption.

$$\int f(E,\mu,T_e)\rho(E)dE = N_0 + dN(dz) = N_0 + \frac{A_{UV}(dz,\omega)}{dz}\frac{I_{UV}\tau_{UV}}{\hbar\omega} \quad 39$$

$$\int f(E,\mu,T_e)\rho(E)EdE - \int f(E,\mu_0,T_{e0})\rho(E)EdE = \frac{dU_{UV}}{\mathrm{dz}} \quad 40$$

$$\frac{A_{UV}}{dz} = \frac{R(\omega)\left(e^{-\frac{z_1}{\alpha}} - e^{-\frac{z_0}{\alpha}}\right)}{z_1 - z_0} \quad 41$$

Following previous calculations of conservation of carriers and energy, the main difference is now that the energy and carrier density are only calculated for a slab of thickness $dz = z_1 - z_0$. This approach breaks down of a film into many thin layers, each with a deeply sub-skin depth thickness, which can then be treated to have uniform absorption individually. Utilizing a multilayer transfer matrix method described in Section 6.1.2, the transmission and reflection can be calculated for a stack of sub-skin depth films with a thickness dependent index change from gradient absorption.

While the index of the stack will be a gradient based on the absorption at each layer, the overall efficiency of the stack can still be calculated as A_{UV}/d as the overall absorbed energy density is consistent. Since the probe will still be in a film that is significantly sub-skin depth, the reflection of a probe is not only due to the interface but to the entire film stack. This leads to a drop in efficiency that follows the bulk energy density without incurring significant error. Simple transmission calculations, assuming a gradient index compared to a bulk index change find a significant error but continue similar trends. For more accurate results, this effect may be considered through a gradient TMM calculation.

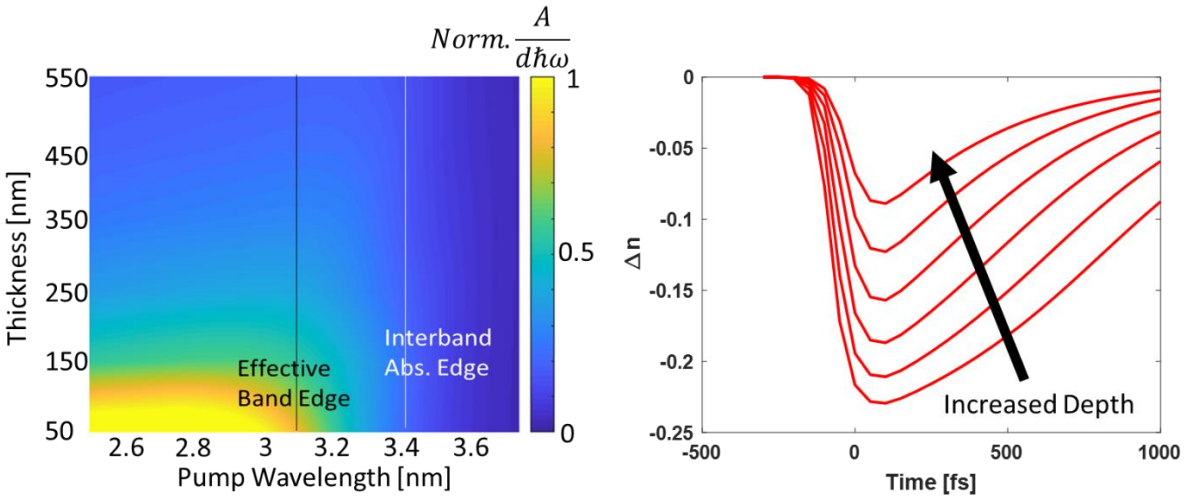

Figure 24 (left) The efficiency of absorption denoted by $A/\hbar\omega d$ calculated as a function of pumping wavelength and film thickness with the spectral film qualities of S4. As the pump energy approaches the band edge it becomes more absorptive while beyond this band edge it begins to fall off. As a function of thickness the film becomes less efficient with a skin depth ~100 nm above the effective band edge leading to a significant drop in efficiency above 200 nm thick films. (right) The refractive index change calculated as a function of thickness for a film with a skin depth of 50 nm and a thickness of 150 nm. Film layers are considered as half of the skin depth showing a significant degradation of efficiency with increased thickness. Transmission calculations were conducted for a bulk absorption density and a gradient absorption density to find an error $\frac{\Delta T_{gradient}-\Delta T_{bulk}}{\Delta T_{gradient}} = 45\%$.

5. HYBRID NONLINEARITIES IN EPSILON-NEAR-ZERO MEDIA

In this section we look to combine the effects of interband and intraband nonlinear excitation of ENZ materials to study more complex interactions and spatio-temporal modulation of the index. Here we will describe how the two separate kinetic models are combined, how they interact, and make use of the predictive power of the model to compare materials across both effects.

5.1. Background: Two Color Excitation of Epsilon-Near-Zero Materials in Literature

Generally, multi pump experiments for IDRI are uncommon in literature, especially for ENZ. However, the control provided through multiple wavelengths, polarizations, angles, etc. provide additional versatility when shaping and engineering the nonlinearity. In particular, one work in literature explored this capability in ENZ materials to achieve bandwidth shaping by using a UV pump and a NIR pump we used to control the index of an AZO film [110]. In this work, two delay stages are used to control the timing of the probe and the NIR pump, while the UV pump has a set arrival time. The effects are considering in this work as non-interacting; the IR pump creates a positive change, the UV pump generates a negative change, the combination of the two is considered as a linear combination. By changing the arrival time between the effects, the interaction of the two pumps can be seen.

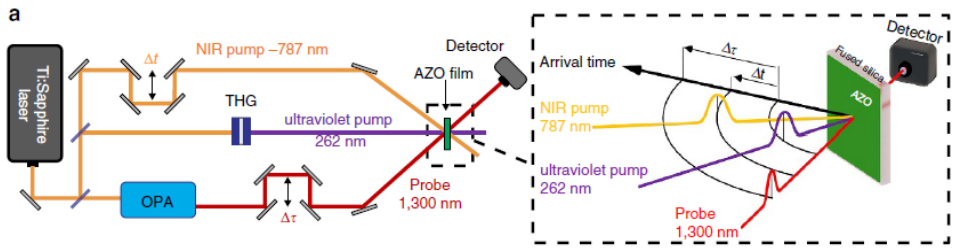

Figure 25 Experimental schematic used in [110] to control both interband and intraband nonlinearities. The 787 nm NIR pump is split and sent through a third harmonic crystal to generate a UV pump. The temporal control of pulse arrival is controlled through two delay stages on the probe and NIR pumps. Figure taken from [5] under Creative Commons License.

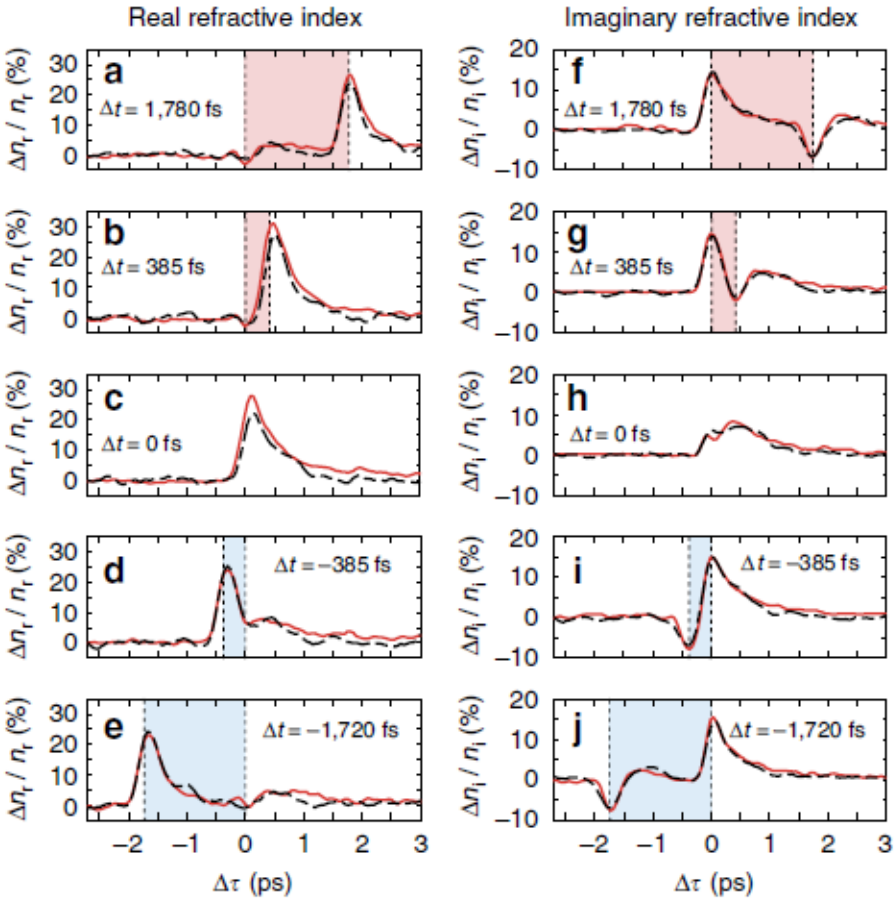

Figure 26 The real (a-e) and imaginary (f-j) percent of refractive index change achieves over a range of Δt and Δτ arrival times for a dual-pump system. The fluences of the ultraviolet and near-infrared pulses are $5\mathrm{mJcm}^{-2}$ and $14\mathrm{mJcm}^{-2}$ respectively. It is seen that when the pulse timings are significantly offset (a,f, and e,j) the nonlinear effects are distinct and separated while their overlap (c,h) results in a singular suppressed effect. Figure taken from Dual Color [5] under Creative Commons License.

This work established the concept of utilizing both the interband and intraband nonlinearities to induce opposite sign nonlinearities; however, an interaction exists where increased carriers from interband absorption induces a change in how intraband absorption occurs, and vice versa. This work generally kept the combination as a linear combination rather than exploring the interaction. Moreover, the paper was unable to accurately predict the amplitude of the nonlinearities, instead restricting its numerical analysis to normalized changes in reflection and transmission. Our theory extends this by providing direct comparison of the magnitude of the nonlinearity while allowing a consideration of the interactions of the two nonlinearities.

5.2. Kinetic Adaptation of Multiple Pump Effects in Epsilon-Near-Zero Media

By exploring every aspect of the individual effects of intraband and interband nonlinearities, we can begin to holistically predict the effects of combinations of multiple pumps. This is the end goal of the work as we can establish more degrees of freedom to optimize the nonlinear response, as well as to utilize the opposing changes in index to shape the index profile both in time and space.

The combination of these effects joins the equations from Section 3.2 and Section 4.2.

$$\int_0^\infty f(E,\mu,T_e)\rho(E)dE = N_0 + \frac{A(\omega_{UV},t)}{\hbar\omega}\frac{P_{UV}}{d} \tag{42}$$

$$A(\omega_{UV},t)\frac{P_{UV}}{d} + A(\omega_{UV},t)\frac{P_{UV}}{d}\frac{\hbar\omega - E_g}{\hbar\omega} + \frac{A(\omega_{IR})P_{IR}}{d} = \int_0^\infty f(E,\mu,T_e)\rho(E)EdE - \int_0^\infty f(E,\mu_0,T_{0e})\rho(E)EdE \tag{43}$$

$$P_{UV} = I_{UV}\tau_{UV} = \int_{-\infty}^{t_{UV}} G_{UV}(t-t_{UV})dt \begin{cases} 1 & t < t_{UV} \\ e^{-\frac{t-t_{UV}}{\tau_{UV}}} & t > t_{UV} \end{cases} \tag{44}$$

$$P_{IR} = I_{IR}\tau_{IR} = \int_{-\infty}^{t_{IR}} G_{IR}(t - t_{IR})dt \begin{cases} 1 & t < t_{UV} \\ e^{-\frac{t-t_{IR}}{\tau_{IR}}} & t > t_{IR} \end{cases} \quad 45$$

From this combination of effects, a few notes can be made. Previous studies have indicated that $\tau_{IR} < \tau_{UV}$ enabling a degree of control over the timing of effects in Equations 44 and 45. Furthermore, in Equation 43, of the potential for the nonlinearities to cross-couple is illustrated. For an interband-first process, the generation of excess electrons above the Fermi level can result in heating of the electron sea. This would alter the effective mass of the electorn sea and result in a modified absorption for intraband nonlinear processes. Under an intraband-first process, the smearing of the free carrier population in energy, produces a more shallow increase in the bandedge absorption versus energy, increasing the absorption for energies just below the Fermi level and decreasing absorption for energies just above. However, this process is not considered here as the absorption of the interband term is considered constant. Future efforts to model the energy-dependent absorption coefficient could include this coupling by determining the interband absorption coefficient directly from the Fermi golden rule [28].

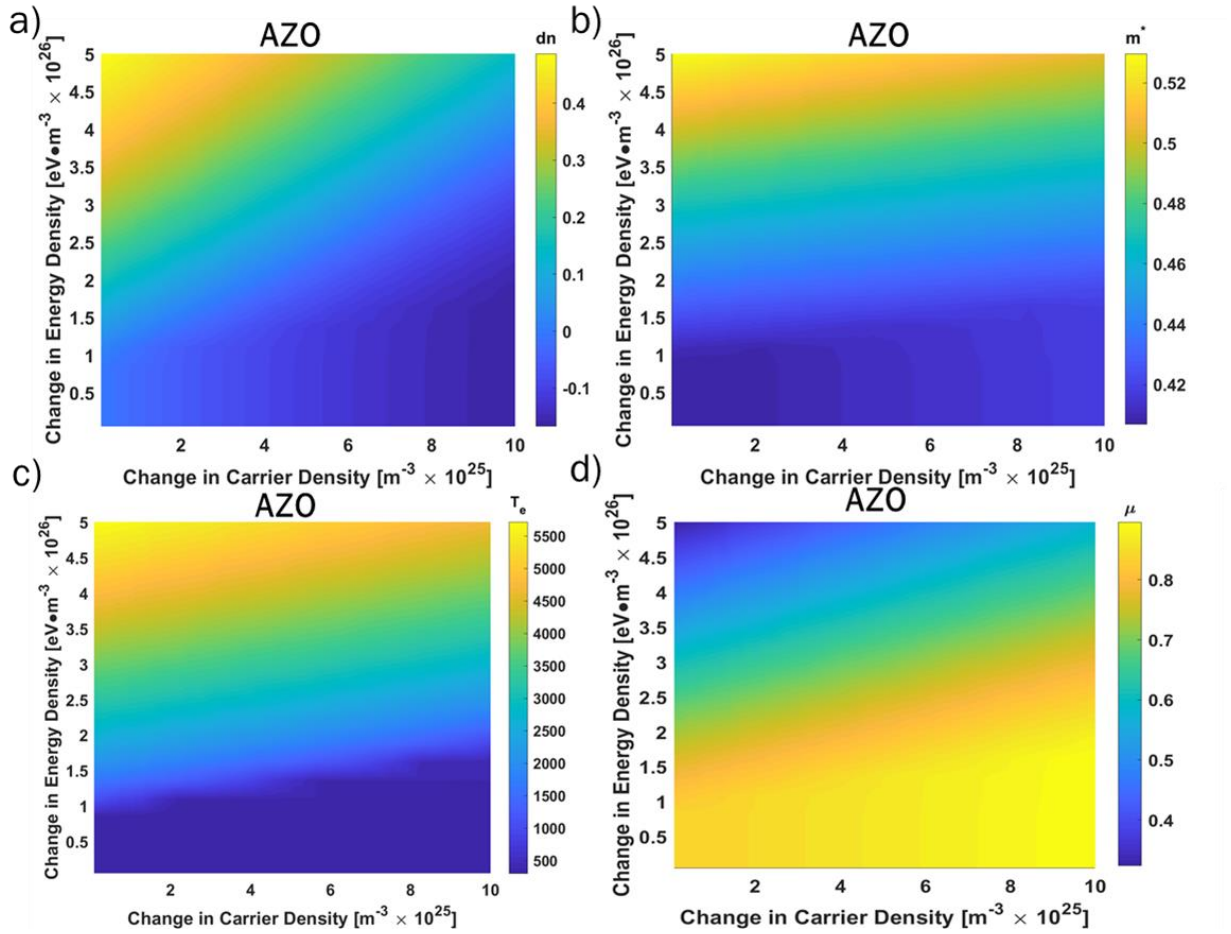

Figure 27 The results of index change (a) due to two pump nonlinear processes calculated for an Al: ZnO film (AZO) with ENZ point of $\lambda_{\mathrm{ENZ}} = 1.5\mu\mathrm{m}$ based on changing energy density and carrier concentration. The factors leading to this effect are the change in carrier density (x-axis) and the average effective mass (b) which increases due to the increased electron temperature (c) in the film. (d) At the same time, the chemical potential, μ, tends to decrease at high temperatures due to carrier continuity. As e-h pairs are generated, the chemical potential rises accordingly.

In Figure 27a, we can see the consequences of the combination of the two nonlinear effects. In particular, a region of "super-linearity" exists where the refractive index does not change from its original value; even though a higher number of carriers exist in the film and the energy density is increased, the two effects counteract. This is an interesting region as it can be accessed through interband followed by intraband pumping, or vice versa, leading to a return to zero. If the return

to zero can be controlled and the timings can be set where the relaxation stays near this zero region, the initial nonlinear process will only be seen for a shorter period of time, acting as a faster signal than its relaxation rate allows.

The interest in the temporal overlap of nonlinearities is twofold: 1) initial reports claim a linear combination of effects [110] whereas we predict variations due to cross-coupling that provide additional freedom in tailoring the nonlinearity, 2) Using one pulse to "quench" the other's effect would offer new abilities for temporal beam shaping. Since the two effects are of opposing sign, adding one nonlinearity the other that is slightly delayed in time will produce a very fast modulation in index (from the peak to the valley), shown in Figure 28b. This is particularly interesting with the new exploration of adiabatic frequency shifting in ENZ nonlinear media [111]. This effect occurs when the material's refractive index changes while the light is propagating in that material, and the magnitude of the shift is proportional to the rate of change of the index. By accelerating the index modulation rates in the medium, the induced adiabatic frequency shift can be enhanced. Since we have improved understanding of optimal pumping regimes for both inter- and intraband responses, comparable ranges (equal and opposite shifts in material such that $\frac{N_0}{m^*_{avg0}} = \frac{N_0+dN}{m^*_{avg}}$) are more able to be controlled, and therefore, the region of linearity may be studied.

Building from these descriptions, single and dual pump experiments can be visualized as traversing the two-dimensional grid of UV and NIR pump excitation through time. Single pumps as presented in Chapters 3 and 4 are described through simple lines while multi-pump experiments traverse through diagonals. If intraband nonlinearities arrive first, the line moves vertically. While overlapped inter-and intraband nonlinearities occur, diagonal movement

occurs, while interband only causes a horizontal movement, angled only by additional energy from pump energies significantly above the absorption edge. As energy is added to the system moves in a positive direction, while relaxation returns in a negative direction. This effect is shown in Figure 28.

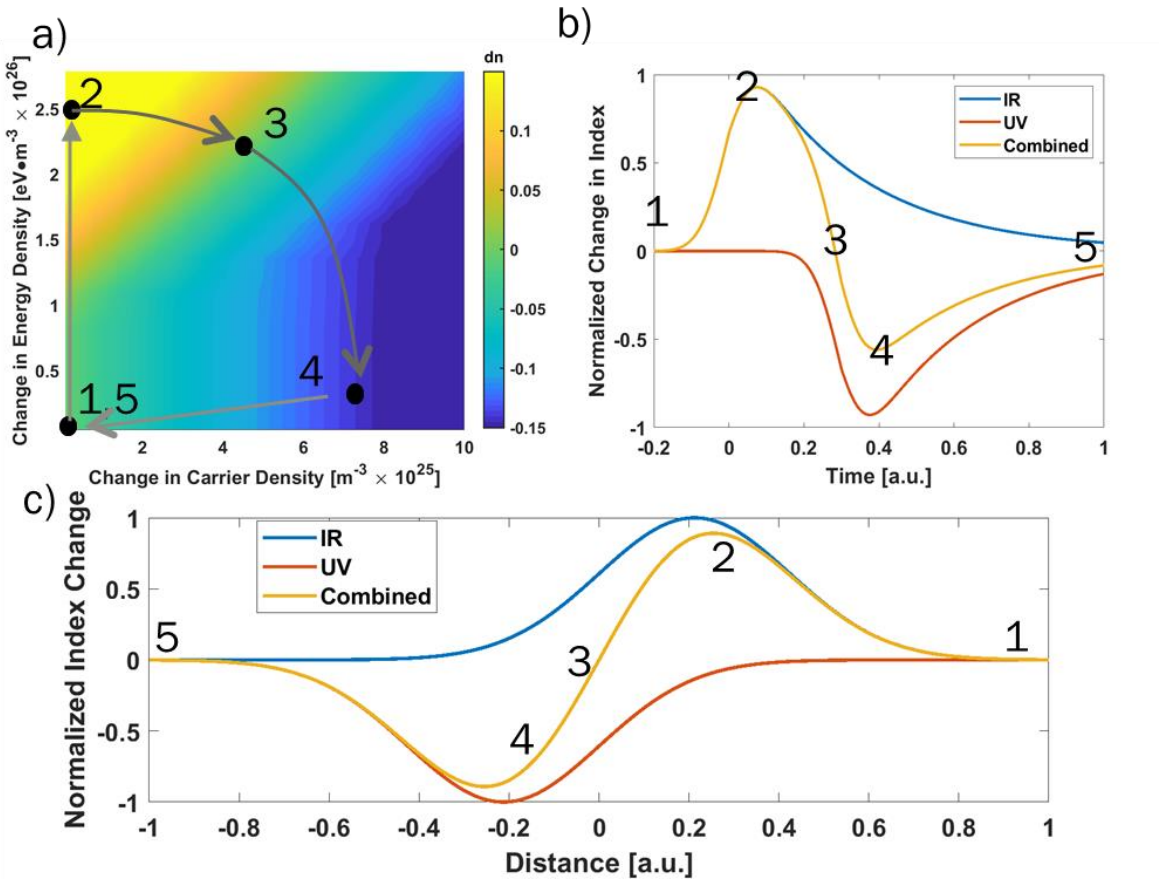

Figure 28: The overlapping of IR (blue) and UV (red) effects in both time (b) and space (c) enable for very high transient properties as seen in orange. This can be depicted as locations in a two-dimensional figure of dn against $\mathrm{dU_{abs}}$ and dN (a). Specific points of interest are labeled 1-5 in each plot with the line in (a) denoting temporal traversing of the spectrum.

5.3. Nonlinear Figure of Merit Comparison for Multi-pump Nonlinearities

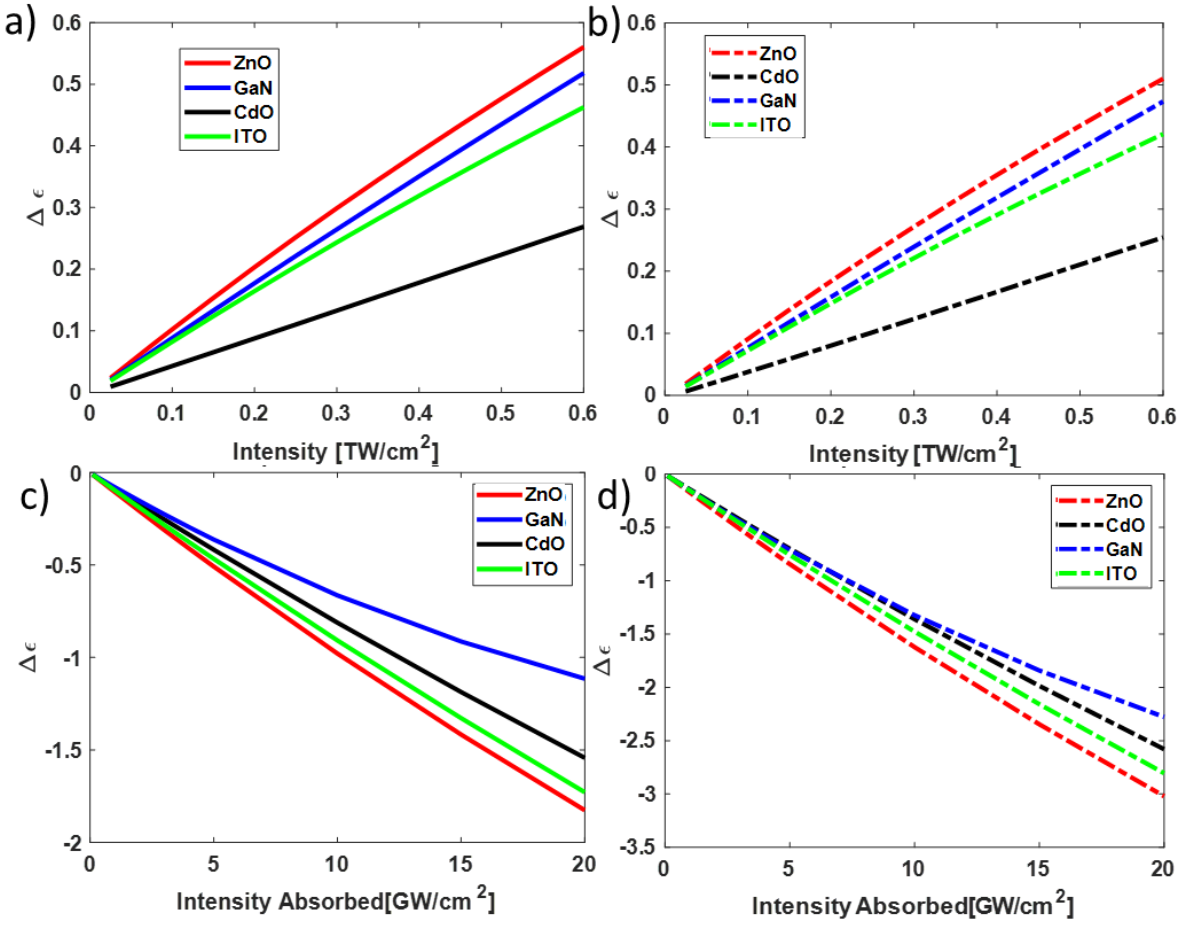

Figure 29 a,b) The change in permittivity calculated from intraband absorption at 787 nm for AZO, GaN, CdO, and ITO with $\lambda(\varepsilon' = 0) = 1.8\mu m$ (solid, a) and $\lambda(\varepsilon' = 0) = 2.2\mu m$ (dashed, b). While ITO and AZO become follow similar magnitudes and curvature, CdO is noticeably worse and GaN is better at high intensities. c,d) The change in permittivity calculated from interband absorption for 0.1eV above the effective band edge of AZO, GaN, CdO, and ITO with $\lambda(\varepsilon' = 0) = 1.8\mu m$ (solid, c) and $\lambda(\varepsilon' = 0) = 2.2\mu m$ (dashed, d). Longer wavelength ENZ films are consistently more efficient due to a lower initial carrier concentration. GaN becomes highly inefficient due to the induced carriers being very heavy compared to other films.

With the established model, we can then extend the framework to additional materials and rapidly evaluate their performance as nonlinear ENZ materials for both inter- and intraband effects *in silico*, requiring only an E-*k* diagram, linear optical properties, and experimental conditions. In particular, the popular ENZ films ZnO heavily doped with Ga or Al (GZO and AZO respectively) and ITO are evaluated alongside heavily doped CdO and GaN for three values of ε'' at the permittivity crossover and several intensities of inter- and intraband pumping, see Figure 29. The linear properties of each material used for the calculations are listed in Table 3 and the HSE hybrid density functional theory parameters of the gap tuned materials are shown in Table 4.

Table 3 Linear properties for AZO/GZO, GaN, CdO, and ITO used to evaluate the nonlinear response.

Material	Crossover Wavelength [μm]	Carrier Concentration [$\times 10^{20} cm^{-3}$]	Effective Mass
AZO/GZO	1.8, 2.0, 2.2	3.94, 3.06. 2.44	0.35, 0.33, 0.32
GaN	1.8, 2.0, 2.2	6.88, 5.07, 3.90	0.38, 0.34, 0.32
CdO	1.8, 2.0, 2.2	7.68, 5.89, 4.63	0.41, 0.38, 0.37
ITO	1.8, 2.0, 2.2	4.44, 3.46, 2.77	0.39, 0.38, 0.37

Table 4 HSE calculated lattice constants and bandgaps obtained by tuning the fraction of exact exchange α and the range separation parameter μ. The crystal structure of ZnO and GaN is wurtzite, that of CdO is rock-salt structure, and that of In_2O_3 is the bixbyite structure (space group 206, $Ia\bar{3}$), which is a body-centered cubic structure with 8 formula units per primitive unit cell. Courtesy of Dr. Denis Demchenko.

Material	α	μ [1/Å]	E_g [eV]	a [Å]
ZnO	0.3	0.0517	3.41	3.26
CdO	0.25	0.383	2.14	4.73
GaN	0.25	0.114	3.42	3.19
In_2O_3	0.25	0.147	2.68	5.11

While full theoretical calculations can be conducted as in Figure 29, these can be laborious and lack intuition to push new boundaries with new materials; to explore a set of materials for both nonlinearities efficiently, a FoM can be established for both effects. From Section 3.2, an intraband FoM is developed:

$$FoM_{intra} = A_{pump}\left[\frac{1}{m^*}\frac{dm^*(\mu_F)}{dE}\right]\left[\frac{1}{N}\frac{dn}{dm^*}\right]. \quad 9$$

The nonlinearity is dominated by a change in the effective mass quantified by the non-parabolicity of dm^*/dE. The index curvature at the probe (typically near ENZ) indicates the sensitivity of the index to the modification of the effective mass, quantified as dn/dm^*. A large number of carriers or high initial effective mass reduces the overall efficiency per unit energy. Similarly, from Section 4.2 the interband FoM can be introduced considering the change of free carriers:

$$FoM_{inter} = \left[\frac{A_{pump}}{E_g}\right]\left[\frac{1}{N}\frac{dN(\mu_F)}{dE}\right]\left[\frac{1}{m^*}\frac{-dn}{dN}\right]. \quad 10$$

Here, the dn/dN describes the sensitivity of the index to a change in carrier density (equivalent to a group velocity term) while dN/dE describes the number of available states near the Fermi energy. Many initial carriers or a high effective mass tend to decrease the efficiency per unit energy. Finally, the absorption is normalized by the bandgap energy because the modulation of carrier density is governed by $\Delta N \propto \frac{A}{\hbar\omega}$ with $\hbar\omega > E_g$. In essence, wide-bandgap materials require more energy to generate the same number of excess carriers.

From the FoM calculations, several important comparisons are made to predict the preferred film for various applications. GaN is found to be efficient for intraband operation due to its large non-parabolicity. At moderate energies, where other band structures are approximately hyperbolic, GaN forms a peak near the L-valley shown in Figure 30a-c. This pushes the non-parabolicity to extreme levels as effective mass and DOS become quite large in this region, giving rise to a large modulation as seen in Figure 29a,b. However, realizing ENZ GaN in the telecom range (1.3–1.5 µm) is expected to be challenging as incremental blue-shifts in plasma frequency via increased doping come with significant increases in effective mass. On the other hand, CdO is found to be more efficient for interband. This because CdO exhibits weak non-parabolicity and for low to moderately doped CdO, each excess electron thus induces a nearly equal change in plasma frequency due to a slow variation of effective mass. Additionally, CdO has been shown to be ultra-low loss in the plasma frequency range of 2-5 µm which leads to a sharp index dispersion in the ENZ region [32,50–52]. However, the high background permittivity requires a large number of carriers to achieve ENZ, which reduces the energy efficiency.

For all-around materials, ITO and doped ZnO are well suited for both interband and intraband nonlinear processes. A provide a moderate non-parabolicity and small background permittivity combine to induce efficient nonlinear effects in both interband and intraband operation. For interband operation, the low initial carrier concentration allows new carriers to contribute to a large percentage of the overall concentration without significantly increasing the average effective mass. For intraband operation, the initial effective mass is moderately low with a non-parabolicity factor that allows for a large effective mass modulation. Additionally GaN and CdO, ITO and doped ZnO (AZO/GZO) have been shown to achieve ENZ ranges as low as 1.2 μm [12,24,25,42,53].

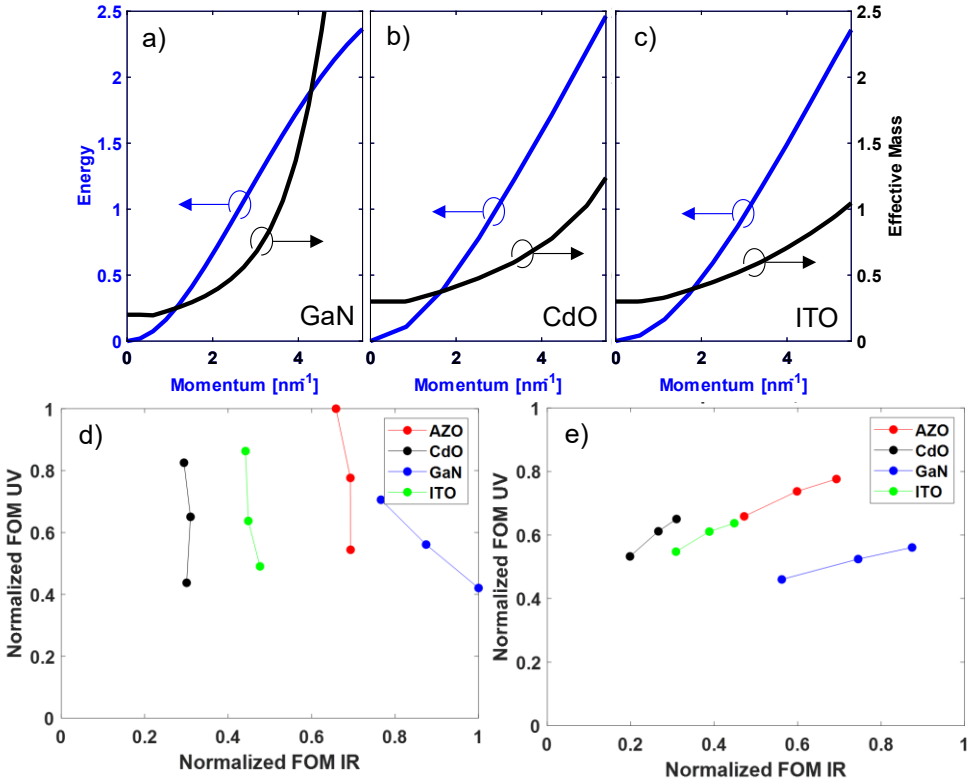

Figure 30 a-c) Energy-Momentum and Effective Mass-Momentum diagrams for GaN ($\Gamma \rightarrow A$), CdO ($\Gamma \rightarrow X$), and ITO ($\Gamma \rightarrow P$) respectively calculated through using HSE. The effective mass is in the units of m^*/m_0. d,e) Normalized Figure of Merit calculations for doped ZnO (AZO/GZO), GaN, CdO, and ITO. Figure d) fixes film loss ($\varepsilon"(\lambda\_ENZ) = 0.7$) while varying ENZ wavelength (1.8, 2.0, 2.2μm bottom to top), while e) fixes the ENZ point to 2.0μm and varying loss $\varepsilon" = 0.3,0.5,0.7$ (left to right)

Additionally, the FoMs illustrate the trade-offs in maximizing nonlinearities of ENZ materials, specifically the link between the absorptivity of the film for the pump and the need for a steep index dispersion at the probe. In the intraband case, this competition produces an optimum for most films in the range of ε" ~ 0.3 – 0.6 [16]. The interband nonlinearity, however, allows more freedom as the absorption of free carriers is not connected to the index slope near ENZ. As a result, one will always benefit from a lower loss at ENZ and higher losses at the pumping frequency with the limit arising due to impedance matching when the refractive index at ENZ approaches zero. A last note that while interband is more efficient, it is generally slower than the

intraband process, leading to a strength-bandwidth trade-off that should be considered for each application. Yet, both processes in TCOs have been shown to achieve THZ scale effects (see Figure 29 a,b).

6. INTRABAND AND INTERBAND EPSILON-NEAR-ZERO NONLINEAR MEASUREMENTS

Sections 3 through 5 contain a significant number of effects and trends which have not been readily studied in literature to date. To remedy this, in-house and collaborative experimental studies have been conducted in both beam deflection and reflection-transmission based methods. Thorough investigation into two AZO films and six GZO films were conducted to study the proposed trends. By validating the theoretical trends, the ideal pump, probe, and films may be determined to provide direction toward the most productive configurations. Experiments to directly explore these trends are studied.

6.1. Background: Experimental Methods for Investigation of Optical Nonlinearities

6.1.1. Beam Deflection Method for Measurement of Intensity Dependent Refractive Index

To measure the Intensity Dependent Refractive Index of materials, techniques interrogate induced refraction through a strong pump laser or a pump and a probe. Since the pump has a spatially varying intensity, a spatially varying refractive index is formed. The pump itself or an independent probe interrogates the spatially varying refractive index that can be interpreted from measurement.

A common method for this interrogation is Z-Scan [104,112–114]. Z-Scan is generally a single beam measurement utilizing the focusing or defocusing of the pump to determine the optical changes. In Z-Scan measurements, the sample is moved across the focus of a beam. As the film approaches the focus, the intensity of the laser increases due to the area decreasing, thus probing

the intensity dependent film properties. In an open aperture measurement, this modifies the transmission due to reflection or absorption changes. Since the laser has a Gaussian spatial distribution, the resulting index distribution follows that of a lens formed by the nonlinear IDRI coefficient. The concavity of the induced lens depends on the sign of n_2. A second measurement, called closed aperture, where the transmission of the beam through a fixed aperture is measured, is often used in conjunction to measure the lensing effect. With proper interpretation of one or both measurements, the nonlinear refraction and absorption of a material is captured.

A method that has been more recently developed is that of beam deflection [113–116]. Beam deflection requires a separate pump and probe that enable both non-degenerate, and time dependent measurements. This is a highly beneficial property for nonlinearities with broad frequency bandwidths and non-instantaneous changes, such as those in ENZ films. Beam deflection operates under the principle that the pump will create an effective prism inside the material that modifies the propagation of by a probe. An example experimental set up is shown in Figure 31.

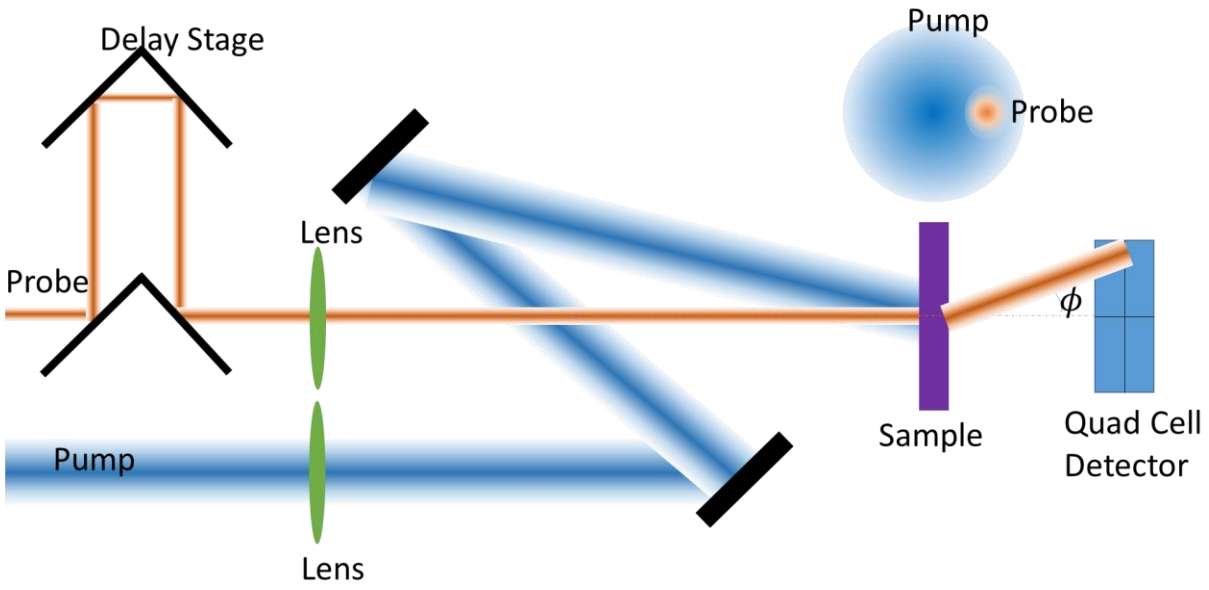

Figure 31: Schematic diagram of a beam deflection measurement. A large pump is used to alter a sample with a probe detecting that change through deflection caused by an effective prism generation. The probe timing can be altered through the use of a delay stage to measure time dependent refraction. The deflection and transmission amounts are measured by a quad cell detector.

The derivation of the effect can follow a few methods [113,114,116]. Under the thin prism treatment, the pump (e) and probe (p) are defined through spatial and temporal Gaussian distributions.

$$I_e(x,y,t) = I_{0,e}\exp\left(-\frac{2(x^2+y^2)}{w_e^2}-\frac{t^2}{\tau_e^2}\right) \quad 48$$

$$I_p(x,y,z,t,\tau_d) = I_{0,p}\exp\left(-\frac{2(x^2+y^2)}{w_p^2(z)}-\frac{(t-\tau_d)^2}{\tau_p^2}\right) \quad 49$$

In the case of a thin film or low GVM film, the location of the probe will not vary compared to the location of the pump in space or time. The sizes of the beam are defined by the $HW1/e^2$ spot sizes w_e and w_p as well as the $HW1/e$ temporal sizes τ_e, τ_p with a temporal separation τ_d. The thin prism approximation operates under the belief that the phase front bends due to a change

in phase accumulation over the thickness of the sample from one end of the probe to the other, i.e. $\frac{(n+n_2 I(x_1))-(n+n_2 I(x_2))}{x_1-x_2} L$, the deflection angle is calculated:

$$\theta = \int_0^L \nabla n_p(x,y,t) ds \approx \nabla n_p(x,y,t) L. \quad 50$$

This is synonymous with the derivation of angular deflection through Generalized Snell's Law [117] under the approximation that the probe is oriented on a major axis of the pump.

$$n_i \sin\theta_i - n_t \sin\theta_t = \frac{\lambda_0}{2\pi}\frac{d\phi}{dx} \quad 51$$

Under normal incidence, transmitted into air, this becomes:

$$\sin\theta_t = \left(\frac{\lambda_0}{2\pi}\frac{d\phi}{dx}\right) \quad 52$$

Since the phase accumulation in a film is calculated as $n\frac{L}{\lambda_0}$, $d\phi$ can be calculated as $\frac{L}{\lambda_0} dn$. Under the small angle approximation, $\sin\theta = \theta$, Equation 52 converges to Equation 50. At a distance D away from the sample, this induces a deflection $\Delta x = D\theta$.

The detector used to measure beam deflection is a quad cell, a single detector partitioned into four sections. Three values are output from the quad cell, E, ΔE_x, and ΔE_y.

$$E = Q_1 + Q_2 + Q_3 + Q_4 \quad 53$$

$$\Delta E_x = (Q_2 + Q_3) - (Q_1 + Q_4) \quad 54$$

$$\Delta E_y = (Q_2 + Q_1) - (Q_3 + Q_4) \tag{55}$$

After the beam has been deflected, it arrives at the detector with a Gaussian shape of:

$$I_d(x, y, t, \tau) = I_{0,d} \exp\left(-\frac{2((x - \Delta x)^2 + y^2)}{w_d^2} - \frac{(t - \tau_d)^2}{\tau_p^2}\right). \tag{56}$$

$$\frac{\Delta E_x(t)}{E(t)} = \frac{\left(\int_{-\infty}^{0}\int_{-\infty}^{\infty} I_d(x, y, t, \tau)\, dy\, dx - \int_{0}^{\infty}\int_{-\infty}^{\infty} I_d(x, y, t, \tau)\, dy\, dx\right)}{\int_{-\infty}^{\infty}\int_{-\infty}^{\infty} I_d(x, y, t, \tau)\, dy\, dx} \tag{57}$$

From the measurement of $\Delta E_x(t)/E(t)$, the deflection, and thus, ∇n_p can be calculated. To make the calculation of ∇n_p simpler, the probe is situated at $w_e/2$ allowing for a triangular approximation of the Gaussian distribution, $\nabla n_p = \frac{n_2 I}{w_e}$. This allows the solution of $\Delta E/E$ to be found numerically as:

$$\Delta x = \frac{2}{\sqrt{e}} \frac{1}{w_e} \frac{1}{\lambda} d \tag{58}$$

$$\frac{\Delta E}{E} = \frac{2\sqrt{2}}{\sqrt{e}} \frac{w_p}{w_e} \frac{L}{\lambda} \Delta n \tag{59}$$

In the presence of nonlinear absorption, the process has an additional degree of complexity as the transmission is modulated as well as the phase. Under thin prism approximations, this can be treated as a separate effect which will both change E itself, as well as provide a non-uniform transmission across the probe which shows as additional ΔE_x.

As a result, the intensity at the detector with absorption considered is now calculated:

$$I_d(x, y, t, \tau) = I_{0,d} T_0(x, y, t, \tau) \exp\left(-\frac{2((x - \Delta x)^2 + y^2)}{w_d^2} - \frac{(t - \tau_d)^2}{\tau_p^2}\right) \tag{60}$$

where $T_0 = 1$ denotes the linear transmission of the film, $T_0 > 1$ is an increased transmission due to the nonlinearity, and $T_0 < 1$ is a reduction in transmission due to the nonlinearity. In the case that n_2 and $\alpha_2$have opposite signs, the two effects have an additive property; a positive n_2

deflects the beam toward the center of the pump, while a negative α_2 will result in the portion of the probe closest to the center also having the largest transmission with the outer portion having less transmission increase. This can lead to large $\Delta E/E$ measurements, even for small index changes. To model both effects simultaneously, the total signal modulation can be measured as $\Delta T_0(t) = \Delta T(t)/T$. This process is necessary since two values are now being extracted, n and α, requiring two measurements, ΔE_x and ΔE.

6.1.2. Time Dependent Nonlinear Reflection-Transmission Method for Epsilon-Near-Zero Materials

Another method available for discerning the nonlinear properties of films is to simultaneously measure the changes in reflection and transmission due to an optical pump. As the reflection and transmission are directly related to the complex refractive index, the measurement of these properties can help lead to understanding the change in a film. While individual measurements of reflection and transmission are useful, simultaneous measurement paired with a numerical model are required to decipher the change in refractive index.

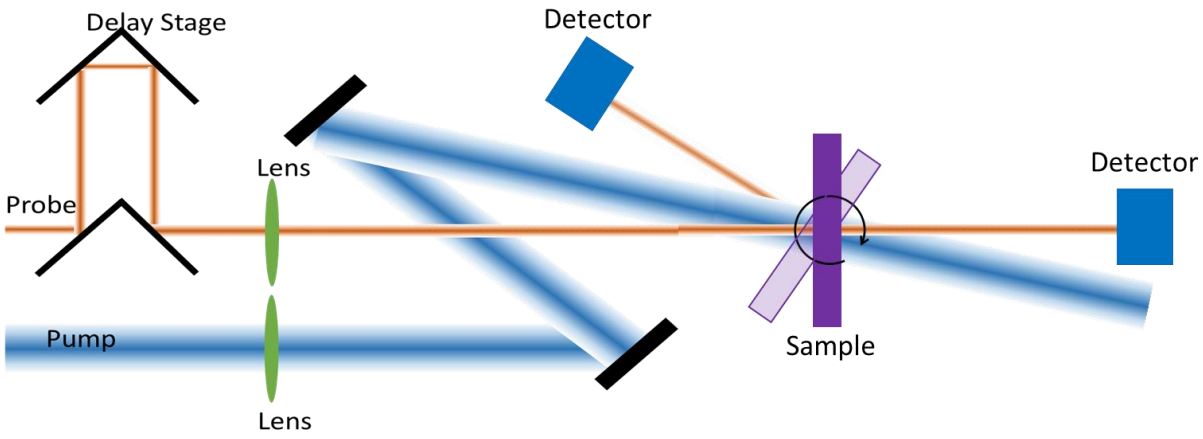

Figure 32 Schematic diagram of a nonlinear reflection-transmission measurement. A large pump is used to alter a sample with a probe detecting that change through a change in reflection and absorption. The probe timing can be altered through the use of a delay stage to measure time dependent changes. The intensities of the reflection and transmission are measured through a detector. The sample is mounted on a rotational stage to enable reflection measurements.

Under the approximation of no substrate effect and normal incidence, the reflection and transmission of unpolarized light can be calculated using the Fresnel equations [118] and Beer's Law as:

$$R(\lambda) = \left(\frac{\tilde{n}(\lambda) - 1}{\tilde{n}(\lambda) + 1}\right)\left(\frac{\tilde{n}(\lambda) - 1}{\tilde{n}(\lambda) + 1}\right)^{*} \quad 61$$

$$A(\lambda) = (1 - R(\lambda))\left(e^{\alpha(\lambda)t} - 1\right) \quad 62$$

$$T(\lambda) = 1 - R(\lambda) - A(\lambda). \quad 63$$

When a substrate or angle is added, more complexity is required to directly solve R and T directly. For this additional complexity, the Transfer Matrix Method can be applied to solve for R,T, and A in a multilayered medium [119]. This method can be used to solve for the propagation coefficients of a plane monochromatic wave for a film on substrate, as well as for more complex

structures such as a graded medium. From characteristic equations of electric and magnetic fields inside a non-magnetic medium, the M matrix can be calculated as:

$$M_{TE}(z) = \begin{bmatrix} \cos(k_0\, n\, z \cos\theta) & -\frac{i}{nk_0 \cos\theta}\sin(k_0 n\, z \cos\theta) \\ -i\, nk_0 \cos\theta \sin(k_0\, n\, z \cos\theta) & \cos(k_0\, n\, z \cos\theta) \end{bmatrix} \quad 64$$

$$M_{TM}(z) = \begin{bmatrix} \cos(k_0 nz \cos\theta) & -\frac{in}{k_0 \cos\theta}\sin(k_0 nz \cos\theta) \\ -\frac{i\, k_0 \cos\theta}{n}\sin(k_0 nz \cos\theta) & \cos(k_0 nz \cos\theta) \end{bmatrix} \quad 65$$

For a succession of film layers, the final $M(z_N)$ matrix is calculated as in multiplication of all previous M matrices:

$$M(z_N) = \prod_{j=2}^{j=N} M\left(z_j - z_{j-1}\right) \quad 66$$

From this total M matrix for the structure, from here called m', the field reflection and transmission coefficients can be calculated [120] with a substrate of index n_2 and film index n_1:

$$r_{TE} = \frac{(m'_{21} + m'_{12}\, n_2 k_0^2 \cos\theta) - i(k_0 m'_{11} + m'_{22}\, k_0 n_2 \cos\theta)}{(-m'_{21} + m'_{12} n_2\, k_0^2 \cos\theta) + i(k_0 m'_{11} + m'_{22} k_0\, n_2 \cos\theta)} \quad 67$$

$$t_{TE} = \frac{2in_1 k_0 e^{-k_0 n_2 t}(m'_{11}m'_{22} - m'_{12}m'_{21})}{(-m'_{21} + m'_{12}\, k_0^2 n_2 \cos\theta) + i(m'_{11} + m'_{22} k_0^2\, n_2 \cos\theta)} \quad 68$$

$$r_{TM} = \frac{(m'_{21} + m'_{12}\, k_0^2 \cos\theta\, /n_2) - i(k_0 m'_{11} + m'_{22}\, k_0 \cos\theta\, /n_2)}{(-m'_{21} + m'_{12}\, k_0^2 \cos\theta\, /n_2) + i(k_0 m'_{11} + m'_{22} k_0\ \cos\theta\, /n_2)} \quad 69$$

$$t_{TM} = \frac{2in_1 k_0 e^{-k_0 t/n_2}(m'_{11}m'_{22} - m'_{12}m'_{21})}{(-m'_{21} + m'_{12}\, k_0^2 \cos\theta\, /n_2) + i(m'_{11} + m'_{22} k_0^2\ \cos\theta\, /n_2)} \quad 70$$

$$R = |r|^2, T = n_2|t|^2 \quad 71$$

To convert between TE and TM operation, the refractive indexes are replaced with the inverse, as shown in Equation 64 and Equation 65. Through this methodology, the accuracy of transmission and reflection calculations are increased. From this approach the reflection and

transmission of a numerical model can be predicted and matched to measured results, hence extracting the complex refractive index in time.

6.2. Intraband Experiments in Epsilon-Near-Zero films

6.2.1. Experimental Measurement of Beam Deflection from Intraband Intensity Dependent Refractive Index in Epsilon-Near-Zero films

To experimentally demonstrate the nonlinear interaction of AZO in intraband excitation, degenerate and non-degenerate beam deflection measurements were conducted. The pump and probe pulses are generated by a 7W, 90 fs, 800 nm Solstice Ace system [Spectra Physics] which are routed into two Ti:Sapphire optical parametric amplifier (TOPAS) systems. The pump pulse was directed into a NIrUVis system to generate pulses from 1200 nm to 1600 nm in wavelength. The probe was directed into a TOPAS system also capable of generation from 1200 nm to 1600 nm. The pump polarization was rotated to vertical while the probe was horizontal to avoid minimize two beam coupling effects. The probe pulse was filtered to ~1mW average power and the pump pulse was filtered to variable powers from 10mW to 100mW average power. The probe line was fitted with a delay line capable of >1ns of delay. The probe was focused to a FW$1/e^2$ waist of $\sim 300\mu m$ while the pump was focused to a FW$1/e^2$ waist of $\sim 1100\mu m$ to $\sim 1500\mu m$ with a beam size ratio $3.2 < \frac{w_e}{w_p} < 5$. The probe was situated $\sim 300\mu m$ below the center of the pump, in accordance with the theoretical ideal placement of $HW1/e^2/2$ [114]. The pump arrived at the sample with an incidence angle of $\sim 10°$ to the sample, parallel to the table. The PDQ30C Quad-Cell Detector (Thorlabs) was located 12cm behind the sample where the probe $FW1/e^2$ waist is $\sim 800\mu m$. Location and size of beams were confirmed through knife-edge

measurements. For all measurements, the films were measured substrate first and the substrate response was measured and removed.

Two samples were studied, S120 with AZO thickness of 120 nm and S240 with AZO thickness of 240 nm, grown on c-sapphire. The AZO films were grown through plasma-enhanced atomic layer deposition (PE:ALD). The two sample characteristics are outlined in Table 5. Films were characterized through spectroscopic ellipsometry paired with transmission measurements as detailed in Section 2 and modelled through Equation 30-32. The resulting permittivity of the samples is shown in Figure 33. Experiments were fit using the theoretical framework described in Section 3-5 with with the band structure calculated through DFT.

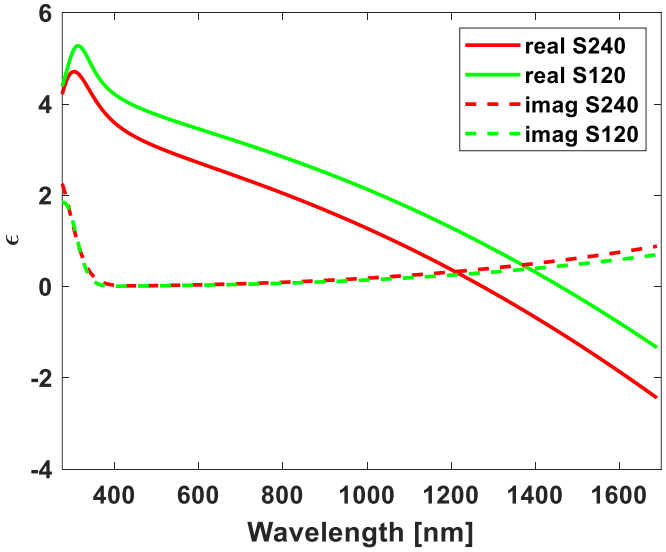

Figure 33 Real (solid) and imaginary (dashed) permittivity of S240 (red) and S120 (green) fit through ellipsometry measurements.

Table 5 Sample characteristics for samples used in nonlinear beam deflection measurements

Sample	Film ENZ [μm]	ε" at ENZ	Carrier Density [$\times\ 10^{26} cm^{-3}$]	Effective Mass [$\times\ m_0$kg]	Thickness [nm]
S120	1.43	0.7	7.958	0.423	120
S240	1.27	0.4	9.413	0.439	240

Initial nonlinear characterization of the films included non-degenerate intensity dependent measurements shown in Figure 34 for sample S120 and Figure 35 for sample S240. For this measurement, the probe was at 1600 nm while the pump was at 1200 nm. For all measurements to follow, temporal dynamics demonstrate a complete relaxation within 1ps for a relaxation rate consistent with other measurements of AZO grown through sputtering, $\tau \sim 200 fs$.

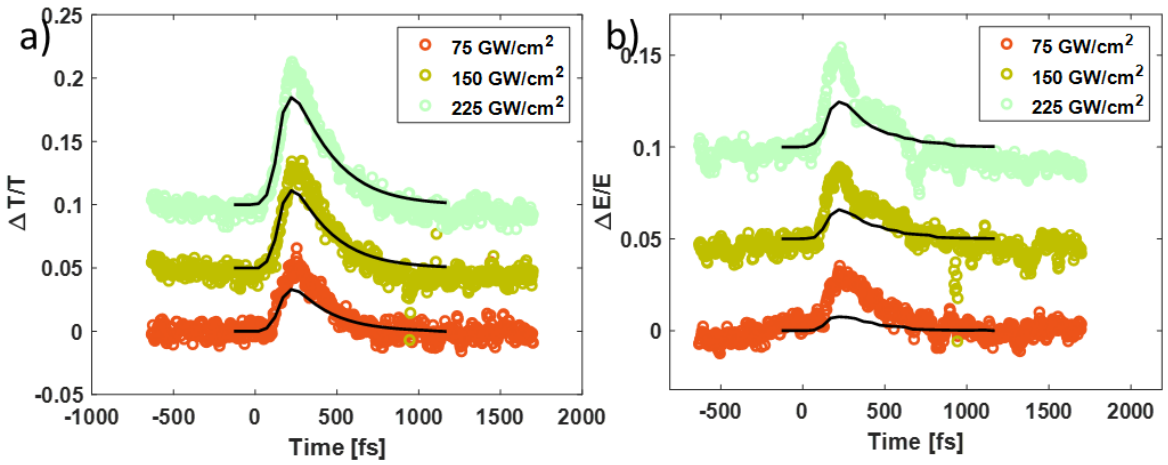

Figure 34: Experimentally measured $\Delta T/T$ (a) and $\Delta E/E$ (b) for S120 at three powers, 75 (red), 150 (olive), and 225 (green) GW/cm^2. As intensity increases, $\Delta T/T$ and $\Delta E/E$ increase. Theoretically calculated $\Delta T/T$ (a) and $\Delta E/E$ (b) are shown in black. An artificial separation of 0.05 is applied for clarity. As intensity increases, $\Delta T/T$ and $\Delta E/E$ increase with a strong agreement in $\Delta T/T$ and a proper ordering for $\Delta E/E$.

For this combination, the experimental and projected values for transmission modulation follow very closely to each other showing a high degree of accuracy to the modelling. The $\Delta E/E$ measurement has a slightly higher modulation than predicted which tends to be a trend of our calculation. Nearly all of the $\Delta E/E$ signal in the film at this combination is projected to be through the transmission modulation with little to no actual deflection predicted due to the nearly flat dispersion of index in this region. In S120, the film is very thin, leading to high initial transmission, even in the metallic region after $1.43\mu m$. This leads to 1600 nm being the optimal transmission modulation probe wavelength as will be discussed further in the spectrally dependent measurements to follow.

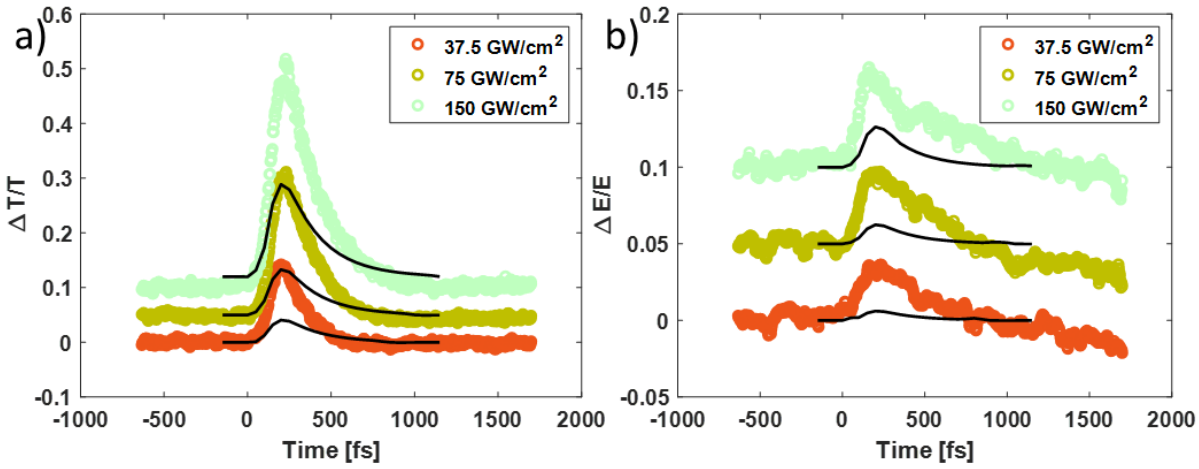

Figure 35 a) Experimentally measured $\Delta T/T$ and $\Delta E/E$ for S240 at three powers, 37.5 (red), 75 (olive), and 150 (green) GW/cm^2. Data is artificially separated by 0.05 for each power. As intensity increases, $\Delta T/T$ and $\Delta E/E$ increase. Theoretically calculated $\Delta T/T$ and $\Delta E/E$ for a modelled S240 are shown in as black lines for each dataset. As intensity increases, $\Delta T/T$ and $\Delta E/E$ increase with a reasonable agreement and ordering.

Compared to S120, S240 shows a very large nonlinear transmission change, but only a marginally higher $\Delta E/E$. The projected values for transmission modulation are within a factor of 2 of the experimentally measured values. The $\Delta E/E$ measurement has significant noise due to the low initial signal but follows the general trends expected through theory. Due to S240 having a shorter crossover wavelength (1270), the probe is in a metallic, slightly negative, dispersion region of the index. Due to this dispersion, no significant beam deflection from index modulation is expect, though the effect of large transmission modulation is evident. Compared to S120, S240 is thick, nearly twice the thickness, and even more metallic. This leads to initial transmission at 1600 nm of only 20%, and enables a significantly larger transmission modulation than is possible in S120, which was measured to be as high as 40% (raw T of 28%). A further examination of results would lead to a conclusion that film S240 also has a more efficient absorption of the pump,

leading to larger modulation. This relative comparison deserves more acute focus and will be discussed further to follow.

To understand the spectral response of our films, the probe and pump must be independently studied. Our theory predicts the largest nonlinear response in pump regimes with the largest absorption and probe regions near ENZ. Figure 17 shows that this region of ideal pump wavelength changes with respect to thickness, with pinning to ENZ occurring at thickness 250 nm and above, with a trend toward long wavelengths for thinner films. To study this effect, films S120 and S240 are utilized as a thin film and a near pinning film. Pump and probe wavelengths of 1200 nm, 1400 nm and 1600 nm are utilized for spectral dependence in all combinations. Knife edge measurements were used to position and size our beams. Pump beams at 1200 and 1600 nm were approximately FW$1/e^2$ waist of $\sim 1100 \mu m$ while the pump at 1400 nm was slightly larger at $\sim 1500 \mu m$. This leads to a small non-ideality in beam deflection where $\Delta E/E$ is slightly smaller at 1400 nm due to a larger w_e (see Equation 60). The pump intensity is kept similar for all experiments between 120 and 150 GW/cm^2 with small variations due to filtering and pump size.

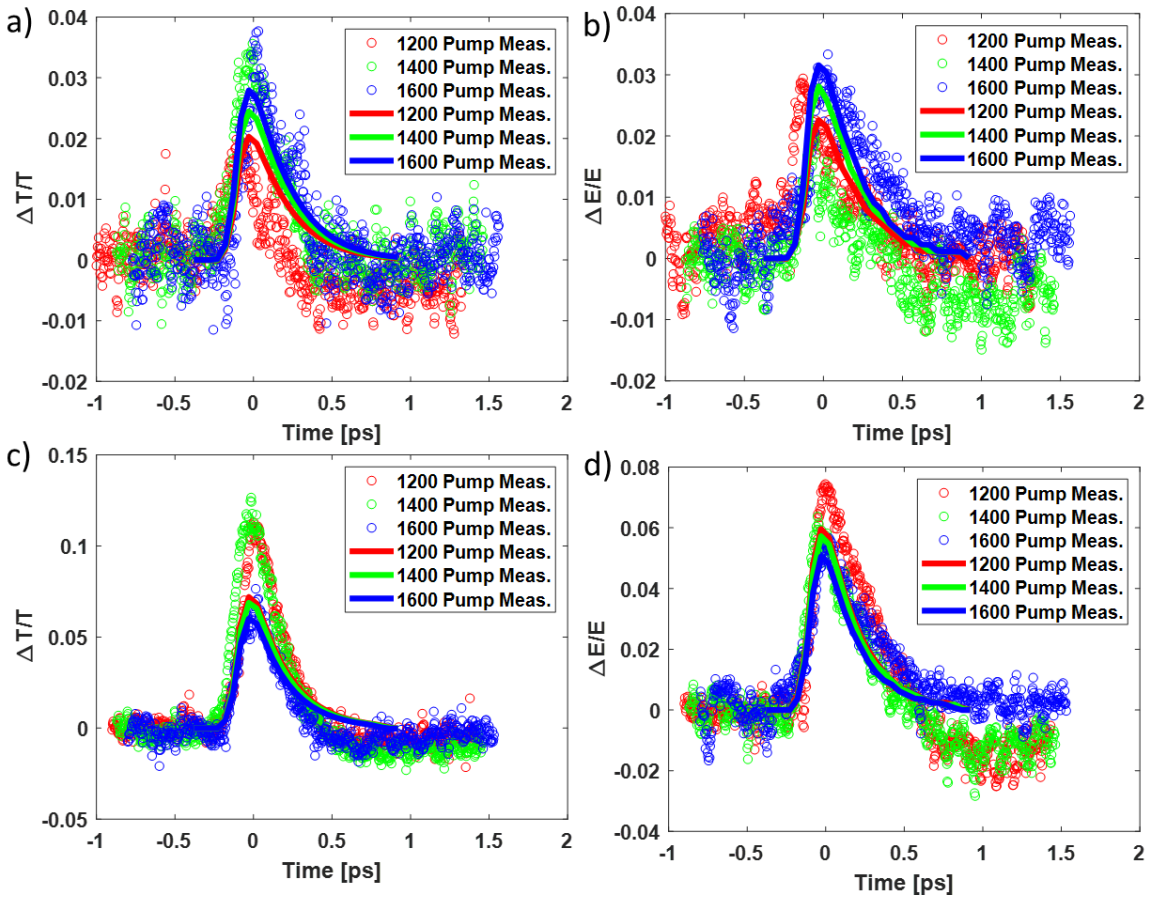

Figure 36 Nonlinear beam deflection measurements at probe wavelength of 1200 nm in $\Delta T/T$ (a,c) and $\Delta E/E$ (b,d) for films S120 (a,b) and S240 (c,d) for three pump wavelengths, 1200 nm (red), 1400 nm (green), and 1600 nm (blue) and an intensity $\sim 125 GW/cm^2$. For film S120, the absorption spectra prefers long wavelength pump operation due to a thickness of only 120 nm, making the 1600 nm pump to induce larger changes than the 1400 and 1200 nm pumps. For film S240, the absorption spectra is pinned to ENZ due to the film thickness of 240 nm. This makes 1200 and 1400 nm significantly more efficient that 1600 nm as the ENZ point of film S240 is approximately in the middle of these two wavelengths.

From experiments probed at 1200 nm and pumped from 1200 to 1600 nm (Figure 36), the trend clearly follows the absorption spectra of the respective films. Film S120 performs most optimally when pumped at 1600 nm falling off to a weakest interaction with 1200 nm due to being a thin film. On the other hand, film S240 equally favors 1200 and 1400 nm pumps as the ENZ wavelength

is ~1300 nm and the film is thick enough to cause the pinning of absorption to ENZ. S240 has the weakest interaction with 1600 nm pumping. Transmission modulation is expected to be largest in all cases for S240 as the initial transmission for S240 is significantly smaller. In the case of probing at 1200 nm, S240 is also expected to have a significantly larger deflection as the probe is nearly at ENZ; whereas, film S120 is probed further blue respectively, causing only minor deflection.

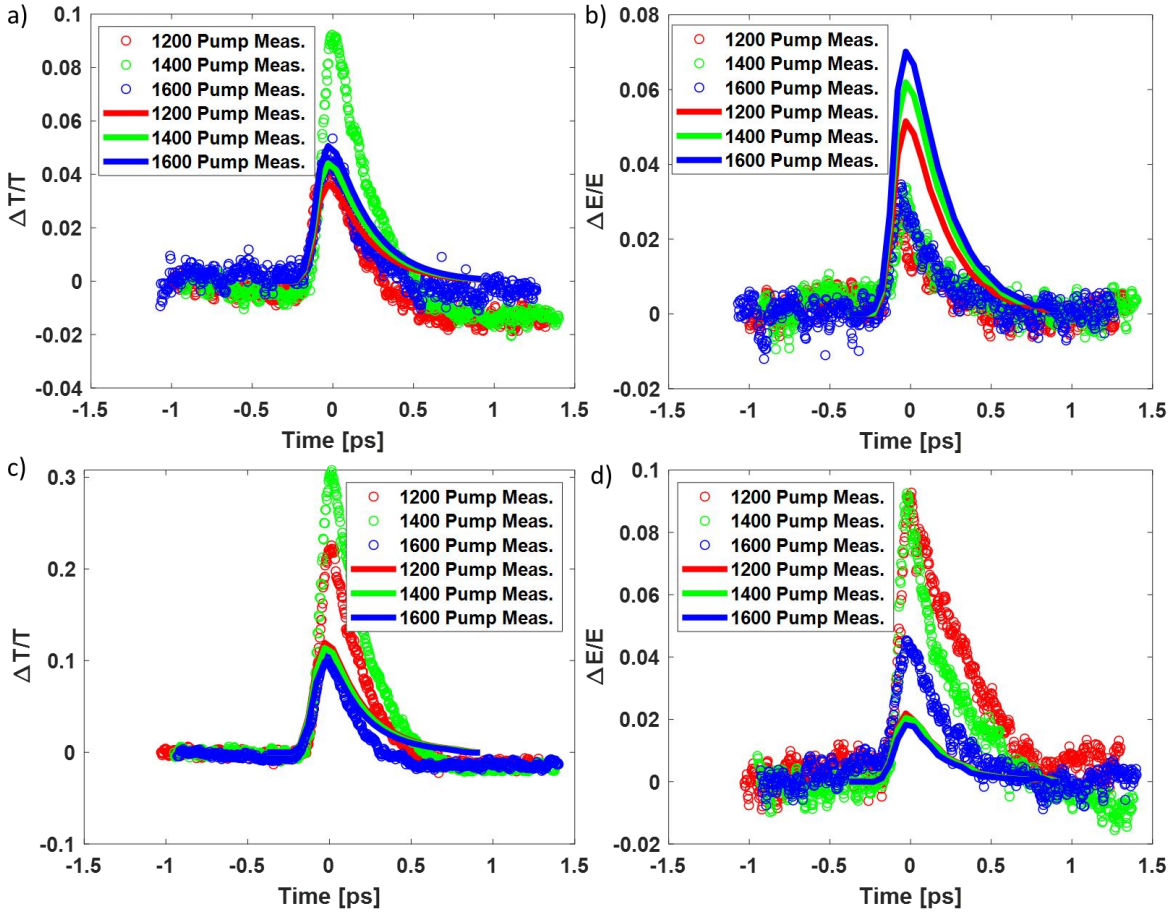

Figure 37 Nonlinear beam deflection measurements at probe wavelength of 1400 nm in $\Delta T/T$ (a,c) and $\Delta E/E$ (b,d) for films S120 (a,b) and S240 (c,d) for three pump wavelengths, 1200 nm (blue), 1400 nm (green), and 1600 nm (red) and an intensity $\sim 125 GW/cm^2$. For both films, this is near the ideal probing wavelength for index modulation, though large transmission changes in S240 obscures this result.

Measurements at 1400 nm probe follow similar trends to those of 1200 nm (Figure 37). Notable differences include an increase in $\Delta T/T$ for S240 which will continue to increase due to the low initial transmission. Here, $\Delta E/E$ has significant contributions due to both a transmission modulation and an index modulation. S120 follows similar trends, however, transmission modulation is still small and there for most of the deflection is caused by the index gradient as the probe is in the ideal probing wavelength for this film.

Through beam deflection measurements, we were able to confirm the trends our model predicts in every combination. Our deflection data supports the calculation of the ideal wavelength index modulation occurring near the ENZ wavelength of the film. The amplitude of transmission modulation also matches well to theoretical models supporting the theory derived.

6.2.2. Experimental Measurement of Time Dependent Nonlinear Reflection-Transmission in Epsilon-Near-Zero Materials

For two GZO films grown by molecular beam epitaxy (MBE), S4 and S5, nonlinear RT measurements were conducted at three pump wavelengths, 1350 nm, 1620 nm, and 1890 nm. The film qualities were characterized through ellipsometry, permittivity shown in Figure 38, and are presented in Table 6. Each of the films has a thin ZnO matching layer to improve the quality of growth of GZO.

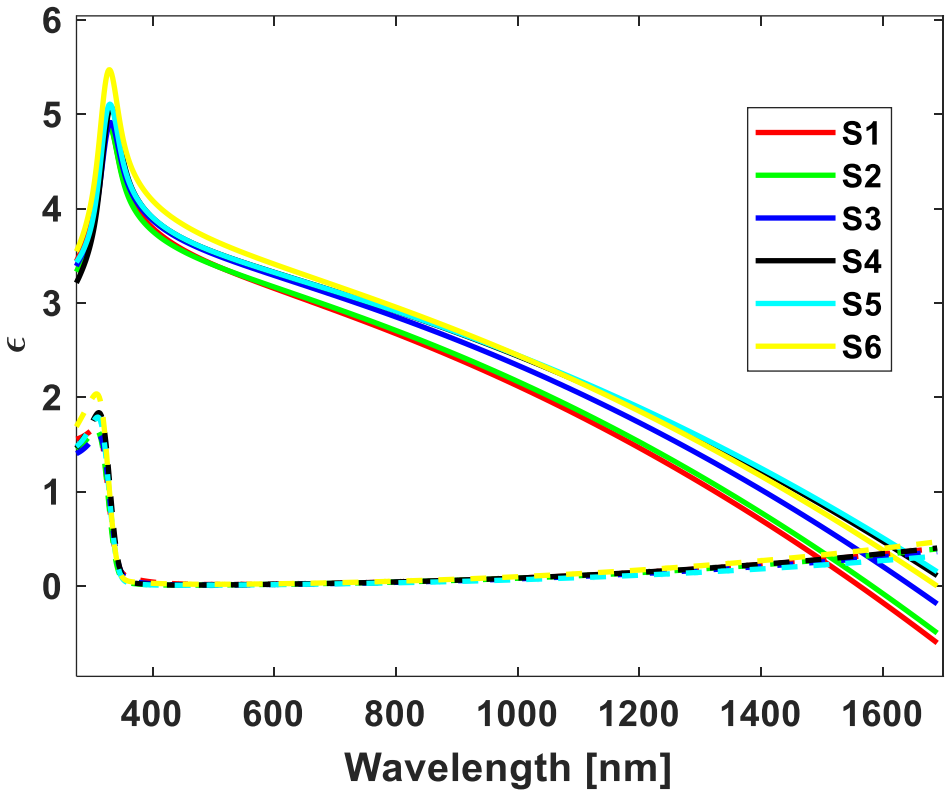

Figure 38 Real (solid) and imaginary (dashed) permittivity of S1-S6 as measured through ellipsometry.

Table 6 Sample characteristics for samples used in nonlinear RT measurements

Sample	Film ENZ [μm]	ε" at ENZ	Carrier Density [$\times\ 10^{26} cm^{-3}$]	Effective Mass [$\times m_0$kg]	Thickness [nm]
S1	1.56	0.31	5.58	0.369	207
S2	1.58	0.32	5.41	0.366	210
S3	1.65	0.33	4.87	0.359	260
S4	1.7	0.41	4.51	0.354	225
S5	1.71	0.31	4.44	0.353	280
S6	1.69	0.48	4.58	0.355	175

Experiments were conducted through collaboration at Argonne National Labs with a white light probe and a 60 fs pump laser. The pump pulse is chopped at 2.5kHz with a system repetition rate of 5kHz. The white light probe was detected at 5kHz directly measuring the difference between the pumped and linear properties to generate $\Delta T/T$ and $\Delta R/R$. A grating and CCD detector are used to measure the spectral response of the white light probe. Transmission measurements were conducted at 5 degrees off normal incidence while reflection was taken at 30 degrees. The pump was horizontally polarized while the probe was vertically polarized. The pump beam was measured at 700 µm $FW1/e$ while the probe was a slightly reduced size. FTIR measurements were used to confirm the linear transmission and reflection of each film. Theoretical comparisons made use TMM calculations at normal incidence for transmission and 30 degrees off normal with TM polarization with 5% reflection added to adjust for non-idealities.

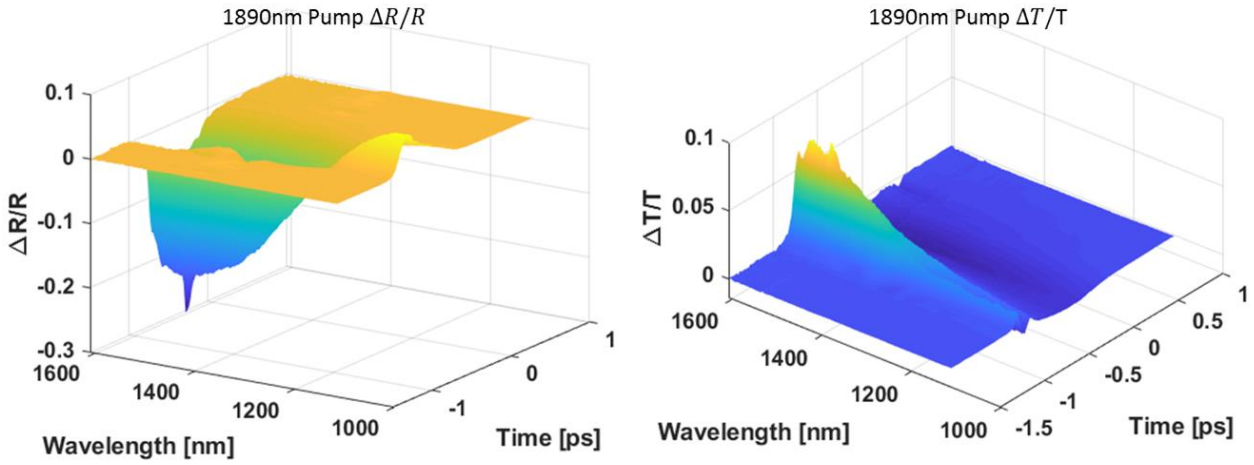

Figure 39 Temporal and Spectral measurements of $\Delta R/R$ (left) and $\Delta T/T$ (right) for S4 pump at an average power of ~8mW. The reflection modulation includes a large negative region from the film becoming less metallic, as well as a positive region due to an impedance matching condition that leads to a region of low reflection. Measurements taken at Argonne Nat. Labs.

Full temporal and spectral measurements are taken for each measurement as shown in Figure 39. Transmission is expected to only increase due to the film becoming less metallic/more dielectric. Reflection is expected to decrease in most of the spectral range; however, a region of increased reflection occurs due to a natural minimum in linear reflection from an impedance matching condition. Near this impedance matching condition, an increase in refractive index results in an increase in reflection as the matching condition redshifts.

Temporal measurements demonstrate a complete relaxation within 1ps for a relaxation rate consistent with other measurements, $\tau \sim 200 fs$. This result suggests that the intraband relaxation dynamics are unaffected between higher quality (lower loss) MBE grown ZnO doped with gallium and lower quality (higher loss) PE:ALD grown ZnO doped with aluminum.

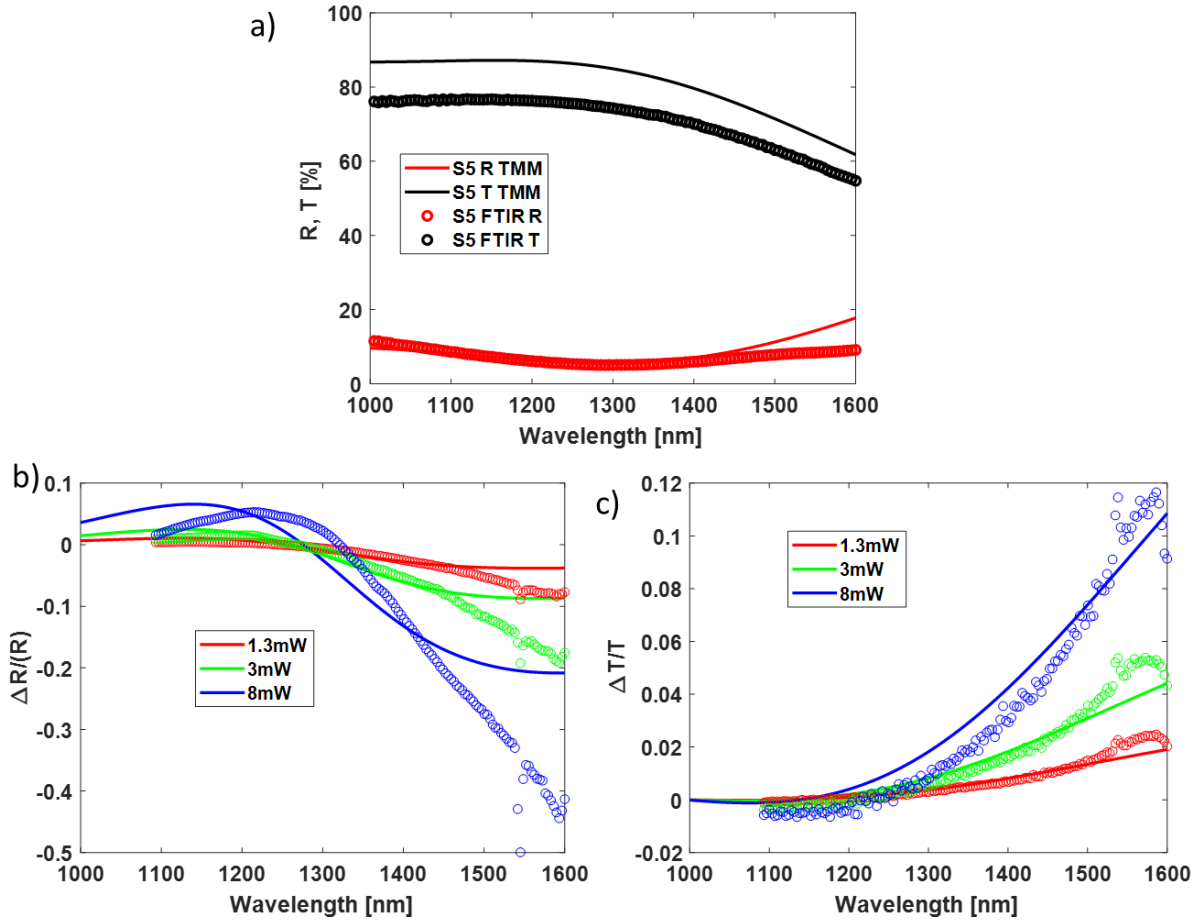

Figure 40 a) Comparison of TMM calculated RT spectra and FTIR measured RT spectra for sample S4. Due to non-idealities such as a 30 nm ZnO buffer layer, a small error exists in the total reflection and transmission for the film. This leads to theoretical error in comparison to experimental results shown in b,c. Intensity dependence of nonlinear RT measurements for sample S5 at three average powers, 1.3mW, 3mW, and 8mW, pumped at 1620 nm. Reflection (b) and transmission (c) follow the expected trend of increased modulation as power is increased. Absolute magnitude of modulation of reflection is higher due to the low initial reflection. Significant error at long wavelengths is attributed to the linear TMM deviation from linear FTIR data. Measurements taken at Argonne Nat. Labs.

A logical first check for nonlinear dependence is reflection and transmission modulation. For transmission measurements, Figure 40 (c), the trend simply follows increased transmission modulation with increased intensity. For reflection measurements Figure 40 (b), the dependence is slightly different in that the region of increased reflection redshifts and increases in intensity

with increased intensity. This occurs because that region is shifted further with increased plasma frequency modulation. Some error exists, especially at long wavelengths, due to a discrepancy between FTIR measured reflection and transmission and the TMM calculated reflection and transmission.

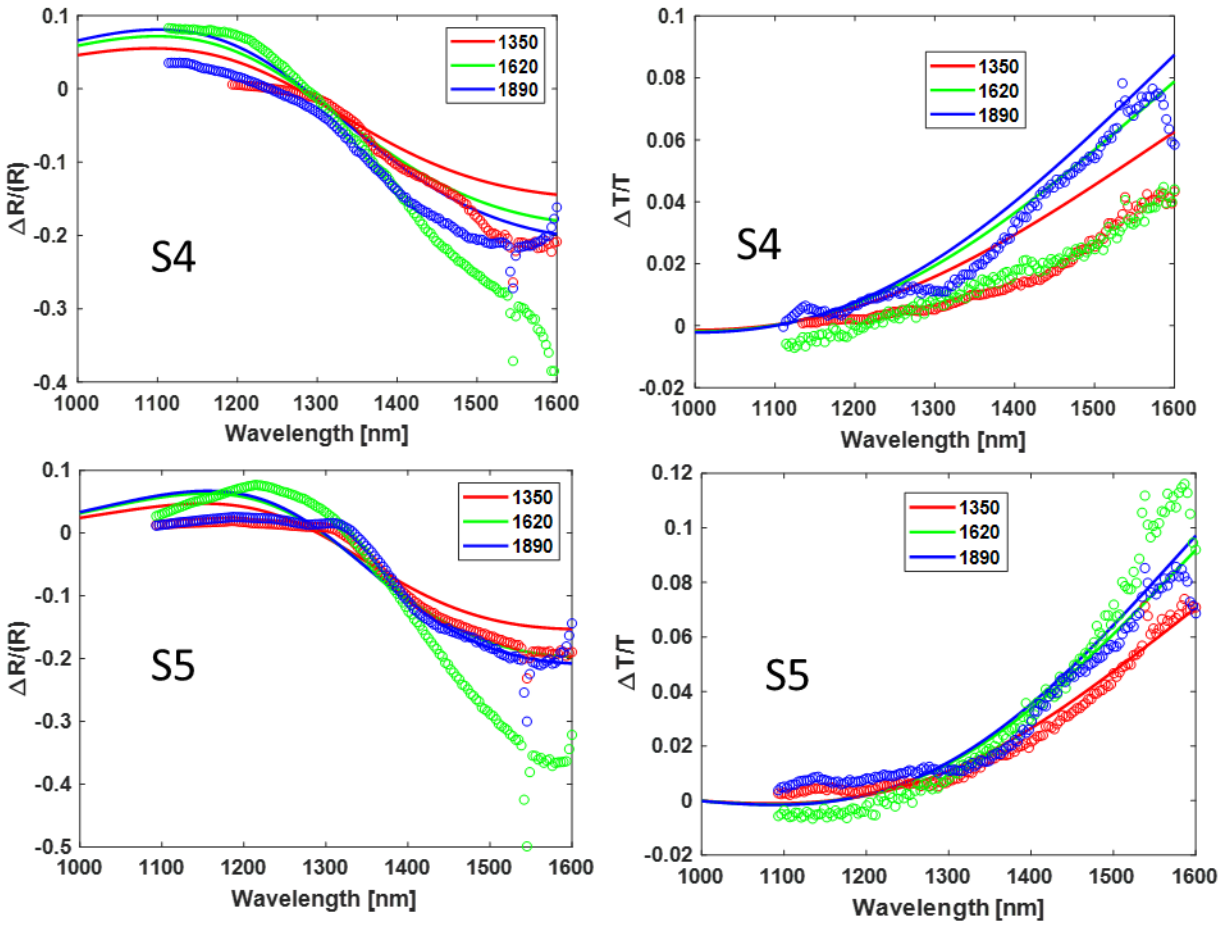

Figure 41 Nonlinear reflection (a,c) and transmission (b,d) measurements (open points) and theoretical matching (solid lines) for films S4 (a,b) and S5(c,d) pumped at an average power of ~8mW (experimental), $\sim 80 GW/cm^2$ (theory). Due to an increased thickness from S4 to S5 the preferred pumping regime shifts from 1890 in S4 to nearly identical response between 1890 and 1620 in S5. Measurements taken at Argonne Nat. Labs.

A comparison of samples S4 and S5 yields a similar comparison to S120 and S140 from Section 6.2.1 in that S4 falls into the transitional thickness before absorption is pinned to ENZ, while S5 falls into the pinned thickness. This distinction is not firm as it depends on film loss and permittivity; however, results indicate that S4 is pumped more efficiently by the 1890 nm pump while S5 is pumped more efficiently by both the 1620 nm pump and the 1890 nm pump. The measured results share the same trend at other powers (not shown). Theoretical calculations show a good agreement limited by the inaccuracy of our TMM calculations and error of experimental results. The TMM calculations used did not consider the ZnO substrate, nor thickness dependence of absorption, leading to error which may be alleviated in future calculations. Experiments in $\Delta R/R$ are particularly prone to error due to the low initial reflection of samples.

6.3. Experimental Nonlinear Reflection and Transmission Measurements of Interband Nonlinearities in Epsilon-Near-Zero

To verify the model, nonlinear reflection measurements were conducted on a GZO film with ENZ $\varepsilon(\lambda_{ENZ} = 1700nm) = 0 + i0.41$ and a thickness of 225 nm grown on 24 nm of ZnO on a c-plane sapphire substrate [43–45]. Linear optical properties were determined via variable angle spectroscopic ellipsometry (J.A. Woollam M-2000) [46], performing successive measurements of the sapphire substrate, ZnO/sapphire, and finally, GZO/ZnO/sapphire to ensure accurate extraction. Nonlinear pump-probe experiments were conducted through collaboration with measurements taken at Argonne National Labs for both a near-infrared pump at 1890 nm (to excite an intraband effect) and an ultraviolet pump at 325 nm (to excite an interband effect), each with a 60 fs pulse width, see Figure 42a. A white light probe is generated from the pump by

focusing the beam inside a 5 mm thick sapphire crystal and is used to observe the change in the sample's reflection and transmission over the range of 1150 nm – 1600 nm using a pair of CCDs (Ultrafast Systems Cam NIR-2). The pump pulse is chopped at 2.5 kHz with a laser repetition rate of 5 kHz. The white light probe was detected at 5 kHz therefore directly measuring the difference between the pumped and unpumped sample to generate $\Delta R/R$. Reflection data was taken at 30° from the sample normal. In all cases the pump was horizontally polarized while the probe was vertically polarized and in the same plane to minimize two-beam coupling effects [47]. The peak irradiance of the IR pump at 1890 nm was 13, 33, and 83 GW/cm^2 (P_{avg} = 1.3, 3.3 and 8.3 mW, respectively) and 1, 2, 6, and 14 GW/cm^2 (P_{avg} = 0.2, 0.5, 1.3 and 3.1 mW, respectively) for the UV pump at 325 nm with results shown in see Figure 43a,b,c,d.

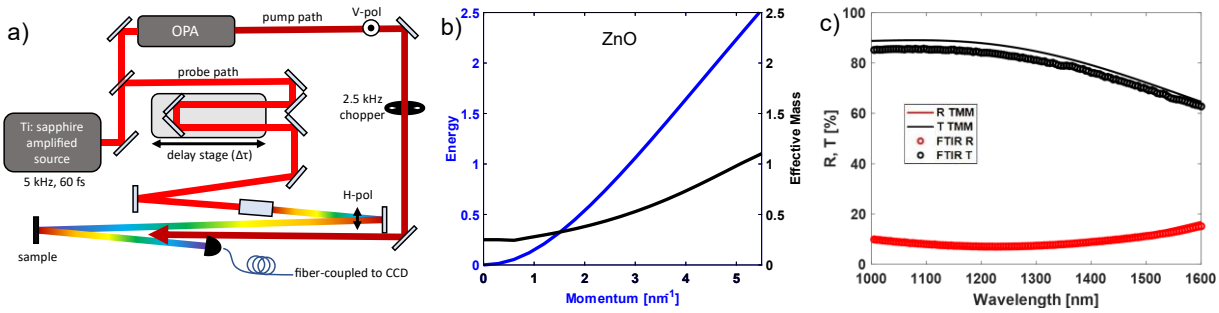

Figure 42 a) Experimental Setup for nonlinear reflection measurements of GZO. b) Energy-momentum diagram of ZnO near the Γ point towards A. c) Transfer-matrix-method calculations for the GZO sample compared to the measured FTIR data for the GZO sample.

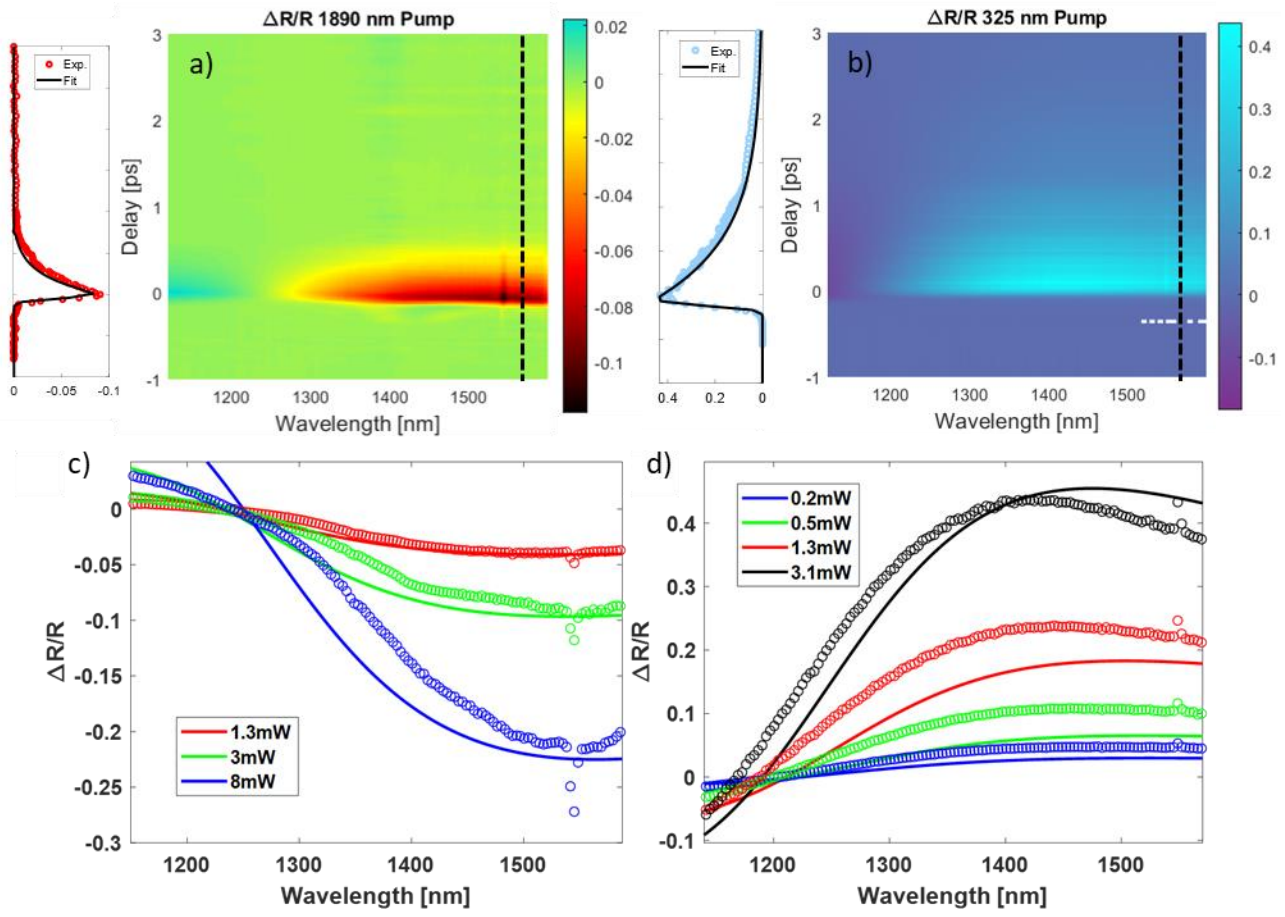

Figure 43 a) Surface plot of nonlinear reflection for a white light probe with wavelengths of 1120 to 1600nm and a delay time of -1ps to 3ps a) pumped with 3mW at 1890nm and b) pumped with 3.1mW at 325nm. Cutlines taken at 1565nm for each show the temporal dynamics of the film. Nonlinear reflection comparison of theory (solid) to experimental (dot) c) pumped at 1890nm with 1.3 (red), 3.3 (green) and 8.3mW (blue) average power and d) pumped at 325nm with 0.2 (blue), 0.5 (green), 1.3 (red) and 3.1mW (black) average power.

Taking the E-*k* diagram of Ga-doped ZnO, shown in Figure 42b, as well as the experimental parameters, the theory can predict the peak magnitude of the change in reflection versus irradiance and probe wavelength for both inter- and intraband nonlinear effects without fitting parameters, see Figure 43c,d. Variations between the predicted linear reflection of the sample and the reflection as measured through FTIR account for some error in the spectral location of the theoretical curves compared to measured results, particularly in the short wavelength region

of Figure 43c.When observing the results, we note the change in sign of the normalized reflection both pumping scenarios. The refractive index of our film is less than unity for the majority of wavelengths, wherein excitation can be thought of as moving the material closer to an impedance matching condition with air (intraband) or becoming further mismatched (interband). However, for short wavelengths, the linear impedance of the GZO is already close to that of air, and thus, at shorter wavelengths, the behavior is reversed.

Utilizing the white light probe, the model can be tested for a broad range of wavelengths in a single measurement. The spectral dependence of reflection and transmission change specifically confirms the plasma frequency modulation. In the case of interband pumping, the zero point clearly blueshifts, while in intraband it clearly redshifts.

6.4. Multi-Pump Nonlinear ENZ Measurements

Our final experiments aim to bring all relevant theories to the same platform by performing both interband and intraband nonlinear studies through a dual pumping system, see Figure 44. The interaction of the two pumps individually, compared to simultaneous pumping provides insight into how the individual processes interact and couple. Moreover, the combination of these effects allows for additional versatility in designing the temporal refractive index of the material as well as controlling nonlinear absorption and phase shifts.

The system follows the same design as the beam deflection experiments; however, the pump TOPAS/NIRUVIS is used to generate a 300 nm wavelength through cascaded second harmonics. The residual power of the 1200 nm to 600 nm conversion is used as a second pump with the probe independently controlled through a second TOPAS. The UV pump line is fitted with a

manual delay line and a UV-fused silica 125mm focal lens is used to focus the pump onto the sample at ~20 degrees.

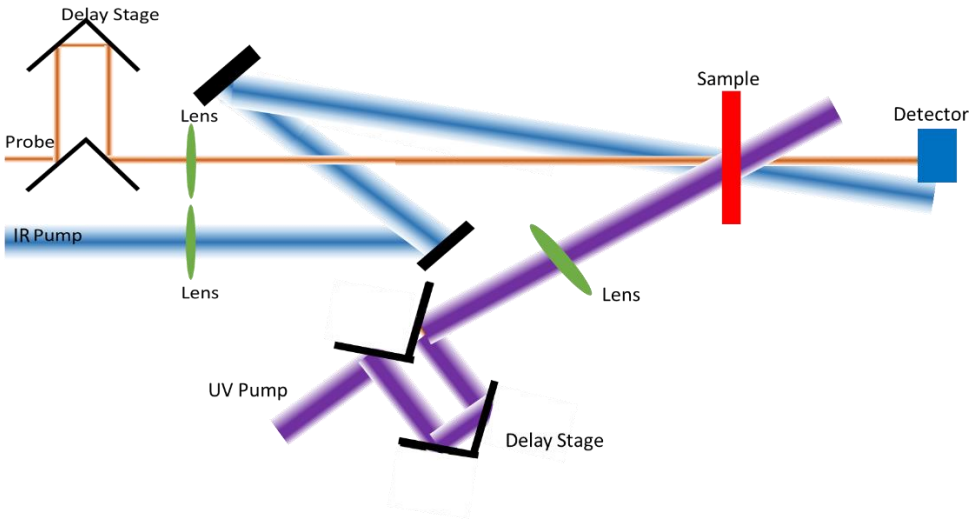

Figure 44 A Schematic Diagram for a dual pump-probe experimental set up. Both the delay line and the UV pump are fitted with delay stage to allow for individual timing control of all beams. All three beams are focused to the sample with both pump beam sizes around $HW1/e^2 \sim 500\mu m$ and the probe size around $HW1/e^2 \sim 100\mu m$.

Using a probe at 1400 nm, with $HW1/e^2 \sim 100\mu m$ and the 1200 nm and 300 nm pumps, with $HW1/e^2 \sim 600\mu m$, we can characterize the effect of each pump individually and near temporal overlap. A manual delay line is used to control the timing of the 300 nm pump. The 1200 nm pump intensity is taken to be $\sim 90 GW/cm^2$ with a UV pump $\sim 15 GW/cm^2$. Theoretical calculations were conducted with these pump intensities, assuming the probe resides in the center of both pumps that are spatially overlapped. Results are shown in Figure 45.

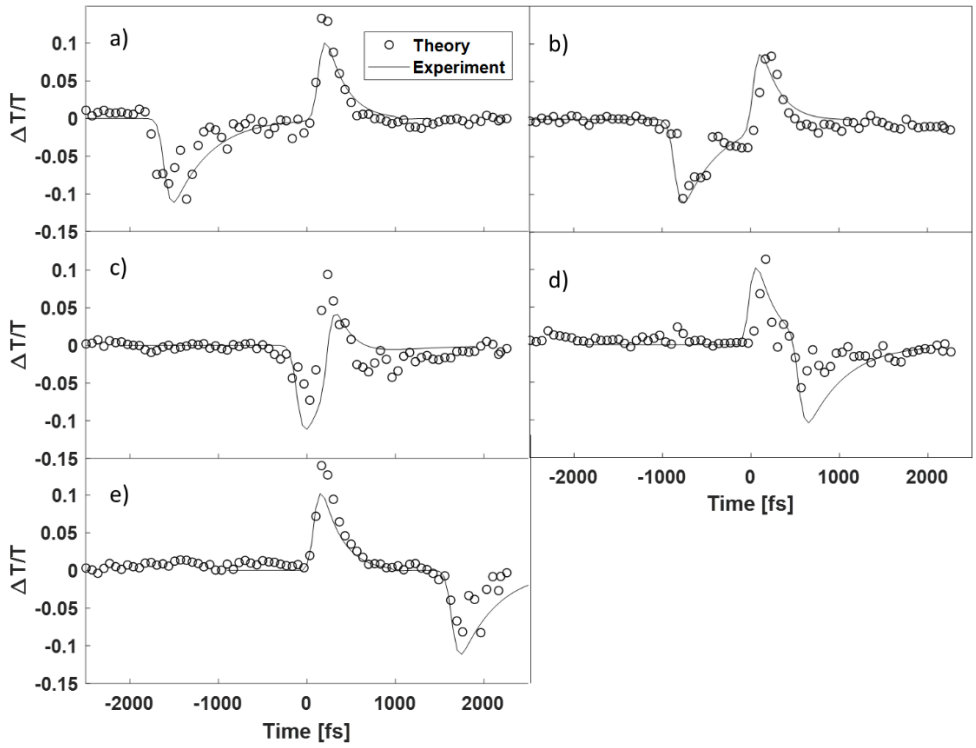

Figure 45 Nonlinear transmission measurements for a dual pump system with pumps at 300 nm and 1200 nm with a probe at 1400 nm. The delay between IR pump and UV pump are taken to be $-1700fs, -800fs, -150fs, 600fs, and\ 1600fs$ respectively for a,b,c,d, and e. At large delays the effects can be considered independent. At delays near zero, quenching effects can be seen with conflicting pump effects.

The results of this study show the relaxation rate of the interband nonlinearities to be slightly elongated (~400 fs) compared to the relaxation of the intraband nonlinearity (~220 fs). Figure 45(a,e) show independent nonlinearities while Figure 45 (b-d) show the interaction between pumps with overlapping effects. Quenching of effects can be seen with peak transmission modulation of both effects reducing compared to that of the independent effect. Theoretical curves fit well to experimental measurements. Further studies may yield supportive results for the physics laid out in Section 5.

To further investigate the behavior of this film, specifically the relaxation rate and behavior at overlap, more measurements were taken with a focus on temporal overlap. Using an IR pump of

$60GW/cm^2$ at 1200 nm and a UV pump of $12GW/cm^2$ perfectly overlapped with the probe at 1400 nm, measurements were taken with about 1.3 ps of delay between pumps, and a second with -0.13ps of delay.

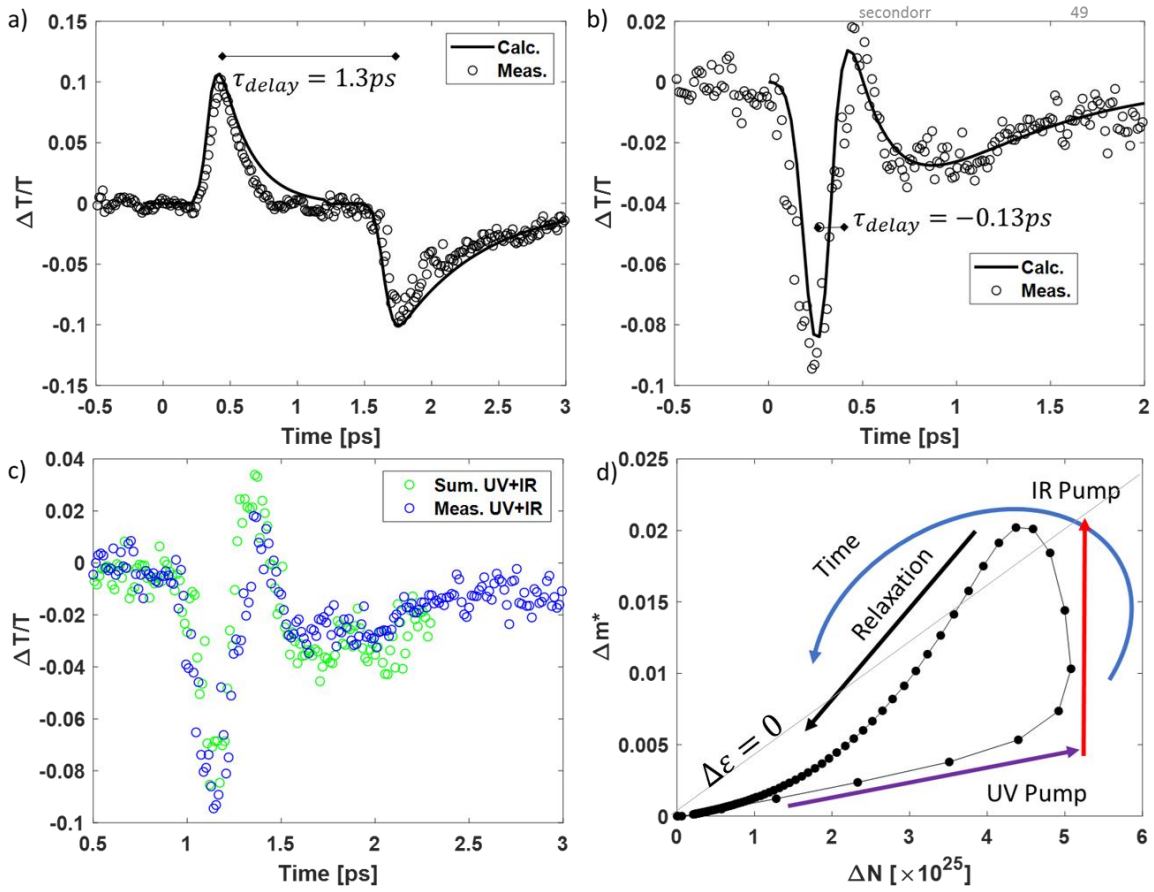

Figure 46 Transmission modulation measured with 1.3 ps of delay between IR and UV pumps (a) and -0.13 ps of delay. The measurements were taken with an IR pump of $60GW/cm^2$ at 1200 nm and a UV pump of $12GW/cm^2$ perfectly overlapped with the probe at 1400 nm. Relaxation rates are calculated as 220 fs for IR and 600 fs for UV. This enables a straddled relaxation where the IR peak relaxes inside the shape of the UV. c) The signal from b) compared to a sum of the UV and IR measurements from a) with proper delay between signals included. The comparison of full measurement and simple addition show the interaction of the UV and IR pumps. d) The calculated change in carrier density and effective mass as a function of time (points every 30 fs). The grey line indicates zero change in permittivity due to equal contribution of carrier change and effective mass change. Above the line denotes a positive change in permittivity while below the line denotes a negative change.

The transmission modulation of separated and overlapped pumps in time are shown in Figure 46a and b respectively. In both cases the model is found to fit well to the experimental results. Since this model is a simple summation of the two effects in time, this indicates that there are no cross-coupling effects for the irradiance levels tested. This is further illustrated by Figure 46c wherein the uncoupled UV and IR index modulation produced from Figure 46a were separated and temporally shifted to approximate the results of Figure 46b with -0.13 ps delay. It is observed that the simple summation and shift (Sum UV+IR) of the experimental data matches quite well to the simultaneous excitation (Meas. UV+IR).

Given this successful modeling, Figure 46d illustrates another useful approach at plotting the temporal evolution of the system versus the change in effective mass and carrier concentration. The UV pump induces both a carrier density increase and an effective mass increase while the IR pump only changes effective mass. A grey line denotes the cancellation of carrier concentration change and effective mass change on the plasma frequency. Above this line, the plasma frequency redshifts as IR is dominant, and below the line, the plasma frequency blueshifts as the UV pump is dominant. As shown in the experimental combination, the film spends most of the interaction in below the grey line, where transmission is reduced, and has a brief period of time above the line before returning below the line while relaxing to zero.

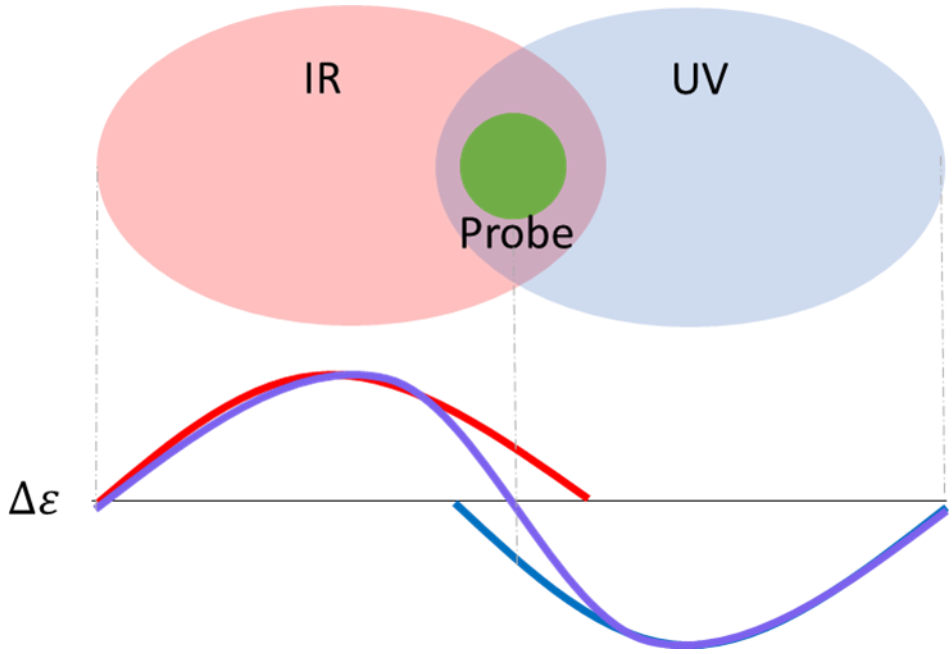

Figure 47: Schematic depiction the overlap of UV and IR pumps in space with the change in permittivity induced show below. The probe is located in the overlap of each pump where the spatial index change is significantly stronger than from induvial pumps.

While the previous measurements were conducted with perfectly overlapped pumps and probe, enhanced deflection can be found by overlapping the pump and probe in a beam deflection set up. By positioning the probe at the 1/e point of each pump, with pumps on opposite sides (See Figure 47), the deflection effects can be engineered to add together. This occurs as the nonlinear prism forms with the high index at the peak in intraband but the peak of the interband nonlinear has a lowered index. When the pulses are equal and opposite, this leads to a null change in index at the center of the probe, with a decreased index on the interband side, and an increased index on the intraband side. These effects combine to cause twice the deflection that would be found from a single pump due to the increased slope ($\theta \propto dn/dx$, see section 6.1.1), while having a neutral effect on total transmission. Following previous methods, we can investigate the effect in S240 in a dispersive region (1200 nm) and a non-dispersive region (1400 nm).

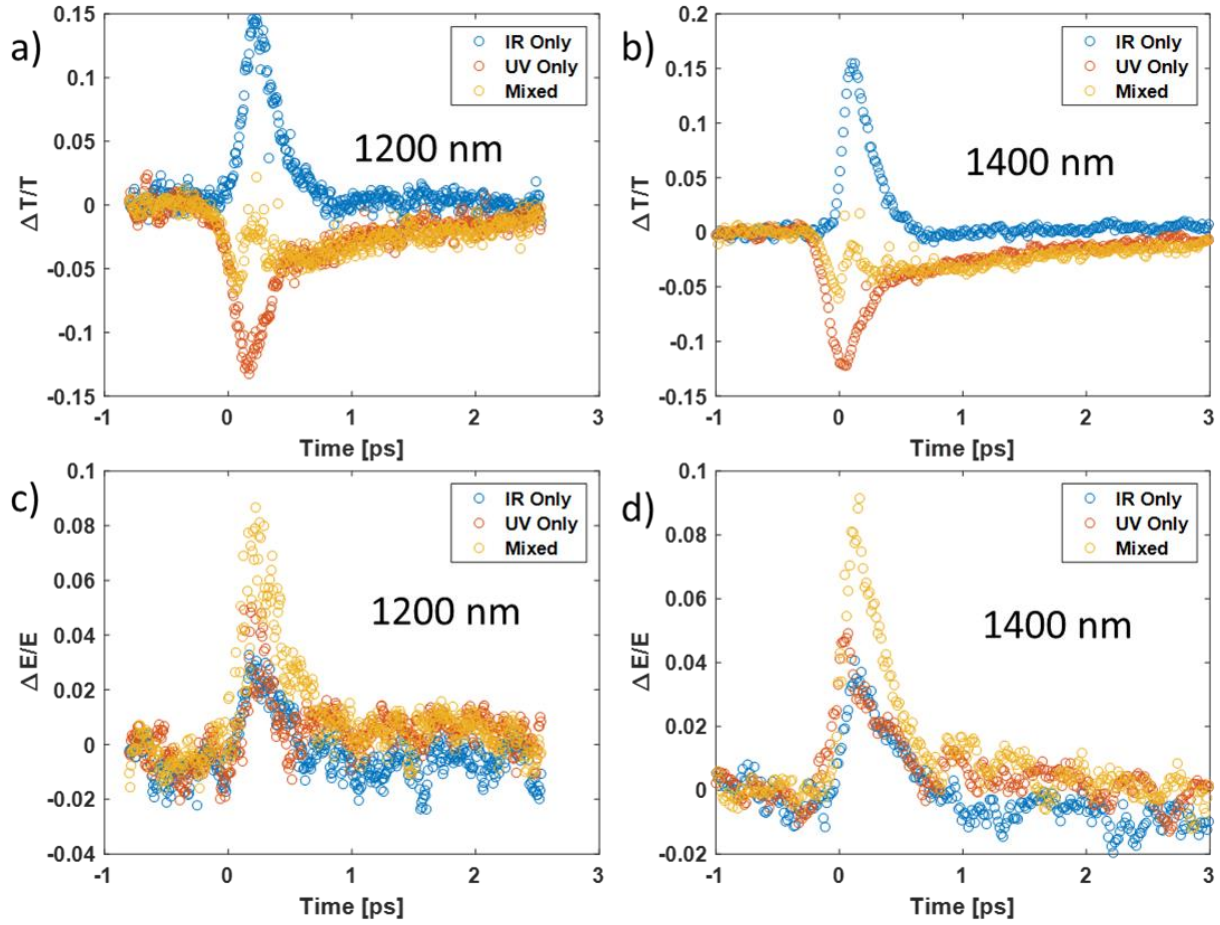

Figure 48 Beam deflection measurements at 1200 nm (a,c) and 1400 nm (b,d) probe wavelengths with a 1200 nm pump (blue), 300 nm pump (red), and both (yellow). In both cases, beam deflection (c,d) is doubled by an additive effect between pump responses while transmission (a,b) nearly cancels. This result enables ultra-large beam deflection and breaks traditional saturation of the effect by using opposing nonlinearities.

In both a dispersive region (Figure 48a,c) and a non-dispersive region (Figure 48, b,d), the nonlinear effect induces twice the effective beam deflection (Figure 48c,d) while approaching a neutral transmission change. Experimentally, the individual pumps were chosen to produce similar transmission and deflection amounts (~15% and 4% respectively). When combined, the transmission change peaks near 0% and the deflection peaks near 8%. This effect is consistent due to transmission modulation following the same spatial trends as index gradient with

increased transmission on the intraband pump side and decreased transmission on the interband pump side. Similar to previous experiments, the temporal difference between relaxation of interband and intraband result in a negative dip in transmission before and after the peak. However, the deflection signal is not affected by the time difference due to the additive nature of the effect.

Multi-pump nonlinear studies provide opportunities to see ultrafast nonlinear signals through transmission modulation such as in Figure 48a,b, and in deflection such as in Figure 48c,d. In Figure 48a, a signal modulation from zero to zero is shown in ~200 fs through the quenching of the interband effect through the intraband effect. This effectively alters the rate of change from a “slow” nonlinearity with a relaxation of 600 fs to a correlation limited bandwidth where the temporal width of effect is nearly the cross correlation of pump and probe times. This increased rate of change could be utilized for temporal beam shaping such as bisecting a 1ps probe in time. By utilizing the beam deflection mode a similar bisection can be created with the altered section of the probe deflected rather than reflected. Utilizing more pumps, this opens an avenue for general control of a surface through spatial and temporal control of pump beams. With a positive and negative index variation available, this enables complex signal constructions.

7. CONCLUSION

Research into nonlinear optical processes in Drude-type epsilon-near-zero materials has been a recent focus due to their large response and high damage threshold. To gain insight into the physics underpinning nonlinear optical modulation of the refractive index in these materials, we derived new operational forms for the nonlinear response. This theory is the most holistic understanding of the nonlinear process for ENZ nonlinearities to date.

The model has been rigorously tested through experimental means of beam deflection and reflection-transmission modulation for aluminum-doped zinc oxide and gallium doped zinc oxide respectively. The experiments presented herein are among the first of their kind using beam deflection as the nonlinear technique to study ENZ nonlinearities and is a promising avenue to explore transient, spectral, polarization, and angularly resolved nonlinear responses with high accuracy. This work also addresses a distinct lack of studies on gallium-doped zinc oxide rather than aluminum-doped zinc oxide, providing rigorous studies in wavelength, thickness, power, and optical loss through our transient reflection-transmission measurements. Lastly, early results of the first known multi-pump beam deflection measurements of ENZ films were presented, showing an opportunity for additive nonlinear responses in deflection while operating at negligible transmission modulation.

Through this, the developed theory allows for the interrogation and prediction of trends to find ideal films and experimental configurations. Among them, investigations note gallium nitride as a promising material for intraband ENZ nonlinear optical application due to its large energy band non-parabolicity, albeit with poor interband operation. Similarly cadmium oxide is suggested as a promising interband nonlinear material due to its very parabolic energy band, but is less suited for intraband operation.

Utilizing the holistic theory and the prediction power entailed, researchers may continue to push the frontiers of nonlinear optics with ENZ materials. While the theory is established for thin films with bulk properties, the physics is established and applicable for structured devices to further engineer or tailor the nonlinear response for given applications. By combining the developed framework with a suitable electromagnetics solver, the response of nanostructures coupled to ENZ films can be predicted readily, thereby enabling the optimization of energy localization and effective refractive index dispersion to enhance nonlinear responses. Additionally, multilayer stacking of individual films may also be a useful application enabling opportunities for further enhancements of specific operations such modulating perfect absorption [121].

While epsilon-near-zero optics suffers from loss, the ability to perform large modulation of the refractive index on sub-micron length scales is a fantastic opportunity for continued nonlinear optical operations. I expect the compact, strong nonlinear interaction of ENZ materials, both current and upcoming, to become a mainstay in research that will provide a wide range of opportunities for improvement through fabrication and design.

8. REFERENCES

1. O. Reshef, I. De Leon, M. Z. Alam, and R. W. Boyd, "Nonlinear optical effects in epsilon-near-zero media," Nat. Rev. Mater. 1 (2019).
2. I. Liberal and N. Engheta, "Near-zero refractive index photonics," Nat. Photonics **11**, 149–158 (2017).
3. N. Kinsey, C. DeVault, A. Boltasseva, and V. M. Shalaev, "Near-zero-index materials for photonics," Nat. Rev. Mater. (2019).
4. R. Secondo, J. Khurgin, and N. Kinsey, "Absorptive loss and band non-parabolicity as a physical origin of large nonlinearity in epsilon-near-zero materials," Opt. Mater. Express **10**, 1545 (2020).
5. M. Clerici, N. Kinsey, C. DeVault, J. Kim, E. G. Carnemolla, L. Caspani, A. Shaltout, D. Faccio, V. Shalaev, A. Boltasseva, and M. Ferrera, "Controlling hybrid nonlinearities in transparent conducting oxides via two-colour excitation," Nat. Commun. **8**, 15829 (2017).
6. L. Caspani, R. P. M. Kaipurath, M. Clerici, M. Ferrera, T. Roger, J. Kim, N. Kinsey, M. Pietrzyk, A. Di Falco, V. M. Shalaev, A. Boltasseva, and D. Faccio, "Enhanced Nonlinear Refractive Index in ε-Near-Zero Materials," Phys. Rev. Lett. **116**, 233901 (2016).
7. R. W. Boyd, *Nonlinear Optics* (Academic Press, 2008).
8. I. C. Reines, M. G. Wood, T. S. Luk, D. K. Serkland, and S. Campione, "Compact epsilon-near-zero silicon photonic phase modulators," Opt. Express **26**, 21594 (2018).
9. Y. Wang, A. Capretti, and L. Dal Negro, "Wide tuning of the optical and structural properties of alternative plasmonic materials," Opt. Mater. Express **5**, 2415 (2015).

10. G. V. Naik, J. Kim, and A. Boltasseva, "Oxides and nitrides as alternative plasmonic materials in the optical range [Invited]," Opt. Mater. Express **1**, 1090 (2011).

11. N. M. Khusayfan and M. M. El-Nahass, "Study of structure and electro-optical characteristics of indium tin oxide thin films," Adv. Condens. Matter Phys. **2013**, (2013).

12. Z. Ma, Z. Li, K. Liu, C. Ye, and V. J. Sorger, "Indium-Tin-Oxide for High-performance Electro-optic Modulation," Nanophotonics **4**, 198–213 (2015).

13. J. Lian, D. Zhang, R. Hong, P. Qiu, T. Lv, and D. Zhang, "Defect-induced tunable permittivity of epsilon-near-zero in indium tin oxide thin films," Nanomaterials **8**, (2018).

14. R. Amin, R. Maiti, Z. Ma, M. Miscuglio, H. Dalir, and V. J. Sorger, "An ITO-based Mach-Zehnder Modulator with Lateral MOS-Capacitor on SOI Platform," in (The Optical Society, 2019), p. JW3A.67.

15. M. Girtan, "Comparison of ITO/metal/ITO and ZnO/metal/ZnO characteristics as transparent electrodes for third generation solar cells," Sol. Energy Mater. Sol. Cells **100**, 153–161 (2012).

16. F. Ruske, A. Pflug, V. Sittinger, B. Szyszka, D. Greiner, and B. Rech, "Optical modeling of free electron behavior in highly doped ZnO films," Thin Solid Films **518**, 1289–1293 (2009).

17. A. Singh, M. Kumar, R. M. Mehra, A. Wakahara, and A. Yoshida, "Al-doped zinc oxide (ZnO:Al) thin films by pulsed laser ablation," J. Indian Inst. Sci. **81**, (2001).

18. H. Morkoç, *Handbook of Nitride Semiconductors and Devices* (Wiley-VCH, 2009), Vol. 1.

19. H. Y. Liu, V. Avrutin, N. Izyumskaya, Ü. Özgür, A. B. Yankovich, A. V. Kvit, P. M. Voyles, and H. Morkoç, "Electron scattering mechanisms in GZO films grown on a-sapphire substrates by plasma-enhanced molecular beam epitaxy," J. Appl. Phys. **111**, 103713 (2012).

20. P. H. Jefferson, S. A. Hatfield, T. D. Veal, P. D. C. King, C. F. McConville, J. Zúñiga-Pérez, and V. Muñoz-Sanjosé, "Bandgap and effective mass of epitaxial cadmium oxide," Appl. Phys. Lett. **92**, (2008).

21. E. Sachet, C. T. Shelton, J. S. Harris, B. E. Gaddy, D. L. Irving, S. Curtarolo, B. F. Donovan, P. E. Hopkins, P. A. Sharma, A. L. Sharma, J. Ihlefeld, S. Franzen, and J. P. Maria, "Dysprosium-doped cadmium oxide as a gateway material for mid-infrared plasmonics," Nat. Mater. **14**, 414–420 (2015).

22. A. Wang, J. R. Babcock, N. L. Edleman, A. W. Metz, M. A. Lane, R. Asahi, V. P. Dravid, C. R. Kannewurf, A. J. Freeman, and T. J. Marks, "Indium-cadmium-oxide films having exceptional electrical conductivity and optical transparency: Clues for optimizing transparent conductors," Proc. Natl. Acad. Sci. U. S. A. **98**, 7113–7116 (2001).

23. S. Saha, B. T. Diroll, J. Shank, Z. Kudyshev, A. Dutta, S. N. Chowdhury, T. S. Luk, S. Campione, R. D. Schaller, V. M. Shalaev, A. Boltasseva, and M. G. Wood, "Broadband, High-Speed, and Large-Amplitude Dynamic Optical Switching with Yttrium-Doped Cadmium Oxide," Adv. Funct. Mater. **30**, 1908377 (2020).

24. S. Benis, N. Munera, R. Acuña, D. J. Hagan, and E. W. Van Stryland, "Nonlinear Fresnel coefficients due to giant ultrafast nonlinearities in indium tin oxide (Conference Presentation)," in *Ultrafast Phenomena and Nanophotonics XXIII*, M. Betz and A. Y. Elezzabi, eds. (SPIE, 2019), Vol. 10916, p. 35.

25. M. Z. Alam, S. A. Schulz, J. Upham, I. De Leon, and R. W. Boyd, "Large optical nonlinearity of nanoantennas coupled to an epsilon-near-zero material," Nat. Photonics **12**, 79–83 (2018).

26. S. Benis, D. J. Hagan, and E. W. Van Stryland, "Enhancement Mechanism of Nonlinear Optical Response of Transparent Conductive Oxides at Epsilon-Near-Zero," in *Conference on Lasers and Electro-Optics* (OSA, 2018), p. FF2E.1.

27. M. Z. Alam, M. Z. Alam, I. De Leon, and R. W. Boyd, "Large optical nonlinearity of indium tin oxide in its epsilon-near-zero region," Science (80-.). **0330**, 0–5 (2016).

28. M. Fox, *Optical Properties of Solids*, 2nd ed. (Informa UK Limited, 2011), Vol. 52.

29. M. Marlo and V. Milman, "Density-functional study of bulk and surface properties of titanium nitride using different exchange-correlation functionals," Phys. Rev. B - Condens. Matter Mater. Phys. **62**, 2899–2907 (2000).

30. C. Ekuma, D. Bagayoko, G. L. Zhao, L. Franklin, and J. T. Wang, "First Principle Study of Electronic Structures of w-CdS, zb-CdS, w-ZnO and Ferro-NaNO2," † African J. Phys. **3**, 119–130 (2010).

31. L. D. Whalley, J. M. Frost, B. J. Morgan, and A. Walsh, "Impact of nonparabolic electronic band structure on the optical and transport properties of photovoltaic materials," Phys. Rev. B **99**, 085207 (2019).

32. X. Liu, J. Park, J. H. Kang, H. Yuan, Y. Cui, H. Y. Hwang, and M. L. Brongersma, "Quantification and impact of nonparabolicity of the conduction band of indium tin oxide on its plasmonic properties," Appl. Phys. Lett. **105**, (2014).

33. John Singleton, *Band Theory and Electronic Properties of Solids*, 4th ed. (Oxford University Press, 2008).

34. O. Reshef, I. De Leon, M. Z. Alam, and R. W. Boyd, "Nonlinear optical effects in epsilon-near-zero media," Nat. Rev. Mater. (2019).

35. J. B. Khurgin and N. Kinsey, "Adiabatic frequency conversion: it is all about group velocity," (2019).

36. J. B. Khurgin, "Slow light in various media: a tutorial," Adv. Opt. Photonics **2**, 287 (2010).

37. N. Kinsey and J. Khurgin, "Nonlinear epsilon-near-zero materials explained: opinion," Opt. Mater. Express **9**, 2793 (2019).

38. J. B. Khurgin, "Slow light in various media: a tutorial," Adv. Opt. Photonics **2**, 287 (2010).

39. G. V. Naik, V. M. Shalaev, and A. Boltasseva, "Alternative plasmonic materials: Beyond gold and silver," Adv. Mater. **25**, 3264–3294 (2013).

40. A. Capretti, Y. Wang, N. Engheta, and L. Dal Negro, "Comparative Study of Second-Harmonic Generation from Epsilon-Near-Zero Indium Tin Oxide and Titanium Nitride Nanolayers Excited in the Near-Infrared Spectral Range," ACS Photonics **2**, 1584–1591 (2015).

41. R. Secondo, D. Fomra, N. Izyumskaya, V. Avrutin, J. N. Hilfiker, A. Martin, Ü. Özgür, and N. Kinsey, "Reliable modeling of ultrathin alternative plasmonic materials using spectroscopic ellipsometry [Invited]," Opt. Mater. Express **9**, 760 (2019).

42. S. A. Maier, *Plasmonics : Fundamentals and Applications* (Springer, 2007).

43. A. A. Maradudin, J. R. Sambles, and W. L. Barnes, *Modern Plasmonics.* (Elsevier Science, 2014).

44. S. Kawata, Y. Inouye, and P. Verma, "Plasmonics for near-field nano-imaging and superlensing," Nat. Photonics **3**, 388–394 (2009).

45. N. Fang, H. Lee, C. Sun, and X. Zhang, "Sub-diffraction-limited optical imaging with a silver superlens.," Science **308**, 534–7 (2005).

46. M. Lahav, A. Vaskevich, and I. Rubinstein, "Biological sensing using transmission surface plasmon resonance spectroscopy," Langmuir **20**, 7365–7367 (2004).

47. A. Dutta, A. V. Kildishev, V. M. Shalaev, A. Boltasseva, and E. E. Marinero, "Surface-plasmon opto-magnetic field enhancement for all-optical magnetization switching," Opt. Mater. Express **7**, 4316 (2017).

48. J. M. Merlo, N. T. Nesbitt, Y. M. Calm, A. H. Rose, L. D'Imperio, C. Yang, J. R. Naughton, M. J. Burns, K. Kempa, and M. J. Naughton, "Wireless communication system via nanoscale plasmonic antennas," Sci. Rep. **6**, 1–8 (2016).

49. S. I. Bozhevolnyi, *Plasmonic Nanoguides and Circuits* (Distributed by World Scientific Pub, 2009).

50. N. Kinsey, M. Ferrera, V. M. Shalaev, and A. Boltasseva, "Examining nanophotonics for integrated hybrid systems: a review of plasmonic interconnects and modulators using traditional and alternative materials [Invited]," J. Opt. Soc. Am. B **32**, 121 (2015).

51. J. C. Ndukaife, A. V. Kildishev, A. G. A. Nnanna, V. M. Shalaev, S. T. Wereley, and A. Boltasseva, "Long-range and rapid transport of individual nano-objects by a hybrid electrothermoplasmonic nanotweezer," Nat. Nanotechnol. **11**, 53–59 (2016).

52. V. E. Ferry, M. A. Verschuuren, H. B. T. Li, E. Verhagen, R. J. Walters, R. E. I. Schropp, H. A. Atwater, and A. Polman, "Light trapping in ultrathin plasmonic solar cells," Opt. Express **18**, A237 (2010).

53. N. Meinzer, W. L. Barnes, and I. R. Hooper, "Plasmonic meta-atoms and metasurfaces," Nat. Photonics **8**, 889–898 (2014).

54. N. Yu and F. Capasso, "Flat optics with designer metasurfaces," Nat. Mater. **13**, 139–150

(2014).

55. S. Bagheri, C. M. Zgrabik, T. Gissibl, A. Tittl, F. Sterl, R. Walter, S. De Zuani, A. Berrier, T. Stauden, G. Richter, E. L. Hu, and H. Giessen, "Large-area fabrication of TiN nanoantenna arrays for refractory plasmonics in the mid-infrared by femtosecond direct laser writing and interference lithography [Invited]," Opt. Mater. Express **5**, 2625 (2015).

56. M. I. Stockman, K. Kneipp, S. I. Bozhevolnyi, S. Saha, A. Datta, J. C. Ndukaife, N. Kinsey, H. Reddy, U. Guler, V. M. Shalaev, A. Boltasseva, B. Gholipour, H. Krishnamoorthy, K. MacDolnald, C. Soci, N. I. Zheludev, V. Savinov, R. Singh, P. Groß, C. Lienau, M. Vadai, M. L. Solomon, D. R. Barton III, M. Lawrence, J. A. Dionne, S. V Boriskina, R. Esteban, J. Aizpurua, X. Zhang, S. Yang, D. Wang, W. Wang, T. W. Odom, N. Accanto, P. M. de Roque, I. M. Hancu, L. Piatkoqski, N. F. van Hulst, and M. F. Kling, "Roadmap on plasmonics," J. Opt. **20**, 043001 (2018).

57. G. V. Naik, V. M. Shalaev, and A. Boltasseva, "Alternative Plasmonic Materials: Beyond Gold and Silver," Adv. Mater. **25**, 3264–3294 (2013).

58. U. Guler, A. Boltasseva, and V. M. Shalaev, "Refractory plasmonics," Science (80-.). **344**, 263–264 (2014).

59. J. Hu, X. Ren, A. N. Reed, T. Reese, D. Rhee, B. Howe, L. J. Lauhon, A. M. Urbas, and T. W. Odom, "Evolutionary Design and Prototyping of Single Crystalline Titanium Nitride Lattice Optics," ACS Photonics **4**, 606–612 (2017).

60. J. A. Briggs, G. V. Naik, T. A. Petach, B. K. Baum, D. Goldhaber-Gordon, and J. A. Dionne, "Fully CMOS-compatible titanium nitride nanoantennas," Appl. Phys. Lett. **108**, 051110 (2016).

61. L. M. Otto, A. T. Hammack, S. Aloni, D. F. Ogletree, D. L. Olynick, S. Dhuey, B. J. H. Stadler, and A. M. Schwartzberg, "Plasma-enhanced atomic layer deposition for plasmonic TiN," in S. Cabrini, G. Lérondel, A. M. Schwartzberg, and T. Mokari, eds. (2016), p. 99190N.

62. P. R. West, S. Ishii, G. V. Naik, N. K. Emani, V. M. Shalaev, and A. Boltasseva, "Searching for better plasmonic materials," Laser Photon. Rev. **4**, 795–808 (2010).

63. P. Patsalas, N. Kalfagiannis, and S. Kassavetis, "Optical properties and plasmonic performance of titanium nitride," Materials (Basel). **8**, 3128–3154 (2015).

64. D. Shah, H. Reddy, N. Kinsey, V. M. Shalaev, and A. Boltasseva, "Optical Properties of Plasmonic Ultrathin TiN Films," Adv. Opt. Mater. **5**, 1–5 (2017).

65. A. Catellani and A. Calzolari, "Plasmonic properties of refractory titanium nitride," Phys. Rev. (2017).

66. P. Huber, D. Manova, S. Mändl, and B. Rauschenbach, "Optical characterization of TiN produced by metal-plasma immersion ion implantation," Surf. Coatings Technol. **142**–**144**, 418–423 (2001).

67. R. P. Sugavaneshwar, S. Ishii, T. D. Dao, A. Ohi, T. Nabatame, and T. Nagao, "Fabrication of Highly Metallic TiN Films by Pulsed Laser Deposition Method for Plasmonic Applications," ACS Photonics **5**, 814–819 (2018).

68. S. M. Edlou, J. C. Simons, G. A. Al-Jumaily, and N. A. Raouf, "Optical and electrical properties of reactively sputtered TiN, ZrN, and HfN thin films," in *SPIE 2262, Optical Thin Films IV: New Developments* (1994), Vol. 2262, pp. 96–106.

69. E. Langereis, S. B. S. Heil, H. C. M. Knoops, W. Keuning, M. C. M. van de Sanden, and W. M. M. Kessels, "*In situ* spectroscopic ellipsometry as a versatile tool for studying atomic layer

deposition," J. Phys. D. Appl. Phys. **42**, 073001 (2009).

70. S. Logothetidis, I. Alexandrou, and A. Papadopoulos, "*In situ* spectroscopic ellipsometry to monitor the process of TiN $_x$ thin films deposited by reactive sputtering," J. Appl. Phys. **77**, 1043–1047 (1995).

71. H. G. Tompkins and J. N. Hilfiker, *Spectroscopic Ellipsometry : Practical Application to Thin Film Characterization* (n.d.).

72. J. N. . Hilfiker and T. Tiwald, "Dielectric Function Modelling," H. Fujiwara R. Collins (Eds.), Spectrosc. Ellipsom. Photovoltaics, Springer (2018).

73. B. Johs and J. S. Hale, "Dielectric function representation by B-splines," Phys. status solidi **205**, 715–719 (2008).

74. J. N. Hilfiker, N. Singh, T. Tiwald, D. Convey, S. M. Smith, J. H. Baker, and H. G. Tompkins, "Survey of methods to characterize thin absorbing films with Spectroscopic Ellipsometry," Thin Solid Films **516**, 7979–7989 (2008).

75. J. N. Hilfiker, R. A. Synowicki, and H. G. Tompkins, "Spectroscopic ellipsometry methods for thin absorbing coatings," in *51st Annual Technical Conference Proceedings of the Society of Vacuum Coaters* (2008), pp. 511–516.

76. R. A. Synowicki, "Suppression of backside reflections from transparent substrates," Phys. status solidi **5**, 1085–1088 (2008).

77. R. L. Sutherland, D. G. McLean, and S. Kirkpatrick, *Handbook of Nonlinear Optics.* (Marcel Dekker, 2003).

78. D. N. Nikogosi͡an, *Nonlinear Optical Crystals : A Complete Survey* (Springer-Science, 2005).

79. S. Basu, "A review of nonlinear optical organic materials," Ind. Eng. Chem. Prod. Res. Dev.

23, 183–186 (1984).

80. D. S. Chemla and J. Zyss, *Nonlinear Optical Properties of Organic Molecules and Crystals* (Academic Press, 1987).

81. J. Cimek, N. Liaros, S. Couris, R. Stępień, M. Klimczak, R. Buczyński, A. D. Sontakke, K. Biswas, A. Tarafder, R. Sen, K. Annapurna, and B. Er, "Experimental investigation of the nonlinear refractive index of various soft glasses dedicated for development of nonlinear photonic crystal fibers References and links," (2017).

82. A. V. Krasavin, P. Ginzburg, and A. V. Zayats, "Free-electron Optical Nonlinearities in Plasmonic Nanostructures: A Review of the Hydrodynamic Description," Laser Photon. Rev. **12**, 1700082 (2018).

83. N. C. Panoiu, W. E. I. Sha, D. Y. Lei, and G.-C. Li, "Nonlinear optics in plasmonic nanostructures," J. Opt. **20**, 083001 (2018).

84. P. Guo, R. D. Schaller, L. E. Ocola, B. T. Diroll, J. B. Ketterson, and R. P. H. Chang, "Large optical nonlinearity of ITO nanorods for sub-picosecond all-optical modulation of the full-visible spectrum," Nat. Commun. **7**, 12892 (2016).

85. L. Wang, S. Kruk, K. Koshelev, I. Kravchenko, B. Luther-Davies, and Y. Kivshar, "Nonlinear Wavefront Control with All-Dielectric Metasurfaces," Nano Lett. **18**, 3978–3984 (2018).

86. A. Krasnok, M. Tymchenko, and A. Alù, "Nonlinear metasurfaces: a paradigm shift in nonlinear optics," Mater. Today **21**, 8–21 (2018).

87. H. Husu, R. Siikanen, J. Mäkitalo, J. Lehtolahti, J. Laukkanen, M. Kuittinen, and M. Kauranen, "Metamaterials with Tailored Nonlinear Optical Response," Nano Lett. **12**, 673–677 (2012).

88. M. Z. Alam, S. A. Schulz, J. Upham, I. De Leon, and R. W. Boyd, "Large optical nonlinearity of nanoantennas coupled to an epsilon-near-zero material," Nat. Photonics **12**, 79–83 (2018).

89. M. Pietrzyk, R. Kaipurath, D. Faccio, and A. Di Falco, "Epsilon near zero metamaterials for ultra-low power nonlinear applications," **9371**, 93710Y (2015).

90. R. M. Kaipurath, M. Pietrzyk, L. Caspani, T. Roger, M. Clerici, C. Rizza, A. Ciattoni, A. Di Falco, and D. Faccio, "Optically induced metal-to-dielectric transition in Epsilon-Near-Zero metamaterials," Sci. Rep. **6**, 27700 (2016).

91. X. Li, M. Pietrzyk, D. Faccio, C. Rizza, A. Ciattoni, and A. Di Falco, "Linear and nonlinear optical behavior of epsilon near zero metamaterials: opportunities and challenges," Proc. SPIE **10111**, 101111O (2017).

92. R. W. Ziolkowski, "Propagation in and scattering from a matched metamaterial having a zero index of refraction," Phys. Rev. E **70**, 046608 (2004).

93. A. Capretti, Y. Wang, N. Engheta, and L. Dal Negro, "Enhanced third-harmonic generation in Si-compatible epsilon-near-zero indium tin oxide nanolayers," Opt. Lett. **40**, 1500–3 (2015).

94. T. S. Luk, D. De Ceglia, S. Liu, G. A. Keeler, R. P. Prasankumar, M. A. Vincenti, M. Scalora, M. B. Sinclair, and S. Campione, "Enhanced third harmonic generation from the epsilon-near-zero modes of ultrathin films," Appl. Phys. Lett. **106**, (2015).

95. D. De Ceglia, S. Campione, M. A. Vincenti, F. Capolino, and M. Scalora, "Low-damping epsilon-near-zero slabs: Nonlinear and nonlocal optical properties," Phys. Rev. B - Condens. Matter Mater. Phys. **87**, 1–35 (2013).

96. C. Argyropoulos, P. Y. Chen, G. D'Aguanno, N. Engheta, and A. Alù, "Boosting optical nonlinearities in epsilon-near-zero plasmonic channels," Phys. Rev. B - Condens. Matter Mater. Phys. **85**, (2012).

97. N. Kinsey, A. A. Syed, D. Courtwright, C. DeVault, C. E. Bonner, V. I. Gavrilenko, V. M. Shalaev, D. J. Hagan, E. W. Van Stryland, and A. Boltasseva, "Effective third-order nonlinearities in metallic refractory titanium nitride thin films," Opt. Mater. Express **5**, 2395 (2015).

98. R. Secondo, J. Khurgin, and N. Kinsey, "Absorptive loss and band non-parabolicity as a physical origin of large nonlinearity in epsilon-near-zero materials," Opt. Mater. Express **10**, 1545 (2020).

99. S. Vezzoli, V. Bruno, C. DeVault, T. Roger, V. M. Shalaev, A. Boltasseva, M. Ferrera, M. Clerici, A. Dubietis, and D. Faccio, "Optical time reversal from time-dependent Epsilon-Near-Zero media," 1–5 (2017).

100. M. A. Vincenti, D. De Ceglia, A. Ciattoni, and M. Scalora, "Singularity-driven second- and third-harmonic generation at ε-near-zero crossing points," Phys. Rev. A - At. Mol. Opt. Phys. **84**, 1–6 (2011).

101. E. Carnemolla, L. Caspani, C. DeVault, M. Clerici, S. Vezzoli, V. Bruno, V. Shalaev, D. Faccio, A. Boltasseva, and M. Ferrera, "Degenerate optical nonlinear enhancement in epsilon-near-zero transparent conducting oxides," Opt. Mater. Express **8**, 3392–3400 (2018).

102. N. Kinsey, C. DeVault, J. Kim, M. Ferrera, V. M. Shalaev, and A. Boltasseva, "Epsilon-near-zero Al-doped ZnO for ultrafast switching at telecom wavelengths," Optica **2**, 616 (2015).

103. S. Benis, P. Zhao, D. J. Hagan, and E. W. Van Stryland, "Nondegenerate, Transient Nonlinear

Refraction of Indium Tin Oxide Excited at Epsilon-Near-Zero," in *Nonlinear Optics* (OSA, 2017), p. NW1A.3.

104. E. W. Van Stryland and M. Sheik-Bahae, "Z-scan technique for nonlinear materials characterization," 102910Q (1997).

105. M. Conforti and G. Della Valle, "Derivation of third-order nonlinear susceptibility of thin metal films as a delayed optical response," Phys. Rev. B **85**, 245423 (2012).

106. E. G. Carnemolla, L. Caspani, C. DeVault, M. Clerici, S. Vezzoli, V. Bruno, V. M. Shalaev, D. Faccio, A. Boltasseva, and M. Ferrera, "Degenerate optical nonlinear enhancement in epsilon-near-zero transparent conducting oxides," Opt. Mater. Express **8**, 3392 (2018).

107. A. S. Gadallah and M. M. El-Nahass, "Structural, optical constants and photoluminescence of ZnO thin films grown by sol-gel spin coating," Adv. Condens. Matter Phys. **2013**, (2013).

108. S. Wu, P. Geiser, J. Jun, J. Karpinski, D. Wang, and R. Sobolewski, "Time-resolved intervalley transitions in GaN single crystals," J. Appl. Phys. **101**, 043701 (2007).

109. N. Kinsey, C. DeVault, J. Kim, M. Ferrera, V. M. Shalaev, and A. Boltasseva, "Epsilon-near-zero Al-doped ZnO for ultrafast switching at telecom wavelengths," Optica **2**, 616–622 (2015).

110. M. Clerici, N. Kinsey, C. DeVault, J. Kim, E. G. Carnemolla, L. Caspani, A. Shaltout, D. Faccio, V. Shalaev, A. Boltasseva, and M. Ferrera, "Controlling hybrid nonlinearities in transparent conducting oxides via two-colour excitation," Nat. Commun. **8**, 15829 (2017).

111. J. Khurgin, M. Clerici, V. Bruno, L. Caspani, C. DeVault, J. Kim, A. Shaltout, A. Boltasseva, V. Shalaev, M. Ferrera, D. Faccio, and N. Kinsey, "Adiabatic frequency conversion in epsilon near zero materials: the role of group velocity," Optica **7**, 226–231 (2020).

112. C. B. De Araújo, A. S. L. Gomes, and G. Boudebs, "Techniques for nonlinear optical characterization of materials: A review," Reports Prog. Phys. **79**, (2016).

113. M. Ferdinandus, "Techniques For Characterization Of Third Order Optical Nonlinearities," Electron. Theses Diss. 2004-2019 (2014).

114. D. J. Hagan, D. Peceli, D. A. Fishman, E. W. Van Stryland, H. Hu, J. M. Reed, M. R. Ferdinandus, M. Seidel, M. Reichert, P. Zhao, S. Webster, and T. R. Ensley, "Temporal, spectral, and polarization dependence of the nonlinear optical response of carbon disulfide," Opt. Vol. 1, Issue 6, pp. 436-445 **1**, 436–445 (2014).

115. D. J. Hagan, E. W. Van Stryland, H. Hu, M. R. Ferdinandus, and M. Reichert, "Beam deflection measurement of time and polarization resolved ultrafast nonlinear refraction," Opt. Lett. Vol. 38, Issue 18, pp. 3518-3521 **38**, 3518–3521 (2013).

116. A. Urbas, F. K. Hopkins, J. M. Reed, K. L. Averett, and M. R. Ferdinandus, "Analysis of beam deflection measurements in the presence of linear absorption," Opt. Mater. Express, Vol. 7, Issue 5, pp. 1598-1605 **7**, 1598–1605 (2017).

117. N. Yu, P. Genevet, M. A. Kats, F. Aieta, J.-P. Tetienne, F. Capasso, and Z. Gaburro, "Light Propagation with Phase Discontinuities: Generalized Laws of Reflection and Refraction," Science (80-.). **334**, 333–337 (2011).

118. E. Hecht, "Optics (4th Edition)," 680 (2001).

119. M. Born, E. Wolf, A. B. Bhatia, P. C. Clemmow, D. Gabor, A. R. Stokes, A. M. Taylor, P. A. Wayman, and W. L. Wilcock, "Principles of Optics: Electromagnetic Theory of Propagation, Interference and Diffraction of Light," Princ. Opt. (1999).

120. P. Yeh, "Optical Waves in Layered Media (Pure & Applied Optics)," (1988).

121. V. Bruno, S. Vezzoli, C. DeVault, T. Roger, M. Ferrera, A. Boltasseva, V. M. Shalaev, and D. Faccio, "Dynamical Control of Broadband Coherent Absorption in ENZ Films," Micromachines **11**, (2020).

9. PUBLICATIONS

9.1. Journal

KN Al-Milaji, RR Secondo, TN Ng, N Kinsey, H Zhao “Interfacial Self-Assembly of Colloidal Nanoparticles in Dual-Droplet Inkjet Printing” *Advanced Materials Interfaces* **5** (10), 1701561 (2018)

R Secondo, D Fomra, N Izyumskaya, V Avrutin, JN Hilfiker, A Martin, N Kinsey “Reliable modeling of ultrathin alternative plasmonic materials using spectroscopic ellipsometry” *Optical Materials Express* **9** (2), (2019)

- Editor’s Choice

R Secondo, J Khurgin, N Kinsey “Absorptive loss and band non-parabolicity as a physical origin of large nonlinearity in epsilon-near-zero materials” *Optical Materials Express* **10** (7) (2020)

D Fomra, R Secondo, K Ding, V Avrutin, N Izyumskaya, Ü Özgür, N Kinsey “Plasmonic titanium nitride via atomic layer deposition: A low-temperature route” *Journal of Applied Physics* **127** (10), (2020)

9.2. Conference

R Secondo, V Avrutin, Ü Özgür, N Kinsey “Optimization of Titanium Nitride Films using Plasma Enhanced Atomic Layer Deposition” *CLEO: Science and Innovations*, JTh2A. 75 (2018)

D Fomra, R Secondo, V Avrutin, N Izyumskaya, K Ding, Ü Özgür, N Kinsey “Optimized Growth of Titanium Nitride Films Using Plasma-Enhanced Atomic Layer Deposition” *Laser Science, JTu2A.* (2018)

R Secondo, N Kinsey “Modelling Nonlinear Near-Zero-Index Media through Carrier Kinetic Models” *Frontiers in Optics,* JTu4A. 34 (2019)

R Secondo, N Kinsey “Carrier kinetic models for intensity dependent refractive index in near-zero-index media (Conference Presentation)” *Active Photonic Platforms* XI 11081, 110810L (2019)

Best Student Presentation Award

N Kinsey, R Secondo, D Fomra “Optical Nonlinearities in Transparent Conducting Oxides—The Role of Loss” 2019 IEEE Research and Applications of Photonics in Defense Conference (2019)

R Secondo, D Fomra, N Izyumskaya, V Avrutin, Ü Özgür, N Kinsey “Characterization of plasma enhanced atomic layer deposited titanium nitride” *Nanophotonic Materials XV* (2018)

R Secondo, KN Al-Milaji, TN Ng, H Zhao, N Kinsey “Numerical Characterization of Monolayer Ink-Jet Printed Polystyrene Lattice” CLEO: Applications and Technology, JTh2A. 80 (2018)